The Thesis Committee for Christina Danielle James

certifies that this is the approved version of the following thesis:

A central Texas drying event identified at the Younger Dryas-early Holocene transition using coupled speleothem $\delta^{13}C$-^{14}C analysis

Approved By

Supervising Committee:

Supervisor: _____
Jay Banner

_____
Dan Breecker

_____
Nathan Miller

A central Texas drying event identified at the Younger Dryas-early Holocene transition using coupled speleothem $\delta^{13}C$-^{14}C analysis

by

Christina Danielle James

Thesis

Presented to the Faculty of the Graduate School of

The University of Texas at Austin

In Partial Fulfillment of The Requirements for the Degree of

Master of Science in Geological Sciences

The University of Texas at Austin

December 2017

Acknowledgements

Completing a thought-provoking and challenging, yet strenuous journey is never a task meant for the sole contribution of one individual. These types of feats can only be achieved with the help, guidance and forethought of highly-skilled, motivated and supportive companions. There are several people who have guided me along in completing this research and I am deeply thankful for their help. I would like to thank my advisor Jay Banner for his esteemed insight, guidance and encouragement through this entire process. This research would not have been possible without Sylvia Pope's (Department of Watershed Protection) efforts in collecting the sample. I would also like to thank Dan Breecker, whose valuable knowledge has helped propel this research to a higher and more inventive platform. Nate Miller has always been supportive, and I am very grateful for his open availability and willingness to take time answering all of my many questions. Toti Larson has given me valued lab experience and assistance, but also provided benevolence and laughter. Eric James' plethora of knowledge and knowhow has been greatly valued; however, his warm spirit and unwavering positivity are what inspired me the most. I would also like to thank both Staci Loewy and Alison Koleszar for their immense and crucial help in the lab. Alexandra Noronha's knowledge and approach to tackling scientific inquiry has been vital to my research; however, it was her thoughtfulness, compassion and fervent support which gave me the mental resolute to stay on track. Kara Posso's astute disposition, compassion, and laughter have been an important piece for my motivation; and Peter Carlson has provided me ample guidance and great scientific discussions. Lastly, I would like to thank my family who have always provided me with countless opportunities, my grandfather who saw more for me than I did myself, and my husband who has given me limitless and unyielding support.

Abstract

A central Texas drying event identified at the Younger Dryas-early Holocene transition using coupled speleothem $\delta^{13}C$-^{14}C analysis

Christina D. James, M.S. Geo. Sci.

The University of Texas at Austin, 2017

Supervisor: Jay Banner

The Younger Dryas (YD, 12,900-11,700 years BP) is characterized by a return to near-glacial conditions in the northern hemisphere during the last deglacial period. Texas moisture proxy records support a general regional warming/drying trend from the YD through the Holocene, however, the timing and magnitude of changes in regional moisture and temperature conditions are poorly constrained. We use moisture proxies from a central Texas stalagmite record (McN-1) collected in the Edwards aquifer (an important human and ecological groundwater resource in central Texas) to assess how epikarst moisture conditions varied in the region during the YD-Holocene transition. The relatively high concentrations of ^{232}Th (>1 ppb) in several horizons in this sample resulted in McN-1 U-series ages with high uncertainties (>10% of measured age). We use two isochrons and measured $^{230}Th/^{232}Th$ ratios from modern calcite grown in central Texas caves to estimate the McN-1 initial $^{230}Th/^{232}Th$ ratio and develop an age model with better constrained uncertainties. Strong correlations between speleothem $\delta^{13}C$ and ^{14}C activities can

result from changes in epikarst carbonate dissolution due to variable CO_2 ventilation or pore space moisture. A decrease in the proportion of ^{14}C-free carbon (the dead carbon proportion, DCP) to 0% is interpreted as a change from partial dissolution in a water-saturated closed system to dissolution in an open system, where carbon from limestone has no measurable effect on dissolved inorganic carbon ^{14}C activities. A negative shift in $\delta^{13}C$ values of 2.8‰ coincident with a decrease in DCP from 7.5 to 0% occurs in McN-1 at the Younger Dryas-Holocene boundary in less than 230 years (as little as 50 years given age constraints). We attribute these parallel declines in $\delta^{13}C$ and DCP to changes in the epikarst dissolution system. If changes in the dissolution system are controlled by pore space moisture, the change to an open system at the YD-Holocene boundary indicates a rapid regional drying event. Application of a calcite dissolution model indicates that 25% of the negative $\delta^{13}C$ shift can be explained by change from a more closed to an open system in the epikarst dissolution region above the cave. We attribute the remaining shift in $\delta^{13}C$ values to reduced drip water pH, associated with an increased contribution of respired CO_2 to epikarst pCO_2. Speleothem growth rates decrease at the YD-Holocene boundary, consistent with our interpretation that carbon isotopes record a decrease in vadose zone moisture. This epikarst moisture interpretation is consistent with other Texas paleoclimate records, indicating a climate transition to drier early Holocene conditions. Compared with existing regional proxy records, the relatively high temporal resolution of the McN-1 $\delta^{13}C$ record (inter-annual) indicates a rapid drying event concurrent with Greenland temperature increases, suggesting a contemporaneous climate response between regional and high latitude climate at end of the YD.

Table of Contents

CHAPTER 1: INTRODUCTION

Texas is a semi-arid region that is projected to experience a decrease in precipitation, runoff and soil moisture over the 21st century as a result of anthropogenic climate change (Banner et al., 2010; Seager at al., 2013). The state's population is expected to double over the next century and will result in state water demands that are expected to increase by 20%, with some central Texas counties projecting water demand increases of up to 400% (Banner et al., 2010; TWDB, 2017). Therefore, state water resource planning will need to take into account climate models that capture the hydrologic variability of the region. Reconstructing paleoclimate is important for understanding climate variability and can be used in conjunction with climate models to better predict future changes in hydroclimate (Masson-Delmotte et al., 2013). Speleothem $\delta^{13}C$ records have been used to reconstruct past climate, including changes in moisture amount (Dorale et al., 1992; Bar-Matthews et al., 1997; Genty et al., 2001, 2006; Oster et al., 2010; Griffiths et al., 2012). Interpretation of these records has proven to be difficult, however, because multiple processes can control speleothem $\delta^{13}C$ values. In particular, both speleothem $\delta^{13}C$ and ^{14}C have been shown to reflect carbon contributions from the atmosphere, soil, organic carbon in the subsoil vadose zone, and carbonate bedrock (Genty et al., 2001; Oster et al., 2010; Atkinson, 1977; Mattey et al., 2016; McDonough et al., 2016; Noronha et al., 2015; Wood et al., 1993; Wood and Petraitis, 1984; Bergel et al., in press). Because of these complexities, paleoenvironmental interpretations of speleothem $\delta^{13}C$ records are commonly under-utilized; however, recent studies show strong correlations between speleothem calcite $\delta^{13}C$ and secular changes in

moisture amount above the cave (Frappier et al., 2002; Oster et al., 2010; Meyer et al., 2014; Ridely et al., 2015).

We use coupled $\delta^{13}C$-^{14}C analysis to assess the relationship between moisture conditions and carbon isotopes during the late Pleistocene [Younger Dryas (YD)]-Holocene transition, from McN-1, a stalagmite collected in Austin. McN-1 is from a cave formed in carbonate bedrock of the Edwards aquifer (an important regional water resource). To provide regional context, we also compare McN-1 to a central Texas speleothem (CWN-4) that spans a similar time period [19,000 – 9,500 calendar years BP (referred to as 'yrs BP' hereafter)] from a cave located approximately 100 km southwest. McN-1 $\delta^{13}C$ values show an abrupt decrease of 3‰ at the beginning of the Holocene with a concurrent decrease in dead carbon proportion (DCP) of 7.5% (Fig. 7). This parallel behavior suggests that changes in vadose zone hydrology and the associated carbonate dissolution regime control speleothem carbon isotopes in this locality. Here, we model changes in the carbonate dissolution regime from our DCP and $\delta^{13}C$ results to understand changes in moisture above the cave, and show that an abrupt drying event immediately followed the YD.

1.1 Younger Dryas climate event

The last deglacial period (18,000 – 11,700 yrs BP) is recognized as a period of abrupt changes in global climate, with several post-glacial warming and cooling events (Clark et al., 2012). The Younger Dryas (12,900-11,700 yrs BP) was a northern hemisphere cooling event characterized by a return to near-glacial conditions, as originally documented in

pollen, lake and ice-core temperature proxy records (Dansgaard et al., 1989; Taylor et al., 1993; Stuiver et al., 1995; Grootes et al, 1997). Based on the Greenland Ice Sheet Project 2 (GISP2) record (Fig. 7), Severinghaus et al. (1998) suggested that Greenland temperatures decreased by 5-10° C during the beginning of the YD; however, these temperature changes would be magnified in the polar regions, with temperature decreases closer to 4-6° C near the low-mid latitudes (Cuffey et al., 1995). Based on the Northern Greenland Ice Core Project and GISP2 ice-core records, the termination of the YD was a large and rapid warming event, with temperature increases of 7-9° C occurring within decades (Svensson et al., 2008; Taylor et al., 1993; Alley, 2000; Rasmussen et al., 2006). The hemispheric-wide warming experienced at the termination of the YD was the largest rapid warming event from the past 13,000 years prior to modern anthropogenic greenhouse warming. The abrupt nature, forcing mechanisms, and regional/global climate responses across the YD-Holocene transition are therefore extensively studied because of the broad implications for understanding climate variability in association with anthropogenic-induced warming. Global responses during the YD include widespread high-latitude cooling in the northern hemisphere, Antarctic warming and reduced African and Asian monsoon intensity (Stocker et al., 1992; Alley and Clark, 1999; Talbot et al., 2007). In Texas, multiple moisture proxy records suggest a regional drying trend following the YD and extending through the early Holocene (Toomey et al., 1993; Holliday, 2000; Polyak et al., 2004; Ellwood and Gose, 2007; Wong et al., 2015). These records have rather poor constraints on the magnitude and timing of moisture changes, and thus there remains a need for improved Texas paleoclimate records (such as McN-1) to better to constrain the timing and nature of hydroclimate change over the YD-early Holocene transition. Texas' modern

hydroclimate is complex with multiple air mass regimes that transport moisture to the region (Seager et al., 2007; Berkelhammer et al., 2011). Hemispheric-wide climate changes (such as the YD) can shift the position of air mass regimes (Allen and Anderson, 1993; McGabe, 1996) and alter the distribution of regional rainfall. Moisture changes in Texas during the YD-Holocene transition could result from shifts in hemispheric-wide teleconnections, and represent regional climate responses to global-scaled warming events. This study focuses on moisture changes during the transition from the YD to the early Holocene, and could provide important context for connections between regional changes in moisture and northern hemisphere teleconnections.

1.2 Background

Controls on speleothem $\delta^{13}C$ involve carbon reservoirs and processes within and between the cave, epikarst and atmosphere. These include changes in the concentration and $\delta^{13}C$ composition of atmospheric CO_2, changes in water availability that influence C_3 plant $\delta^{13}C$ values, and rates of soil CO_2 production (e.g. Kohn, 2010; Diefendorf et al., 2010). Other controls include: changes in vegetation type (C_3 vs. C_4 plants), the magnitude of CO_2 degassing from drip water, drip rates, the age of organic matter, and the proportion of host rock carbon (Hendy, 1971; Bar-Matthews et al., 1999; Mickler et al., 2004; Mickler et al., 2006; Fairchild et al., 2006; Dreybrodt and Scholz, 2011; Deininger et al. 2012; Meyer et al., 2014; Breecker et al., 2017). Several processes that can influence $\delta^{13}C$ in speleothems occur in soil and epikarst above the cave before speleothem calcite precipitation begins (Fig. 2). Meteoric water infiltrates the epikarst and interacts with epikarst CO_2, decreasing its pH and increasing dissolved inorganic carbon (DIC) concentrations [e.g. $CO_{2(aq)}$,

bicarbonate (HCO_3^-), and carbonate (CO_3^{2-})]. The acidic DIC solution dissolves karst carbonate minerals (Equation 1) until equilibrium with respect to calcite is established. The pH of water within the limestone is typically 7.5-8.5, where the dominant DIC species is HCO_3^- (Meyer et al., 2014). When encountering the lower pCO_2 conditions of the cave, CO_2 degasses from the solution (drip water) and calcite precipitates via Equation 2:

$$H_2CO_3 + CaCO_3 \rightarrow Ca^{2+} + 2HCO_3^- \quad \text{Equation 1}$$

$$Ca^{2+} + 2HCO_3^- \rightarrow CO_2 + H_2O + CaCO_3 \quad \text{Equation 2}$$

Identifying the nature of carbonate dissolution along the soil-bedrock profile is important for understanding variability in DIC $\delta^{13}C$. Speleothem carbon can be derived from a combination of soil-respired CO_2 [either from root respiration or soil organic matter (SOM) decomposition], deep organic matter (OM) and carbonate bedrock (Meyer et al., 2014). Noronha et al. (2015) suggest that most speleothem carbon derives from CO_2 produced by microbial decomposition of relatively old OM (40-600 years) deeper in the soil/bedrock profile. The $\delta^{13}C$ values of CO_2 produced from OM are typically within 1‰ of the OM $\delta^{13}C$ values (Bowling et al., 2008). This contrasts from previous observations that root-respired CO_2 is the primary source for speleothem carbon (Genty et al., 2001). Biologically respired CO_2 by either scenario is has lower $\delta^{13}C$ values (~ -30 to -20‰) than carbonate bedrock, which typically has values near 0‰ (Dorale et al., 1993; Genty et al., 2001).

Climate driven changes in C_3 vs C_4 vegetation above the cave can control the $\delta^{13}C$ of soil CO_2 (Hendy, 1971; Baker et. al, 1997; McDermott, 2004). However, Breecker, et al. (2012) and Meyer et al. (2014) show that deeply rooted plants (e.g. trees) are the primary

source of respired carbon to central Texas caves. In most ecosystems, C_3 plants have deeper roots than C_4 plants, suggesting a strong C_3 bias on speleothem $\delta^{13}C$, and suggesting minimal $\delta^{13}C$ contribution from changes in C_3 vs C_4 vegetation. Furthermore, carbon turnover times for deep OM are slow, typically occurring over centennial-millennial timescales (Trumbore et al., 1996; Noronha et al., 2015). Therefore, changes in the relative abundance of C_3 vs. C_4 vegetation should be preserved in the speleothem $\delta^{13}C$ record over centennial-millennial timescales, but cannot reasonably account for abrupt (e.g. multi-decadal) changes speleothem $\delta^{13}C$.

The temperature-dependent equilibrium $\delta^{13}C$ fractionation factors between DIC species, CO_2 gas, and calcite also control speleothem $\delta^{13}C$, with typical $CaCO_3$-HCO_3^- fractionation factors of 0-2‰ for temperatures ranging between 10-30 ^oC (Deines et al., 2974; Mook, 2002). Kinetic fractionation of drip water, as it enters the cave or during calcite precipitation, can be a strong control on speleothem $\delta^{13}C$. The lower pCO_2 conditions of a cave (relative to the epikarst) cause rapid degassing of CO_2 in drip water, resulting in preferential $^{12}CO_2$ loss to the gas phase. Changes in cave ventilation, often resulting from seasonal temperature changes, affect the amount of cave air pCO_2 and therefore, control the rate of drip water CO_2 degassing (Banner et al., 2007; Meyer et al., 2014). Cave-air that is warmer than outside air (winter conditions) causes density-driven ventilation and mixing with outside air (lower pCO_2), resulting in lower cave air pCO_2 and enhanced degassing (Banner et al., 2007; Cowan et al., 2013). Slower drip rates increase speleothem $\delta^{13}C$ due to longer intervals between each drip, resulting in more CO_2 degassing, which preferentially removes ^{12}C (Mickler et al., 2004; Dreybrodt and Scholz,

2011; Meyer et al., 2014). Prior calcite precipitation (PCP) is the process of degassing and precipitation of calcite within epikarst void space, before drip water enters the cave. Factors promoting PCP include drier epikarst conditions or lower cave air CO_2 (Bourges et al., 2001; Fairchild et al., 2006). Increased PCP causes $^{12}CO_2$ to preferentially escape from oversaturated waters and results in increased $\delta^{13}C$ values of drip water (Meyer et al., 2014). However, fractionation of ^{14}C as a result of PCP is minimal, and therefore PCP has a negligible effect on speleothem ^{14}C activities.

Carbon sources (organic carbon and usually a component from carbonate bedrock) that contribute to drip water DIC ultimately control ^{14}C activity. The ^{14}C activity of speleothem carbon sourced from OM CO_2 is less radiogenic than the contemporaneous atmosphere, with typical values of ~90 percent modern carbon (pMC; Noronha et al., 2015). The ^{14}C activity of speleothem carbon derived primarily from carbonate bedrock (typically older than 40,000 years) is 0 pMC (Fig. 2). To quantify the amount of speleothem carbon derived from OM or carbonate bedrock, we calculate the "dead carbon proportion" (DCP), which is the difference between atmospheric and speleothem ^{14}C at a given time in the past. Previous studies (Genty et al., 2001; Fohlmeister et al., 2011; Griffiths et al., 2012; and Noronha et al., 2014) suggest that epikarst carbonate dissolution processes are a strong control on DCP. Under open system conditions (large gas/water volume ratio) in the carbonate dissolution regime, most of the carbon is in the gas phase as CO_2, and little carbonate rock dissolution is required to reach equilibrium; thus, the $\delta^{13}C$ values and ^{14}C activities of DIC are controlled by respired CO_2. In open systems, ^{14}C activities of the DIC approach values similar to OM, while DIC $\delta^{13}C$ values are ~8‰ higher than OM due to

equilibrium fractionation, corresponding to relatively lower DCP (~0%) and $\delta^{13}C$ values (Figure 14). However, under closed system conditions with small gas/water volume ratios, the fraction of carbon from the rock required to attain equilibrium is larger, and therefore, DCP values theoretically approach 50% (based on the stoichiometric relationship between CO_2 and $CaCO_3$ in the carbonate dissolution equation). The $\delta^{13}C$ values of DIC also represent a 50/50 mixture of respired CO_2 and carbonate rock carbon (Hendy, 1971). Carbonate dissolution in natural systems varies between these two end-member scenarios, with most systems being closer to the open system endmember.

1.3 Hydrogeologic Setting

McN-1 stalagmite was collected from a 7m long, 1.5m high, shallow cave (~2m below ground surface; Fig. S3) located near McNeil High School in north Austin, Texas (Fig. 1; 30º44'69.28" N, -97º73'29.35", 269 m above sea level). The cave is one of several caves in the region that were discovered during construction of utilities, roads and housing developments. The cave was filled with concrete on August 12, 2014, preventing any access. The cave developed in the Kainer Formation of the Edwards Group. The Edwards Group is Cretaceous in age, approximately 200 m thick, highly permeable and fractured, and exposed at ground surface across the Balcones fault zone (Fisher and Rodda, 1969; Saribudak, 2016). Soils developed on Edwards Group units are typically thin (< 30 cm) and clay-rich, supporting juniper savanna, oak, elm and woodlands (Cooke et al., 2007). The cave is currently covered by a mixture of grassland, oak, elm and juniper. The Edwards Group is one of the two water-bearing units (along with the Trinity Group) of the Edwards

aquifer (Fig. 1). The Edwards aquifer is highly transmissive and is an important human and ecological groundwater resource in central Texas, supplying drinking water to 1.5 million people (Sharp and Banner, 2000; Eberts et al., 2011; Gary et al., 2011). Recharge of the Edwards aquifer primarily comes from surface stream losses over the highly permeable carbonate bedrock, while discharge is primarily from spring flow and well withdrawal (Eberts et al., 2011).

Central Texas rainfall is mainly sourced from the Gulf of Mexico via the Great Plains low-level jet (Seager et al., 2007). Increased moisture contributions from Pacific westerly storm tracks occur during the winter (Berkelhammer et al., 2011). The North American Monsoon episodically brings rainfall variously sourced from the Gulf of California, Gulf of Mexico, and tropical Pacific (Higgins, 1997). Speleothem δ^{18}O values from several caves across the southwestern U.S. spanning the same time interval as McN-1 show influences of past moisture delivery via low-δ^{18}O Pacific moisture to the west and high δ^{18}O GoM moisture (Asmerom et al., 2010; Wagner et al., 2010; Feng et al., 2014). Rainfall in the region is bimodal, with most accumulation in the spring and fall, bracketing relatively dry summers. Average annual rainfall in central Texas is ~83 cm/year, with several state-wide droughts occurring over the past century (Stahle and Cleaveland, 1988; NOAA, 2017).

CHAPTER 2: METHODOLOGY

2.1 Sample Selection and Preparation of Stalagmite McN-1

McN-1 was cut along its central growth axis using a water saw, and slab faces polished using diamond lapidary wheels. McN-1 is 58 cm long and 10 cm in diameter, with the study interval comprising the bottom 15 cm of the sample. Detrital material in speleothem calcite is typically avoided for U-series geochronology as it could contain external ^{230}Th that was not formed as a decay product within the calcite ^{238}U/^{230}Th closed system. This would result in an overestimation of the calculated age. Therefore, optimal layers selected for U-series dating were based on their lack of detrital content as determined by prescreening of layers with low ^{232}Th concentrations (< 1 ppb) (Table 7).

2.2 Stable Isotopes

Oxygen and carbon isotope samples were collected using a Taig Micro Mill mounted on an inclined frame. For stable isotope analysis, transects were milled along the growth axis using a 0.5 mm tungsten-carbide drill bit. Following removal of the upper 100 µm of the transect surface to exclude surface contaminants, samples (1.5 mm wide and 3 mm deep) were milled in continuous 100 µm steps. In total, 249 samples were analyzed for stable isotope ratios. To assess whether or not stable isotope values were affected by kinetic fractionation, we use adapted a version of the Hendy Test (Hendy, 1971). The traditional Hendy Test supports that calcite formed under equilibrium conditions if stable isotope values are similar laterally along the same growth layer. However, there are several limitations with the Hendy Test (Dorale and Liu, 2009; Mickler et al., 2006), including: (1)

equilibrium fractionation occurring along the central growth axis with concurrent kinetic fractionation along the flanks, and (2) difficulty resolving single growth layers. We drilled four separate transects variously offset (Fig. 3) left and right of the central growth axis. We attempt to overcome the first limitation by sampling multiple tracks within 1 cm of the central growth axis. Overlap between the transects enabled stratigraphic comparisons of stable isotopes within three horizons. To overcome the second limitation, the overlap between transects spans multiple layers so that we can compare an average of several layers rather than trying to resolve a single layer. For the MCN-1 offset intervals, standard deviations obtained for micromill samples sharing the same growth intervals were < 0.095 (1σ) for both carbon and oxygen isotopes (Table 6). These similarities are consistent with minimal kinetic effects. However, because of the closeness of the parallel transect positions (~1 cm), kinetic effects may affect stable isotope values more strongly in transects further from the growth axis. The effect of kinetic fractionation on McN-1 stable isotopes could be more robustly assessed through additional stable isotope transects located farther off-axis.

Stable isotope measurements were made at the University of Texas at Austin (UT Austin) using a 253 Isotope Ratio Mass Spectrometer (IRMS) interfaced with a Gasbench II sample introduction system. Approximately 250 μm of calcite powder was placed in Exetainer vials, which were flushed with ultra-high purity He for 8 minutes at ~100 ml/min. Phosphoric acid (103% H_3PO_4) was injected (0.10 mL) into the vials, and allowed to react with the carbonate samples at 50^o C for 2-8 hours. Sample CO_2 was introduced via continuous flow with 7-9 measurements collected over a period of 8 minutes. An in-house marble standard (UTM) was used to determine analytical uncertainty and correct for

analytical drift throughout each session analysis. External uncertainty for $\delta^{13}C$ is ± 0.08‰ (1σ) and for $\delta^{18}O$ is ± 0.05‰ (1σ) based on 50 UTM replicate analyses. Results are reported with respect to the VPDB standard, based on replicate analyses (n = 14) of the NIST (National Institute of Standards and Technology) standards NBS19 and NBS18 (Coplen, 1996). Accepted $\delta^{13}C$ values of NBS-19 and NBS-18 are 1.95‰ and -5.014‰, respectively. NBS-19 and NBS-18 accepted $\delta^{18}O$ values are -2‰ and -23.2‰, respectively (Friedman et al., 1982).

2.3 ^{14}C Measurements and Dead Carbon Proportion Calculation

Ten ^{14}C samples were collected as intact ~10 mg wafers of calcite to avoid contamination from atmospheric CO_2 (Gill et al., 1995). The calcite wafers were crushed and pretreated with a 50% HCl leach to remove any secondary carbonate. The samples were then hydrolyzed in 85% H_3PO_4 and graphitized. After graphitization, ^{14}C analysis was conducted on a NEC Compact (1.5 SDH) AMS system at the University of California Irvine. All results were corrected for isotopic fractionation following procedures of Stuiver and Polach (1977).

To quantify the amount of ^{14}C-free ("dead") carbon present in the speleothem calcite, we measure DCP. DCP is calculated using the measured speleothem ^{14}C activities ($a^{14}C_{meas}$) reported in fraction modern carbon (FMC) using the equation from Genty and Massault (1999) and Genty et al. (1999):

$$DCP = (1-a^{14}C_{init.}/\ a^{14}C_{atm.init.}) \cdot 100 \qquad \text{Equation 3}$$

where $a^{14}C_{atm.init.}$ is the ^{14}C activity of the atmosphere at the time of calcite precipitation, and $a^{14}C_{init.}$ is the ^{14}C activity of the speleothem at the time of calcite precipitation. $a^{14}C_{init}$ is calculated using Equation 4:

$$a^{14}C_{init} = a^{14}C_{meas.}/e^{(-\ln(2)/5730) * t)} \quad \text{Equation 4}$$

where $a^{14}C_{meas}$ is the activity of the measured speleothem calcite and t is the corresponding independent U-series age. The $a^{14}C_{atm.init.}$ are measured from the IntCal13 calibration curve (Reimer et al., 2013). The IntCal13 calibration curve presents Northern Hemisphere atmospheric ^{14}C activities over the past 50,000 yrs BP, as compiled from ^{14}C measurements of tree rings, plant macrofossils, speleothem, corals and foraminifera. Because IntCal13 has a 5-year sampling resolution, the assigned $^{14}C_{atm.init.}$ value is the nearest IntCal13 point to the U-series age. Reported DCP uncertainties are calculated by incorporating the errors from the U-series ages, IntCal13 values and ^{14}C activities (Table 4).

2.4 Lamina ^{232}Th and ^{238}U Concentration Analysis

Preferential lamina selected for U-series dating were determined based on analyses of ^{232}Th and ^{238}U concentrations. Forty-two laminae (Fig. 17) were selected for this screening to determine layers with low ^{232}Th (< 1 ppb) concentrations. Approximately 5 mg of calcite powder was collected along each lamina using a handheld dental drill with a 0.5 mm tungsten-carbide drill bit. The samples were gravimetrically diluted 200-fold with 2% trace metal grade HNO_3 to reduce the concentration of total dissolved solids to levels below 2,000 ppm. The analytes were measured on an Agilent 7500ce inductively coupled quadrupole mass spectrometer (ICP-Q-MS) at the UT Austin. Analyte signals were

measured in counts per second (cps) and were converted to concentration (ppb) by calibrating the system using a series of external standards of differing concentrations (5 calibration standards and one 2% HNO_3 blank). Correction factors derived from the linear regressions of the calibration standards were determined, and the measured cps was converted to concentration based on the respective calibration curve.

Accuracy and precision of the measured element concentrations were determined by analyzing two quality control (QC) standards. QC standards included two lab fortified matrix spikes (QC1 and QC2) that contained analytes close to the middle of the calibration range. To assess accuracy, recoveries were determined from each of the two QC standards by running replicate QC analyses (two replicates of QC1 and four replicates of QC2) and comparing the average of the replicate values to the actual values. Recoveries for both ^{232}Th and ^{238}U were all within 14% of the known concentrations, with the majority of sample recoveries being greater than 10%. Analyte concentrations were corrected for based on the respective dilution factor. The limit of detection (LOD) indicates the lowest concentration that can be detected with 95% confidence of the measurement being above background signal. Concentrations that are below the LOD are flagged as "< LOD". The LOD's were determined based on the statistical variance of the 17 2% HNO3 blank replicates, and are 0.009 and 0.003 ppb for ^{232}Th and ^{238}U, respectively. Five samples had measurable ^{232}Th above the LOD, with values that were > 1 ppb, and three samples had ^{238}U below the LOD. The 5 laminae with samples containing ^{232}Th concentrations > 1 ppb were avoided for U-series analysis. ^{238}U concentrations, QC standards, blanks and calibration standard values are shown in Table 7.

2.5 Uranium-series Dating

Uranium disequilibrium series (U-series) dating was used to obtain high-precision ages of growth laminae in stalagmite McN-1. Growth layers with minimal ^{232}Th were sampled (n = 31) using a handheld dental drill with a 0.5 mm tungsten-carbide drill bit, with approximately 0.15 g of calcite powder collected for each sample (Fig. 3). Twenty-five samples were analyzed on a Thermo-scientific Neptune Plus Multicollector-Inductively Coupled Plasma Mass Spectrometer (MC-ICP-MS) at the University of Minnesota Twin Cities, Minneapolis, Minnesota (UMN). Three samples (McN-IS-1, McN-IS-2, and McN-1b) were analyzed on a Thermo Scientific Triton Thermal Ionization Mass Spectrometer (TIMS) located at the UT Austin. Chemical separations, similar to those described in Musgrove et al. (2001), were conducted in a class 100 clean lab at either the UT Austin or at UMN. Measured $\delta^{234}U$ values of external standard NBL-112A for analytical sessions at UMN had a mean value of -38.1 ± 1.3‰ (2σ) (n=2). One internal NBL-112A standard was analyzed at UT with a value -37.7 ± 1.1‰ (2σ). These values are within the 2σ uncertainty of the long term history of NBL-112A measurements made at UT Austin and UMN, with $\delta^{234}U$ average values being -37.2 ± 1.8 (n=52), and -36.9 ± 1.0 (n=40), respectively. $\delta^{234}U_{initial}$ values express the per mil (‰) variation of the $^{234}U/^{238}U$ atomic ratio of a sample from the secular equilibrium ratio, and are corrected to their initial values. Full procedural blanks (FPB), including chemical separation and filament loading techniques, were measured to determine contamination during sample preparation (Table S7). FPB-1, FPB-2 and FPB-3 were processed at UT Austin, and FPB-4 was processed at UMN. values averaged <3 pg for U and <11 pg for Th, which is < 0.003%, and 0.6% of measured U and Th, respectively. Replicate samples were collected from McN-9, 25 and

28 (Table 1). Replicate sample calcite was separated immediately after drilling, and underwent the same chemical separation procedures as all other U-series samples. All replicate samples ages were within uncertainty of the original samples, where the 2σ standard deviations between original and replicate samples McN-9, McN-25 and McN-28 were 290, 28 and 245 years BP, respectively. Ages were calculated using the $^{230}Th/^{238}U$ decay equation determined by Broecker (1963) (see Appendix A for detailed description of U-series methodology).

2.6 Isochron Analysis and Initial $^{230}Th/^{232}Th$

Initial ^{230}Th concentrations are traditionally estimated from the concentration of ^{232}Th, assuming an initial $^{230}Th/^{232}Th$ ratio of 4.4 ± 2.2 ppm (Richards and Dorale, 2003). This ratio is based on a bulk-Earth U/Th ratio for material at secular equilibrium, but is poorly constrained in most systems. Due to the high ^{232}Th concentrations (> 1 ppb) of several McN-1 U-series samples, determining the initial $^{230}Th/^{232}Th$ ratio is necessary for constraining both U-series ages and their uncertainties. Measurements on modern calcite from Westcave Preserve (located in central Texas) have $^{230}Th/^{232}Th$ values that range from 6 to 15 ppm (Wortham et al., 2013). This suggests that central Texas speleothems may contain $^{230}Th/^{232}Th$ values that are higher than the commonly assumed bulk-Earth $^{230}Th/^{232}Th$ value (4.4 ± 2.2 ppm). We therefore use the isochron method to constrain the initial $^{230}Th/^{232}Th$ value and correct for contributions of detrital ^{230}Th (see Appendix A for a detailed description of the isochron methodology).

Three coeval samples with variable $^{238}U/^{232}Th$ were collected along the same

growth layer to produce an isochron-derived initial $^{230}Th/^{232}Th$ (Fig. 3). We sampled along two different layers (McN-7 and McN-8) to produce two unique isochrons. We used ISOPLOT 4.15 to calculate the isochron, given the U/Th activity ratios of the coeval samples (Ludwig and Titterington, 1994). The isochron-derived detrital $^{230}Th/^{232}Th$ value for McN-8 is 14.7 ± 3.8 ppm and for McN-7 is 27.0 ± 75.5 ppm (Table S5). Isochron coeval samples McN-7-2 and McN-7-3 contain similar ^{232}Th concentrations resulting in the Mean-Square Weighted Deviate (MSWD) and uncertainties of both the calculated age and $^{230}Th/^{232}Th_{inital}$ being an order of magnitude higher than values for the McN-8 isochron. A three-point isochron is contingent on there being a large enough difference in ^{232}Th concentrations between each point such that detrital ^{232}Th-free endmember isotopic ratios can be determined and a robust regression line can be developed (Fig. S1). The McN-7 isochron results in an initial $^{230}Th/^{232}Th$ uncertainty (±75.5 ppm) that is higher than the McN-8 isochron-derived $^{230}Th/^{232}Th$ value, and is not useful in constraining initial$^{230}Th/^{232}Th$. We use the McN-8 isochron-derived detrital $^{230}Th/^{232}Th$ of 14.7 ± 3.8 ppm in the calculation of all McN-1 U-series ages (see Appendix A). This value is within range of other $^{230}Th/^{232}Th$ values from central Texas speleothem calcite (6-15 ppm; Wortham et al., 2013).

2.7 Drip water Dissolved Inorganic Carbon Isotope Model

To quantify the changes in DCP and $\delta^{13}C$ as a result of changes in the carbonate dissolution regime, we use the calcite dissolution model from Fohlmeister et al. (2011). This model simulates variations in the ^{14}C activity and $\delta^{13}C$ values of drip water DIC

during calcite dissolution in the vadose zone. See Appendix A for detailed discussion of how model works.

The Fohlmeister et al. (2011) model is based on the dissolution model of Hendy (1971), where the concentrations of CO_3^{2-}, HCO_3^-, OH^-, H^+ and $CO_{2(aq)}$ are calculated using mass action relations, and Ca^{2+} is calculated from the condition of electroneutrality ($[H^+] + 2[Ca^{2+}] - [OH^-] - [HCO_3^-] - 2[CO_3^{2-}] = 0$). Values of $\delta^{13}C$ and ^{14}C are assigned to the initial $CO_{2(g)}$ (see Section 3.4). Initial pCO_2 is assumed, from which a pH value is calculated. In the first step, water is in equilibrium with $CO_{2(g)}$, and contains no Ca^{2+}. The next step considers calcite dissolution, with the model increasing the pH in 0.001 increments (based on dissolution of calcite increasing pH, making a more alkaline solution). At each pH increment, concentrations of all of the DIC species and OH^- are calculated assuming thermodynamic equilibrium under an open system using mass action relations, and Ca^{2+} is then calculated using the equation of electroneutrality. This procedure is repeated at successively higher input pH until $x \cdot Kc = Q$, where Q is the ion activity product and Kc is the equilibrium constant for the reaction:

$$Ca^{2+} + CO_3^{2-} \leftrightarrow CaCO_3$$

The open/closed system ratio (x) is the fractional approach toward equilibrium that occurs during open as opposed to closed system dissolution. Therefore, under a completely open system, $x = 1$ and $Q = Kc$ and thus the open system calculations described above are carried out until the solution is in equilibrium with calcite at the specified pCO_2. The model calculates all concentrations under open system conditions until the dissolution process stops when saturation with respect to calcite has been established ($Q = Kc$). If $0<x<1$, the

model will calculate the concentrations of the species under open system conditions until the pH value associated with Q = Kc·x is reached. When open system dissolution stops, the $\delta^{13}C$ values of all DIC species are calculated using temperature dependent fractionation factors listed in Mook and de Vries (2000) and the relative abundance of the species. The $\delta^{13}C$ value of total DIC is calculated by mass balance. This becomes the carbon reservoir, of both concentration and $\delta^{13}C$ values, that mixes with limestone carbon during closed system dissolution. The effect of pH on the speciation of DIC and the difference among $\delta^{13}C$ values of DIC species at equilibrium are what result in pCO_2 controlling final $\delta^{13}C$ values of drip water total DIC. From this point, the model calculates the remaining concentrations under closed system conditions until saturation is reached. If x = 0, Q = 0, and all $CaCO_3$ dissolution occurs under closed system conditions until saturation. For example, if x = 0.8, dissolution under an open system will stop when Q = 0.8·Kc. In this scenario, 80% of calcite dissolution occurs under an open system followed by 20% dissolution under a closed system.

$\delta^{13}C$ and ^{14}C values formed under closed system conditions consider the amount (and carbon isotope signature) of carbon coming from host rock dissolution. Mass conservation requires that under a closed system:

$$c_{CO_{2(aq),initial}} + c_{HCO_{3,initial}^-} + c_{CO_{3,initial}^{2-}} + c_{Ca^{2+}} = c_{CO_{2(aq)}} + c_{HCO_3^-} + c_{CO_3^{2-}}, \quad \text{Equation 5}$$

where initial concentrations refer to DIC species before any dissolution. The change in Ca^{2+} accounts for the amount of carbon added from calcite dissolution. The $\delta^{13}C$ values of

total DIC formed under closed system dissolution are calculated using the isotope fractionation factors described in Mook and de Vries (2000) and equation 6:

$$\delta^{13}C_t(n) = (\delta^{13}C_t(n-1) \cdot \sum c_j(n-1) + \delta^{13}C_{CaCO_3} \cdot (c_{Ca^{2+}}(n) - c_{Ca^{2+}}(n-1))) \Big/ \sum c_j(n), \quad \text{Equation 6}$$

where n = the current dissolution step, c_j is the concentration of the DIC species, and $\delta^{13}C_{CaCO3}$ is the $\delta^{13}C$ value of the host rock. ^{14}C activity is also computed using equation 6 and fractionation factors described in and Salieges and Fontes (1984). Changes in ^{14}C activities and $\delta^{13}C$ values of total DIC are modeled across various initial pCO_2 values and open/closed system ratios (Fig. 4).

2.8 Petrography

The study interval at the base of McN-1 consists primarily of translucent, columnar calcite, with three prominent horizons of darker laminae (which we assume to be detrital-rich material) near the bottom 20 cm (Fig. 3). High-resolution scanned images of the polished slab face and thin sections were petrographically examined to document laminae thicknesses, mineral fabric and porosity. Three epoxy-embedded thin section (150 µm thick), spanning the basal 40 mm of McN-1, were prepared at the UT Austin (UT Austin) and examined under transmitted-light and reflected-light microscopy (Zeiss Axioskop 40 microscope).

CHAPTER 3: RESULTS

3.1 Petrography

Macroscopic observations of the basal McN-1 polished slab and thin section reveal a gradual transition from thick, highly porous, opaque white lamina to thinner translucent, dense lamina from 12,200 to 11,600 years BP (Fig. 8, Interval A). The porous, opaque lamina vary from 0.5 to 1 mm in thickness. A sharp transition to brown-tan lamina occurs at ~11,600 yrs BP (Fig. 8, Interval B), with lamina thicknesses decreasing to ~0.05 mm. These darker laminae have increased detrital content (as shown by higher ^{232}Th concentrations) and correspond with the onset of the Holocene (Fig. 8). The onset of these detrital layers also corresponds with an abrupt slowing of growth through the early Holocene from 93 μm/year to 5 μm/year (Fig. 6).

A gradual transition from the dark lamina to dense, translucent lamina occurs at ~54 cm from the top. This denser, translucent calcite section extends over 3 cm and spans the period from ~9,600 to 8,600 yrs BP (Fig. 8, Interval C). A gradual transition into brown-tan lamina occurs at 51.5 cm from the top and extends 2 cm (Fig. 8, Interval D), and are similar in appearance and color with the dark lamina from Interval B. However, Interval D laminae are relatively flatter near the growth axis. Dreybrodt (1999) show that increased drip rate can increase the radius of a speleothem and create flatter lamina. The flatter lamina in Interval D correspond with the fastest McN-1 growth rates (~130 μm/year). Another gradual transition into dense, translucent lamina extends from 47-49 cm (Interval E). The porous, opaque laminae are characterized by fast growth, variable thickness and high porosity. The translucent laminae are characterized by relatively constant thicknesses and

higher density, and the brown-tan lamina are characterized by variable laminae thicknesses, higher density and thinning towards the flanks.

3.2 U-Th Chronology and Growth Rates

^{238}U concentrations from McN-1 U-series ages range from 100 - 680 ppb. We use the isochron-derived $^{230}Th/^{232}Th$ of 14.7 ± 3.8 ppm to constrain the amount of detrital ^{230}Th and reduce the U-Th age uncertainty. However, several U-series samples had ^{232}Th concentrations exceeding 1 ppb, resulting in age uncertainties beyond 5%. McN-1 $\delta^{234}U$ values range from 104 to 145‰. McN-1 ^{238}U and ^{232}Th concentrations are similar to speleothems from other Edwards plateau caves that cover the same time period, including speleothems from Cave Without A Name (CWN-4; Feng et al., 2014), and Natural Bridge Caverns (NBJ; Wong et al., 2015). ^{238}U concentrations for CWN-4 range from 220 - 410 ppb, and NBJ ^{238}U concentrations range from 160 - 330 ppb. CWN-4 ^{232}Th concentrations show similar detrital contamination, with several ages having > 1 ppb, while NBJ has less ^{232}Th (< 0.2 ppb). NBJ initial $\delta^{234}U$ values are consistent with McN-1 (~150‰), whereas CWN-4 $\delta^{234}U$ values are three times higher (~340‰). The corrected ^{230}Th ages, measured ^{238}U and ^{232}Th concentrations, δ^{234} U, and $^{230}Th/^{232}Th$ activities for McN-1 are listed in Table 1.

An age vs. depth profile (Fig. 5) was constructed from the reported U-series ages (and 2σ uncertainties) and datums using a Monte Carlo simulation statistical model COPRA (Breitenbach et al., 2012). A piecewise cubic Hermite interpolating polynomial (PCHIP) was used to construct the age-depth profile with 2,000 Monte Carlo increments. The PCHIP is a polynomial with one continuous derivative that conserves the monotonicity

and shape of the age vs. depth data, with hiatuses preserved as abrupt changes in growth rates. Seven U-series ages with uncertainties greater than 5% of the calculated age were not used in the final age model. McN-1 stable isotope and DCP time series are ultimately constrained by 15 U-Th dates, ranging from 12,300 to 6,800 yrs BP, within the bottom 15 cm of the studied stalagmite section.

Growth rates are calculated using the distances (in μm) and ages between contiguous U-series datums. McN-1 growth rates range from 3 to 193 μm/year (Fig. 6; Table 9). Relatively fast growth occurs between 12,200 – 11,800 years BP, with an average of 93 μm/year. This fast growth coincides with the low ^{232}Th content layers and during the end of the Younger Dryas. Growth rates decrease substantially after 11,800 years BP, with average values of 5 μm/year until ~8,700 years BP. A significant increase in growth of ~130 μm/year occurs between 8,700 – 8,200 years BP, at which point growth ceased, with a hiatus between 8,200 and 7,100 years BP (Fig. 6).

3.3 Stable Isotopes, ^{14}C and Dead Carbon Proportion

Between 12,200 and 11,600 yrs BP, McN-1 δ^{13}C values average -4 ± 0.6‰ (Fig. 7), before rapidly decreasing to ~ -7.5‰ near the end of the Younger Dryas (11,700 yrs BP). According to our age model, this sharp negative δ^{13}C excursion occurs within approximately 230 years. Extending through the early Holocene portion of the record (11,700 – 7,200 yrs BP), δ^{13}C values show little variability (averaging -8‰), except for a prominent increase from -9 to -6‰ between ~8,600 and 8,200 yrs BP, which coincides with the fastest growth rate interval in the McN-1 record (~130 μm/year from 8,700 – 8,200 yrs BP).

McN-1 $\delta^{18}O$ values range from -5.3 to -2.6‰ throughout the entire record. Values at the base of McN-1 between 12,200 to 12,100 years BP define an increase in $\delta^{18}O$ from -4 to -2.6‰, followed by an abrupt decrease to -4.6‰ by 11,900 yrs BP. An abrupt increase to -3.1‰ occurs at 11,850 yrs BP. From ~11,800 yrs BP, $\delta^{18}O$ values steadily decrease and remain near -4.5‰ throughout the Holocene. Compared to the $\delta^{13}C$ record, the YD and Holocene portions of the $\delta^{18}O$ record are more variable, without an excursion across the YD-Holocene boundary. McN-1 $\delta^{18}O$ values are consistent with mean CWN-4 $\delta^{18}O$ values (-3.5‰) that span the YD and early Holocene, and NBJ $\delta^{18}O$ values (-3.8 to -4.8‰) that span the middle-late Holocene (Fig. 12; Feng et al., 2014; Wong et al., 2010). Modern speleothem calcite from central Texas caves (Inner Space Cavern and Natural Bridge Caverns; Fig. 1) show similar $\delta^{18}O$ values ranging from -6 to -4‰ (Pape et al., 2010; Feng et al., 2012). Modern drip water from these caves has a mean $\delta^{18}O$ value of -3.4 ± 2‰ SMOW. The similarities between ancient and modern central Texas speleothem $\delta^{18}O$ values may suggest that moisture source (e.g. Gulf of Mexico) has been a primary control on central Texas speleothem $\delta^{18}O$ from the onset of the Holocene (see Section 4.3; Feng et al., 2014).

McN-1 ^{14}C activities range from 25.5 to 41.0 pMC, while DCP values range from 0 to 7.8%, with DCP errors ranging from 0.8 to 3.8% (2σ). DCP measurements spanning the YD (12,200 – 11,700 yrs BP) average 7.5%. DCP measured on both sides of the negative $\delta^{13}C$ shift (Fig. 7), at ~11,670 yrs BP, indicate a concurrent reduction in DCP to 0%. Three younger DCP measurements, spanning 10,500 - 11,600 yrs BP, decrease to 0%. DCP increases from 0 to 4% after 10,000 yrs BP, at which point $\delta^{13}C$ values remains

relatively low and do not follow a similar increasing trend. However, DCP values are still lower during the later portion of the Holocene than during the YD (Fig. 7). Speleothem DCP values below 0% are not possible, as this would indicate speleothem ^{14}C activity that was higher than that of the atmosphere. We attribute calculated negative DCP values to errors associated with age assignment (U-series or IntCal13 ages) or ^{14}C activity measurement. These errors result in overestimated $a^{14}C_{atm.init.}$ values. However, all negative DCP values fall within uncertainty of 0% (Fig. 7). DCP errors are calculated from uncertainties in $a^{14}C_{atm.init}$ and speleothem $a^{14}C$. Table 4 shows ^{14}C activities and calculated DCP values.

Initial $\delta^{234}U$ values range from 120 to 146‰ (Fig. 7), with apparent cotemporaneous shifts with both $\delta^{13}C$ and DCP excursions. $\delta^{234}U$ values spanning 12,200 – 11,700 yrs BP average 145‰, with a decrease to 113‰ at 10,500 yrs BP. This decrease is consistent with the abrupt decreases in both $\delta^{13}C$ (by 2.8‰) and DCP (by 7.5%) values at the YD-Holocene transition. $\delta^{234}U$ values increase to ~130‰ until 8,500 yrs BP, where an abrupt increase to 146‰ is observed and consistent in timing with an increase in $\delta^{13}C$ (-9 to -6‰).

3.4 Drip water Dissolved Inorganic Carbon Isotope Model

We compare two time intervals across the YD/Holocene boundary in McN-1 to assess the change in epikarst moisture state across this transition (Fig. 13). These intervals are defined based on the higher resolution $\delta^{13}C$ record (compared to DCP), and the stratigraphic position of the distinctive negative $\delta^{13}C$ excursion. Integrating constraints from the age model, the negative $\delta^{13}C$ shift began at 11,624 ± 180 yrs BP. Accordingly,

we define for McN-1 the late-YD interval (LYD) from samples with ages between 12,200 – 11,603 yrs BP, and the early Holocene interval (EHO) as samples with ages between 11,603 – 10,488 yrs BP (Fig. 13). We chose to limit EHO to the earliest Holocene portion of sampling distribution in order to understand the changes in mean moisture state across the local YD/Holocene transition. Based on mean $\delta^{13}C$ and DCP values from both intervals, $\delta^{13}C$ undergoes a negative shift of 2.8‰ (-3.8 to -6.6‰) over the same time that DCP undergoes a 7.5% (7.5 to 0%) reduction. The lower DCP and $\delta^{13}C$ values during EHO suggest a decrease in host rock carbon contribution relative to LYD, corresponding to a decrease in epikarst moisture level.

To quantify the change in the McN-1 carbonate dissolution regime required to account for the magnitudes of the observed negative shifts in $\delta^{13}C$ (by 2.8‰) and DCP (by 7.5%) across the LYD-EHO transition, we modeled the carbon isotope values of DIC in drip water following equilibration with calcite under varying initial pCO_2 and open/closed system limestone dissolution (Fig. 4). The model requires several initial soil-epikarst system boundary assumptions (specifically, the initial $\delta^{13}C$ and ^{14}C values of the $CO_{2(g)}$, temperature, and soil pCO_2), which we constrain from modern and paleoclimate data from regional caves and soils. We chose a model system temperature of 15°C based on paleoclimate temperature data compiled for the southwest U.S during the YD-Holocene transition (13-17° C, Cole and Arundel, 2005), and a pCO_2 value of 20,000 ppm based on soil pCO_2 concentrations above modern central Texas caves (Breecker et al., 2012). Soil organic carbon (SOC) from soils collected in south central Texas that spanned the YD have $\delta^{13}C$ values ranging from -25 to -20‰ (Holliday et. al, 2011). Therefore, we selected -22‰

for initial CO_2 $\delta^{13}C$. Although modeled drip water DIC $\delta^{13}C$ values are not similar to the measured McN-1 speleothem $\delta^{13}C$ values (suggesting other processes not considered in the model affect McN-1 $\delta^{13}C$), constraining the $\delta^{13}C$ of respired CO_2 is important, because a larger difference between respired CO_2 and limestone $\delta^{13}C$ will result in a larger calculated drip water DIC $\delta^{13}C$ shift. Our modeling goal is to account for the magnitude of the shift, rather than the absolute values of the $\delta^{13}C$ shift. Because carbon sources for McN-1 are likely to be > 200 yrs, based on ^{14}C activities of SOM values overlying central Texas caves, we selected initial CO_2 ^{14}C values of 100 pMC (Bergel et al., in press). Modeling of drip water DIC carbon isotope values using the proxy-defined endmember temperatures (13 and 17°C) result in changes in the shifts of $\delta^{13}C$ to be less than 0.05‰ (<4% of model results using our selected temperature). Varying initial $\delta^{13}C$ (-25 to -20‰) and initial ^{14}C (120-80 pMC) values result in changes in the magnitude of the drip water DIC $\delta^{13}C$ and ^{14}C shifts of less than 5% of results using our selected parameters.

After converting ^{14}C activities to DCP, our model (Fig. 4) predicts changes for drip water DIC $\delta^{13}C$ and DCP as a result of changes in epikarst pCO_2 and various open/closed system ratios. Iso-pCO_2 lines are shown across the modeled open/closed system lines and connect same initial soil gas pCO_2 values. The upper open/closed system line represents the DIC carbon isotope composition of a saturated solution formed under open system conditions, and the lowest line shows the carbon isotope composition under closed system conditions (Fig. 4). Our model demonstrates that a change from 7.5 to 0% in drip water DCP along a pCO_2 line of 20,000 ppm results from an open/closed system shift from 40/60 to 100/0. A shift in the open/closed system ratio of this magnitude causes modeled drip

water DIC $\delta^{13}C$ to decrease by 0.68‰. This represents only 25% of the total $\delta^{13}C$ shift, suggesting that other processes are responsible for the majority (75%) of the $\delta^{13}C$ shift. As shown in Fig. 4, changes in open/closed system ratios result in large variations of drip water DIC DCP and relatively moderate variations in $\delta^{13}C$. Figure 4 shows that along a specific pCO_2 line, a shift from a completely open to closed system results in a shift in DCP of ~ 50%, but only a 2‰ shift in $\delta^{13}C$. The relatively smaller changes in $\delta^{13}C$ related to changes between open and closed system conditions is likely due to differences in pH of the solution. For the end member open system dissolution, pH is relatively high because water is fully equilibrated with calcite. The high pH results in increased concentrations of the isotopically heavier DIC species (CO_2^{3-}), resulting in higher total DIC $\delta^{13}C$ values. For the closed system, the pH is relatively low initially. The initiation of closed system dissolution in the model occurs at point when open system dissolution ends, which is the transition point in the model where the $\delta^{13}C$ value of total DIC mixed with limestone carbon is calculated. For the 100% closed system scenario, no calcite dissolution has yet occurred. Therefore, the pH is lower, resulting in $\delta^{13}C$ values of total DIC that are lower the total $\delta^{13}C$ values of DIC in the 100% open system scenario. Mixing with limestone then increases the $\delta^{13}C$ value of total DIC in the closed system scenario, a process that doesn't occur in the open system scenario. Therefore, changes to $\delta^{13}C$ values under open and closed systems purely as a result of solution pH cause the $\delta^{13}C$ values to move in the opposite direction from shifts caused by variable contributions of isotopically heavier limestone carbon. The magnitude of change in $\delta^{13}C$ values is muted relative to what would be expected if pH of the water were the same between both systems.

CHAPTER 4: DISCUSSION

In the following sections, we assess changes in epikarst moisture at McN-1 during the YD-Holocene transition using $\delta^{13}C$ and dead carbon proportion (DCP) variations, speleothem fabrics, growth rates and $\delta^{234}U$. Carbonate dissolution model results suggest changes in the carbonate dissolution regime were a minor control on McN-1 $\delta^{13}C$ values during the negative shift at the YD-Holocene transition. We address other potential mechanisms that could explain the remainder of the negative shift in $\delta^{13}C$ values (see Section 4.6). We also assess how changes in growth rates, speleothem fabrics and the transition from a partially open to fully open dissolution system during the YD-Holocene transition affect epikarst moisture (see Sections 4.1 and 4.2). We then compare McN-1 moisture proxy results to other regional proxy records, which show a similar drying trend beginning at the onset of the Holocene (see Section 4.7).

4.1 Growth Rates and Moisture Amount

Speleothem growth rates have been used to proxy moisture amount, where a positive correlation between rainfall amount, drip rate and growth rate has been shown (Baker et al., 1993; Polyak and Asmerom, 2001). Empirical evidence from cave monitoring studies in central Texas suggest that drip rates can control calcite growth at inter-annual timescales, while cave-air pCO_2 is shown to control speleothem growth seasonally, via seasonal ventilation of cave atmospheres in this region (Banner et al., 2007). Based on the centennial timescales of this study, and disregarding any geomorphological changes in the cave that resulted in ventilation regime changes (such as sinkhole development), seasonal changes

in cave-air pCO_2 (such that ventilation was low enough to allow calcite precipitation) are not expected to be a primary control on changes observed in the McN-1 growth rates. If rainfall amount is the dominant control on growth rates, then the McN-1 record suggests that the end of the YD (12,200 - 11,700 yrs BP), as shown by relatively fast growth (~93 μm/year), was wetter than the Early Holocene (11,700-8,700 yrs BP; Fig. 6). Based on the growth rate record, conditions remained dry through the Holocene with average growth rates of 5 μm/year. A ~400 year period spanning 8,700-8,300 years BP experienced substantially faster growth (< 25 x higher; 130 μm/year) than the preceding drier early Holocene, indicating relatively wetter conditions. Growth rates negatively correlate with $\delta^{13}C$ values, as shown by the abrupt decrease in growth rates at the end of the YD (Fig. 6), that coincides with the negative 3‰ $\delta^{13}C$. Similarly, the prominent increase in $\delta^{13}C$ from -9 to -6‰ between ~8,600 and 8,200 yrs BP corresponds with the onset of highest McN-1 growth rates (~130 μm/year), which span 8,700 – 8,200 yrs BP.

Calcite growth is also controlled by several additional factors, including: water-film thickness, degassing rates via changes in cave-air pCO_2, concentration of dissolved Ca^{2+} in the solution and temperature (Dreybrodt, 1988). For these reasons, we use the growth rate results in conjunction with other McN-1 moisture proxies (carbon isotopes and fabrics) to better constrain moisture conditions over the YD-Holocene transition. The correlation between McN-1 growth rates, carbon isotopes and fabrics suggest that moisture amount is controlling growth rates.

4.2 Petrography

Lamina in speleothems may form over time from changes in organic acids, detrital mineral particles, fluid inclusions, changes in fabrics, mineralogy, or trace element incorporation into the crystal lattice, and can result from seasonal to stochastic events (Fairchild et al., 2001; Boch et al., 2011). The decrease in $\delta^{13}C$ and DCP occur over the same time interval in McN-1 (55 cm from the top; Fig. 7), and directly coincide with the onset of brown-tan lamina (Fig. 18).

Speleothem fabrics can provide valuable information about geochemical alteration and post-depositional processes resulting from changes in hydrology, which may complement paleoclimate proxy data (Frisia et al., 2000; Frisia and Borsato, 2010). McN-1 is composed of columnar calcite, where both acute and equant rhombohedra dominate the crystal form (Frisia et al., 2000; Dickson, 1993). Dense calcite forms via complete coalescence of multiple small stacked crystal units known as crystallites (Kendall and Broughton, 1978). These layers show a compact columnar fabric (C) where inter-crystalline porosity is not visible under an optical microscope. The presence of inclusions and higher porosity indicates incomplete coalescence and columnar open fabric (Co). These fabric classifications can be controlled by karst hydrology, where under relatively fast drip rates and a thick fluid film, crystals grow too fast to allow for incomplete coalescence and columnar open fabric (Kendall and Broughton, 1978), and alternatively, slower drip rates result in complete coalescence and columnar compact fabric (C). We identify mineral fabrics across McN-1 as either columnar open or columnar compact according to Frisia et al., (2015) (Figs. 10-12). Based on these classifications, the YD portion of McN-1 containing columnar open fabric would have formed under faster drips

and correspond with the relatively faster growth during the YD (Fig. 8). Similarly, the denser and columnar compact fabric observed in the Holocene portion of McN-1 would have formed under slower drip rates, where the dominant fabric type in Intervals B and C are concurrent with relatively slower growth (Fig. 6). Interval D (Fig. 8) contains columnar open fabric that spans ~8,500 to 8,300 yrs BP and is contemporaneous with the fastest McN-1 growth rates (~130 μm/yr). The concurrent transition of both fabric type and growth rates near the basal portion of McN-1 suggests similar climatological controls affecting both speleothem growth and fabric variation (Fig. 6).

Clay-rich soils of the Edwards Plateau are a potential source for detrital material inferred for the brown-tan lamina. Based on mineralogical and geochemical differences between the Edwards Limestone and overlying soils, Cooke et al. (2007) indicate the Edwards Limestone is only a minor source for silicate material found in overlying soils. The primary soil silicate source is instead suggested to derive from the Del Rio Clay, with lesser contributions from central Texas dust. The Del Rio Clay consists largely of illite, kaolinite and quartz, and does not presently overly the cave (Cooke et al., 2007). Accumulation of non-carbonate materials (i.e. silicates, oxides, organic matter) onto speleothems can occur by several processes, including fluvial transport during cave flooding events, solid phase infiltration from soils, or directly to the speleothem surface via eolian processes (Fairchild and Treble, 2009; Gonzalez-Lemos et al., 2014). Materials can also be transported in suspension from soils via drip water, or solution transport from soil, where soil elements (such as Fe, Mn, Mg, and K) are deposited as oxides. Central Texas dust deposited on the speleothem could be derived from the overlying soil source as well as direct accumulation by eolian transport to the cave (Cooke et al., 2007). Results of

geochemical analysis of the brown-tan lamina in McN-1 by laser-ablation ICP-MS are consistent with these laminae being enriched in soil-derived silicate components (Gilchrist, personal communication)

4.3 Comparison with Central Texas Speleothem CWN-4

We compare McN-1 to a central Texas speleothem record (CWN-4), located ~100 km to the southwest, that spans a similar time period (19,000 – 9,500 yrs BP). Feng et al. (2014) assessed the relationship between speleothem $\delta^{18}O$ and moisture sources in the US SW. Based on the close correspondence between changes in CWN-4 $\delta^{18}O$ and Gulf of Mexico foraminferal $\delta^{18}O$ records during the last deglacial (notably featuring coincident negative $\delta^{18}O$ excursions attributed to the influx of isotopically light deglacial meltwater to the Gulf of Mexico), in addition to tracking of modern rainfall over the region, they concluded that Gulf of Mexico seawater is the most significant moisture source for central Texas. Although there is no discernable abrupt climate signal in the McN-1 $\delta^{18}O$ record that can be unambiguously tied to a Gulf of Mexico moisture proxy (as is represented in CWN-4), mean McN-1 $\delta^{18}O$ values (-4.1‰) are consistent with mean CWN-4 $\delta^{18}O$ values (-3.3‰) that span the YD and early Holocene (Fig. 17). The CWN-4 record has a hiatus that begins at 12,300 yrs BP, so there is no period of overlap around the YD-Holocene transition. Therefore, the McN-1 $\delta^{18}O$ record may provide missing context for changes in the Gulf of Mexico over this time. The overall trend showing decreasing $\delta^{18}O$ values from ~-3 to -4.5‰ through the early Holocene (Fig. 17) may indicate the Gulf of Mexico became isotopically lighter, either from meltwater input (although, no proxy records indicate a

constant meltwater influx spanning the early Holocene), or increased contribution from isotopically lighter moisture sources (such as the Pacific Ocean).

CWN-4 $\delta^{13}C$ values spanning the same time interval as the McN-1 time series average -4.75‰, and show no obvious correlation with McN-1 $\delta^{13}C$ (Fig. 17). Due to the hiatus in the CWN-4 record spanning 12,300 - 9,900 yrs BP, we cannot compare McN-1 and CWN-4 $\delta^{13}C$ values around the end of the YD, near the negative $\delta^{13}C$ shift. However, CWN-4 $\delta^{13}C$ values during the Holocene are approximately 3‰ higher than McN-1 during the same time span, and are similar to CWN-4 $\delta^{13}C$ values during the YD. This suggests that the processes controlling the CWN-4 $\delta^{13}C$ record are different from those controlling McN-1. Differences in processes controlling $\delta^{13}C$ between the two records could include kinetic fractionation, enhanced PCP, differences between epikarst thickness affecting open/closed system conditions, or changes in vegetation type dominating the $\delta^{13}C$ signal.

4.4 $\delta^{13}C$ – Dead Carbon Proportion Correlation

Both McN-1 DCP and $\delta^{13}C$ values decrease over 12,200-10,500 yrs BP with a high correlation (r^2=0.75, n=7). This correlation suggests that DCP and $\delta^{13}C$ could be responding to the same changes in environmental/climate conditions. Environmental factors that result in a positive correlation between $\delta^{13}C$ and DCP are limited. Speleothem DCP represents the contribution of carbon from bedrock and/or OM, where a positive correlation between speleothem $\delta^{13}C$ and DCP can result from changes in closed versus open system behavior within the epikarst dissolution regime (Fig. 16; Fohlmeister et al., 2010; Griffiths et al., 2012; Noronha et al., 2014). In an open system, there is a limitless

volume of gas and thus the isotopic composition of DIC is controlled by respired CO_2. Increased epikarst moisture limits the volume of gas with which epikarst water can exchange and thus results in a non-zero effect on the isotopic composition of DIC from limestone dissolution. The larger the water/gas volume ratio, the larger the effect that limestone dissolution has on the DIC isotope composition. In a perfectly closed epikarst system, soil-limestone pore spaces are completely filled with water with no CO_2 gas present, resulting in DIC DCP values of 50% (assuming all calcite dissolution occurs under these conditions) (Hendy, 1971). Open system dissolution is favored by drier conditions due to the unlimited supply of OM-derived CO_2 gas (Fig. 16).

Changes in SOM turnover times may control DCP levels (Genty et al., 2001; Oster et al., 2010), with relatively slower turnover rates leading to higher DCP as a result of organic matter producing older CO_2. The McN-1 study area is currently characterized by thin soils and with juniper savanna and woodlands vegetation cover. However, there is evidence of thicker soil coverage (~0.5 to 2 m) over the Edwards Plateau prior to extensive erosion during the late Pleistocene to early Holocene (Cooke et al., 2003, 2007). Thicker soils during the YD may have had slower SOM turnover times and higher DCP. Although, studies of central Texas caves suggest that OM from deeply rooted plants is the primary source of speleothem carbon, not SOM (Breecker, et al., 2012; Meyer et al., 2014). Some contribution to DCP from SOM turnover rates should be considered; however, changes to speleothem DCP as a result of SOM turnover rates would be transferred over centennial-millennial time scales (Trumbore et al., 1996; Noronha et al, 2015; Bergel et al., in press). Given the abrupt nature and magnitude of the shift in DCP, we suggest that SOM turnover rates played a minor role in the DCP excursion.

We collected published DCP data from modern speleothem localities, along with annual rainfall totals, to look for trends between modern rainfall and speleothem DCP (Table 5) that may serve as a relevant analog for the McN-1 record. Although regional karst variations (i.e. porosity, thicknesses, carbon source) could influence extents of limestone dissolution, and thereby, DCP values, we find that highest speleothem DCP values are from high annual rainfall regions, whereas lower speleothem DCP values correspond to regions with lower annual rainfall. For example, speleothem DCP values in the range of ~30-40% occur in Indonesian and Scottish cave with annual rainfall on the order of ~2,000 mm/yr (Griffiths et al., 2012; and Genty et al., 1999); speleothem DCP values from Heshang Cave in southwest China range from 9-13%, with annual precipitation between 1,300 and 1,500 mm/yr (Noronha et al., 2014); and two modern speleothem localities from SW France have average DCP values of ~9%, where annual rainfall totals 900 mm/yr (NOAA; Genty and Massault, 1999). Speleothem DCP and annual rainfall for all listed sites in Table 5 are positively correlated (r^2=0.68, n=8; Figure 12), suggesting a moderate linkage between DCP and rainfall. The differences between karst from various regions (i.e. porosity, thicknesses, carbon source) could result in differences in how climate affects regional limestone dissolution, and thereby, DCP values. Also, a change in the speleothem DCP does not necessarily suggest that a correlation-derived proportional increase in rainfall has occurred. This correlation only suggests that rainfall is one of the factors controlling DCP, and a direct quantitative analysis of rainfall changes should not be assumed for our data compilation. However, the McN-1 record does correspond to drier localities in this compilation, with DCP values ranging from 0 and 8% and annual rainfall totaling ~800 mm/yr.

4.5 McN-1 $\delta^{234}U_{inital}$ Time Series

McN-1 $\delta^{234}U$ values show positively correlated, contemporaneous shifts with $\delta^{13}C$, DCP, and growth rates at both the YD-Holocene transition and at 8,500 yrs BP. Initial $\delta^{234}U$ values have been used to proxy groundwater-bedrock interaction and water residence times above caves (Ayalon et al., 1999; Zhou et al., 2005; Griffiths et al., 2010; Polyak et al., 2012). $\delta^{234}U$ is the per mil (‰) variation of the $^{234}U/^{238}U$ atomic ratio, which we correct to initial speleothem calcite values using $\delta^{234}U_{initial} = \delta^{234}U_{measured} \cdot e^{\lambda_{234} \cdot T}$, where T = ^{230}Th age. ^{234}U is a daughter product of ^{238}U decay. In bedrock, ^{234}U can be transferred to the surrounding water, either directly from crystal surface or via weakening of the ^{234}U lattice site from alpha-recoil damage. Therefore, ^{234}U is prone to selective weathering by variable conditions of groundwater interaction. Calcite precipitating from these waters can have ^{234}U values greater than 0, particularly in arid regions (Zhou et al., 2005). Common interpretations of speleothem ^{234}U values propose a model in which slower infiltration rates and associated longer water residence times, caused by dry epikarst conditions, result in higher proportions of ^{234}U relative to ^{238}U incorporated into the water (Ayalon et al., 1999; Griffiths et al., 2010; Polyak et al., 2012). If pore spaces within the bedrock are fully saturated, then by this model, changes in the flow of water (and residence time) would result in $\delta^{234}U$ values that are negatively correlated with water flow. However, lower amounts of water in the epikarst could also reduce the extent of weathering (due to less pore water surface area), particularly if conditions are very dry, in which case the leaching ^{234}U into groundwater wound be lower.

A decrease in McN-1 $\delta^{234}U$ values (145 to 115‰) between 11,700 to 10,500 yrs BP, and subsequent increase in $\delta^{234}U$ values (130 to 145‰) at 8,500 yrs BP is consistent in timing with parallel shifts in $\delta^{13}C$, DCP and growth rates (Fig. 7). The very dry conditions during the early Holocene (as suggested by DCP values near 0%, and growth rates as low as 3 μm/yr) could have reduced bedrock weathering, resulting in relatively lower $\delta^{234}U$ values. The increase in moisture at ~8,700 yrs BP could have increased weathering, consistent with the abrupt increase in $\delta^{234}U$.

4.6 Drip Water Dissolved Inorganic Carbon Isotope Model

The next two sections address the moisture change in the epikarst, and explain the significant controls on $\delta^{13}C$ during the YD-Holocene transition. We incorporate the drip water DIC carbon isotope model (see Section 2.6) to quantify the relationship between McN-1 DCP and $\delta^{13}C$ based on the values spanning the prescribed intervals LYD and EHO (Fig. 13). Increases in pCO_2 decrease the $\delta^{13}C$ of the drip water DIC. This is due to shifts in DIC speciation ($CO_{2(aq)}$, HCO_3^-, CO_3^{2-}), and their different fractionation factors, as a result of changes in pCO_2 (pH; Dulinski and Rozanski, 1990). An increase in pH increases the concentration of the CO_2 species, which has a relatively lower $\delta^{13}C$ value than other DIC species, and therefore decreases the $\delta^{13}C$ of the total DIC of the drip water. Under equilibrium conditions, each DIC species has a $\delta^{13}C$ value that either changes with temperature or with variable open/closed system conditions, but does not change with changes in pH (Dulinski and Rozanski, 1990). For our DIC carbon isotope model, we wish to constrain how drip water $\delta^{13}C$ is affected by changing open/closed system (dissolution

regime) conditions of the epikarst, before any CO_2 degassing and calcite precipitation along the flow path has occurred, in order to quantify the range of $\delta^{13}C$ variation that could be transferred to speleothem calcite. We are interested in whether or not the shift in McN-1 $\delta^{13}C$ can be explained by changes in the dissolution regime without changing initial pCO_2, therefore, therefore, we identify changes occurring along a selected iso-pCO_2 line.

Modeled results show a change in the open/closed system ratio from LYD to EDO as transitioning from 40/60 to 100/0 (Fig. 4). In an open system (open/closed system ratio of 100/0), there is an infinite gas/water ratio in epikarst pore spaces, which results from either 1.) a large number of gas-filled pore spaces relative to water-filled pore spaces, or 2.) exchange with atmospheric gas via ventilation or diffusion. The former is controlled by the amount of water in the epikarst, where progressively closed system behavior results in gas/water ratio of the pore space to decrease with the addition of water (Fig. 16). However, as mentioned in the second process above, closed system dissolution can occur under conditions with minimal pore gas exchange, and not be dependent on moisture. Our model does not distinguish between these two scenarios. If the modeled open/closed system values are representative of changes in vadose zone moisture, the modeled DCP shift in McN-1 indicates a change from a partially closed system during LYD to an entirely open system (with no water occupying soil pore space) during EHO. The modeled change in $\delta^{13}C$ attributed to the carbonate dissolution regime is -0.68‰, which explains 25% of the total -2.8‰ change in $\delta^{13}C$ from LYD to EHO. Based on our calcite dissolution model, changes in the carbonate dissolution regime do not explain the majority of the $\delta^{13}C$ shift at the YD-Holocene transition, where the majority $\delta^{13}C$ variability is probably controlled by other processes.

As mentioned in Section 3.3, several assumptions and boundary conditions are used in the DIC carbon isotope model to constrain temperature, initial pCO_2 and carbon isotope values. Some of these assumptions are based on sparse paleoclimate data (Cole and Arundel, 2005; Holliday et al., 2012; Bouton et al., 1999). However, changes in boundary conditions (temperature, initial pCO_2 and carbon isotope values) based on endmember values produce only small $\delta^{13}C$ and ^{14}C shifts that are < 5% of the values reported here, suggesting uncertainties in boundary conditions do not influence interpretations. Other model limitations involve model results that do not reflect changes between OM or soil-respired CO_2 carbon isotope values (Fig. 4), where the model requires us to specify initial only soil CO_2 carbon isotope values as model inputs. The drip water DIC $\delta^{13}C$ model also does not take into account processes occurring after dissolution (e.g. kinetic processes inside the cave); which could explain the remaining ~2‰ $\delta^{13}C$ shift.

4.7 Other Controls on McN-1 $\delta^{13}C$

Our DIC carbon isotope model does not reproduce the full magnitude of the shift in calcite $\delta^{13}C$ at the YD-Holocene transition, which suggests that variations in the McN-1 $\delta^{13}C$ record are largely a result from controls beyond carbonate dissolution. We assess other potential processes that controlled McN-1 $\delta^{13}C$ variability, including; kinetic fractionation, changes in vegetation type (C_3 vs C_4), and changes in epikarst drip water pH.

McN-1 $\delta^{13}C$ and $\delta^{18}O$ values are moderately correlated (r^2=0.48, n=249), which may support kinetic fractionation during calcite precipitation. To evaluate further whether or not kinetic fractionation can account for McN-1 $\delta^{13}C$ variability, we compared $\delta^{13}C$

values sampled within the same growth interval, for three different stratigraphic levels (see Section 2.2). We find that laterally offset $\delta^{13}C$ values from the same growth horizon are highly reproducible [standard deviations of overlapping paths mean values are ±0.08‰ (1σ)]. suggesting that kinetic fractionation is minimal. Because of the close horizontal spacing of the sampling tracks (Table 6), it is possible that kinetic fractionation is not fully assessed by our parallel transect measurements. Sampling transects located further from the growth axis may be required to better assess the influence of kinetic fractionation on McN-1 $\delta^{13}C$ values.

Organic matter from deeply rooted trees are suggested to be the primary source for speleothem carbon in central Texas (Breecker, et al., 2012; and Meyer et al., 2014), where carbon slow turnover times for deep OM are slow (centennial-millennial). Therefore, any changes in vegetation type (C_3 vs C_4) would be preserved in the speleothem $\delta^{13}C$ record over longer time scales than what is observed in the YD-Holocene transition $\delta^{13}C$ shift. Also, the C_3 dominated trees that supply OM carbon to regional caves could result in a strong C_3 bias on speleothem $\delta^{13}C$, further suggesting minimal $\delta^{13}C$ contribution from changes in C_3 vs C_4 vegetation. Changes in atmospheric $\delta^{13}C$ values over the last 25,000 years also cannot explain McN-1 $\delta^{13}C$ variability, as carbon isotope values have been shown to vary between -6.2 to -6.8‰, which would only result in changes to speleothem $\delta^{13}C$ of < 1‰ (Schmidt et al., 2012).

Tests of alternative mechanisms fail to reasonably account for the full magnitude of the shift in $\delta^{13}C$ at the YD-Holocene transition; therefore, we propose that changes in solution pH associated with epikarst pCO_2 variations, before calcite precipitation, could

account for the remaining ~-2‰ $\delta^{13}C$ shift. Low pH epikarst drip waters contain more isotopically negative H_2CO_3 (relative to HCO_3^- and CO_3^{2-}) compared to higher pH drip waters. Degassing in the cave should increase the pH of the drip water during calcite precipitation, which result in dissociation of H_2CO_3 and thus decrease in the $\delta^{13}C$ values of HCO_3^- and CO_3^{2-}, and ultimately result in speleothem calcite with lower $\delta^{13}C$. If the epikarst transitioned to more open system conditions across the YD-Holocene boundary, increased ventilation could have increased availability of O_2, resulting in increased autotrophic/heterotrophic respiration rates above the cave (Kuzyakov and Larinova, 2005). An increase in respiration rates would increase epikarst pCO_2 and decrease drip water pH and calcite $\delta^{13}C$.

4.8 Changes in Regional Climate during the YD-Holocene Transition

The late Pleistocene involved several abrupt deglacial warming and cooling events, concluding with the rapid transition to warmer and more stable Holocene climate at 11,700 yrs BP. Recent paleoclimate research from subtropical and tropical latitudes demonstrate antiphasing relationships in the late Pleistocene, where wetter conditions in one region correspond with drier conditions in another (Vakulenko et al., 2006; Cruz et al., 2009; Kowler, 2015). Initiation of the YD has been linked through proxy records to a change from meltwater outflow via the Mississippi River southward to the Gulf of Mexico, to the meltwater outflow via St. Lawrence River system northeastward to the North Atlantic Ocean (Lehman and Keigwin, 1992; Broecker et al., 2006; Murton et al., 2010; Not and Hillaire-Marcel et al., 2012). An influx of freshwater to the North Atlantic of this magnitude could have reduced North Atlantic Deep Water (NADW) formation (McManus

et al., 2004). Globally, this weakening in NADW formation would reduce cross-equatorial flow of warm surface waters from the tropics, resulting in widespread high-latitude cooling in the northern hemisphere, southward shift of the Intertropical Convergence Zone (ITCZ), and Antarctic warming from a build-up of heat in the South Atlantic Ocean (Stocker et al., 1992; Alley and Clark, 1999).

Atmospheric circulation models and ocean circulation proxy records suggest that the termination of the YD (11,700 yrs BP) coincided with reinvigoration of NADW formation (Hughen et al., 1996; Fawcett et al., 1997; Lassen et al., 2002; Vellinga and Wood, 2002; Bakke et al., 2009) and a northward shift in the ITCZ (Haug, et al., 2001; Fleitmann et al., 2006; Deplazes et al., 2013; Schneider et al., 2014). The ITCZ migrates because of differential hemisphere warming, and can occur seasonally or over longer timescales (centennial or millennial) (Schneider et al., 2014). ITCZ migration affects global rainfall distribution, resulting in changes in monsoon intensity and jet stream patterns (Schneider et al., 2014). Paleoclimate modeling suggests that an expanded Laurentide ice sheet during glacial periods could deflect the jet stream southward, causing increased rainfall in the Southwestern U.S. (Kutzbach and Guetter, 1986). Reflectance of biogenic and terrigenous deposits from Caricao basin sediments as well as multiple land-based records from the circum-Caribbean region suggest the ITCZ responded to millennial variations in high northern latitude temperature during the deglacial (Peterson and Haug, 2006; Deplazes et al., 2013). Each time high northern latitudes cooled, a southward ITCZ migration is observed in the Caricao basin records, including during the YD. A Borneo stalagmite record shows coeval reductions in rainfall with millennial high-latitude cooling events during the deglacial, suggesting the southern tropics experienced increased rainfall

during southward ITCZ migrations (Partin, 2007). In North America, a more southerly ITCZ would shift the Pacific westerly storm track south and result in higher amounts of Pacific-derived rainfall over the southwestern U.S. (Allen and Anderson, 1993; McGabe, 1996). Interpretations of Arizona and New Mexico speleothem records attribute increased Pacific-derived rainfall during late Pleistocene cooling events (including the YD) to southward shifts in the westerly storm track (Asmerom et al., 2010; Wagner et al., 2010). Although modern Texas rainfall is predominantly sourced from the Gulf of Mexico (Seager et al., 2007), an enhanced contribution of Pacific-derived rainfall does occur during the winter (Wong et al., 2015). Therefore, shifts in the ITCZ could have modified regional winter rainfall as a result of changes in the Pacific westerly storm track during the YD.

Wong et al. (2015) document extensive variability among multiple Texas moisture and temperature proxy records during the Holocene, with focus on soil $\delta^{13}C$, fluvial and eolian deposits, speleothems and magnetic susceptibility records. Although some variability can be attributed to limited controls on age, landscape evolution, and proxy interpretation (Wong et al., 2015), these proxy records overall support a general warming/drying trend from the YD through the Holocene. Several early Holocene records indicate a drying trend from the onset of the Holocene to the late Holocene (5,000-3,000 yrs BP), after which wetter conditions persist from 3,000-1,000 yrs BP, and then return to drier conditions for the remaining Holocene. The abruptness and timing of the YD-Holocene transition drying trend does vary among proxy records. Contrary to the abrupt moisture change identified in the McN-1 record, an analysis of alluvial deposit carbon isotopes at Fort Hood, Texas indicates a gradual shift to warmer and drier conditions at the YD/Holocene boundary (Nordt et al., 1994). Faunal assemblages and magnetic

susceptibility records from Hall's Cave, Texas do show increased aridity through the Holocene (Toomey et al., 1993; Ellwood and Gose, 2006); however, these records suggest the drying trend may have begun before the YD. The Hall's Cave proxy records show centennial resolution, whereas the McN-1 record is an order of magnitude higher and shows decadal resolution.

Similar to our McN-1 moisture interpretations, multiple southwestern U.S. speleothem records show a general moisture increase over the southwestern U.S. during the YD (Table 8), followed by drying in the early Holocene (Polyak et al., 2004). This is consistent with SOM $\delta^{13}C$ values from central Texas which indicate decreased C_4 productivity (possible resulting from increased moisture) during the YD, and correspond with glacial meltwater influx to the Gulf of Mexico at the onset of the YD (Holliday et al., 2011). Changes in strontium isotope variations from Edwards Plateau cave-fill deposits, as well as eolian deposits and soil carbon isotope data from the Texas Southern High Plains also suggest an increase in aridity and extensive soil erosion spanning from the beginning of the Holocene (Cooke et al., 2003; Holliday, 2001). Several central Texas caves contain sediments from these eroded soils (Toomey et al., 1993; Cooke et al., 2003), suggesting that the detrital material present in McN-1 could also be derived from this same soil erosion event.

Our interpretation of the McN-1 speleothem $\delta^{13}C$-DCP record agrees with multiple other Texas paleoclimate records, which indicate a climate transition from wetter conditions during the YD to drier conditions through the Holocene. McN-1 growth rates and petrographic fabrics also support wetter conditions during the YD, followed with an

abrupt decrease in moisture (reduced growth rates) in the early Holocene (Fig. 6). If the McN-1 DCP record mainly proxies changes in the carbonate dissolution regime, as detailed earlier, then abrupt vadose zone drying would have occurred in less than 230 years, and as little as 50 years given our geochronological constraints. The relatively short time span in which this drying occurred is not observed in most existing Texas paleoclimate records. This moisture transition in central Texas coincides with the end of the YD, when Greenland temperatures increased 7-9° C in a span of decades (Rasmussen et al., 2006). These similarities are consistent with a contemporaneous climate response between the Arctic and mid-latitudes related to changes in AMOC and attendant shifts in the ITCZ and related jet stream patterns (Haug, et al., 2001; Fleitmann et al., 2006; Deplazes et al., 2013; Schneider et al., 2014). This suggests that Texas climate is responsive to hemispheric-wide rapid warming events via changes in northern hemisphere teleconnections and moisture transport.

CHAPTER 5: CONCLUSIONS

We integrated stable isotopes, ^{14}C and petrographic analyses from a central Texas speleothem to understand how moisture conditions changed during the late Pleistocene-early Holocene transition. Changes from fast to slow growth rates of the McN-1 stalagmite suggest an abrupt transition to drier conditions at the onset of the Holocene, with dry conditions (slow growth) persisting through the early Holocene (11,700 to 8,900 yrs BP). Petrographic inspection of speleothem growth fabrics (from columnar open fabric indicative of fast drips during the Younger (YD), to columnar compact fabric during the onset of the Holocene) supports the growth rate-moisture proxy interpretation.

We use coupled time series of $\delta^{13}C$ and DCP to constrain likely epikarst moisture conditions and delineate controls on speleothem $\delta^{13}C$ and DCP. A rapid 3‰ shift to lower $\delta^{13}C$ values occurs after the end of the YD within 230 years, concurrent with a 7.5% decrease in dead carbon proportion (DCP). McN-1 DCP and $\delta^{13}C$ values show parallel declines between 12,200-10,500 yrs BP, suggesting that changes in the nature of carbonate dissolution processes in the vadose zone were a control on speleothem $\delta^{13}C$ and DCP. The higher DCP and $\delta^{13}C$ values during the YD support a greater carbon contribution to DIC from host rock and higher vadose zone moisture contents, whereas the decrease in these values at the end of the YD indicates abrupt vadose zone drying. This produced a shift from a relatively closed to an open epikarst system during the YD-Holocene transition. To quantify how changes in the epikarst dissolution regime could have affected speleothem $\delta^{13}C$, a calcite dissolution model (Fohlmeister et al., 2011) was used to characterize epikarst drip water $\delta^{13}C$ compositions associated with differing open/closed system

conditions in the vadose zone. Calcite dissolution model results indicate that changes in the carbonate dissolution regime can only explain 25% of the ~3‰ negative shift in speleothem $\delta^{13}C$ values, with a transition from a partially open to fully open dissolution system. Kinetic effects also cannot explain the negative $\delta^{13}C$ shift, as Hendy $\delta^{13}C$ offset tests for three separate growth horizons show high reproducibility in $\delta^{13}C$. To best explain the remainder of the ~3‰ $\delta^{13c}C$ shift, we propose that increases in respiration rates acted to decrease drip water pH, thereby resulting in lower calcite $\delta^{13}C$.

The coupled carbon isotope and growth rate record for McN-1 was used to assess regional moisture conditions during the YD. Both the abrupt nature and timing of the $\delta^{13}C$ and DCP shift suggest the epikarst experienced rapid drying in the transition from the YD. Our interpretation of a transition to drier Holocene conditions generally agrees with several Texas paleoclimate records (Toomey et al., 1993; Holliday, 2000; Polyak et al., 2004; Ellwood and Gose, 2007; Wong et al., 2015). The relatively short time span of this drying event (as little as 50 years given age constraints) is consistent with Greenland temperature increases over the same time interval (Rasmussen et al., 2006) and suggests a link with high latitude climate during the end of the YD.

FIGURES AND TABLES

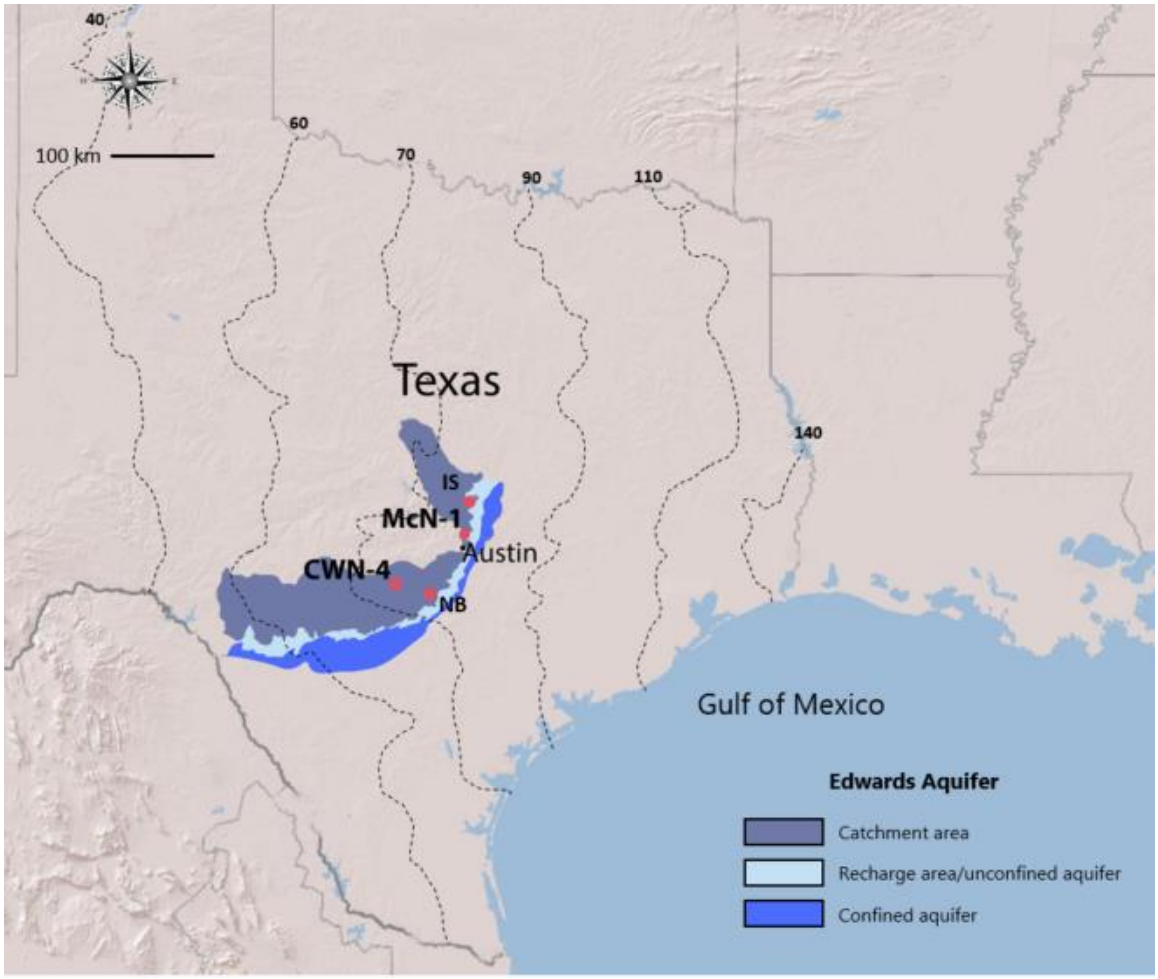

Figure 1: Site map showing the location of central Texas speleothem records (McN-1, CWN-4). Two additional central Texas caves [Natural Bridge Caverns (NB) and Inner Space Cavern (IS)] are shown, where active monitoring of cave drip water and ventilation systems has been conducted for the past two decades (Musgrove and Banner, 2004; Banner et al., 2007; Feng et al., 2012; Cowan et al., 2013). MCN-1, CWN-4, IS and NB are formed within the Cretaceous limestone of the Edwards group. Hydrologic zones of the Edwards aquifer are shown in blue. The confining unit of the Edwards aquifer is the Del Rio Clay, and is eroded over by the catchment area and recharge area. Annual rainfall contours (cm/year) are shown as black dashed lines (TWDB, 2005). Most rainfall for central Texas originates from the Gulf of Mexico, with average rainfall totaling 83 cm/year.

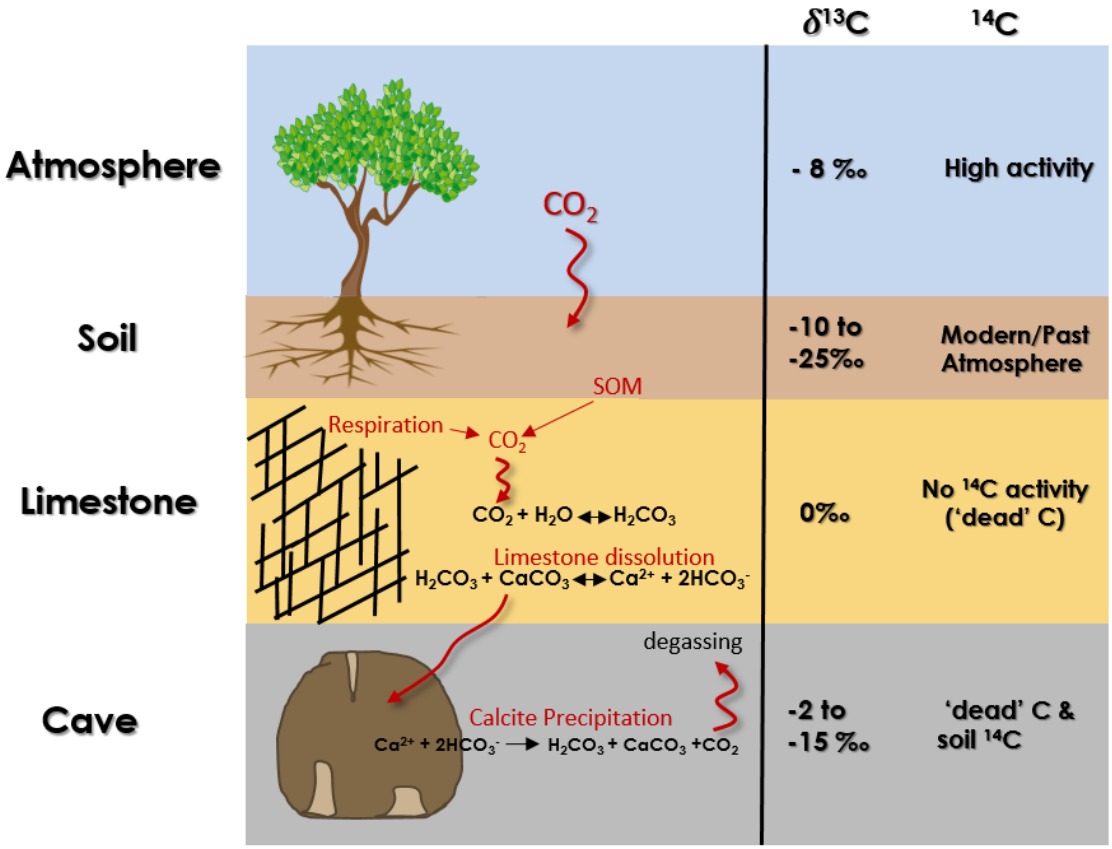

Figure 2: Diagram of calcite dissolution and precipitation processes extending from the atmosphere to the cave environment. Shown are typical $\delta^{13}C$ values and relative ^{14}C descriptions of the respective carbon reservoirs. Meteoric water infiltrates into the soil and bedrock and interacts with CO_2, forming H_2CO_3. H_2CO_3 migrates down into the limestone bedrock and dissolves it under variable open/closed system conditions. Under a closed system, the soil CO_2 gas is isolated from the dissolution process via water filled pore spaces, and the evolved DIC has carbon isotope signatures similar to carbonate bedrock (Fig. 16). Upon entering lower pCO_2 conditions of the cave, drip water degasses, resulting in speleothem calcite precipitation.

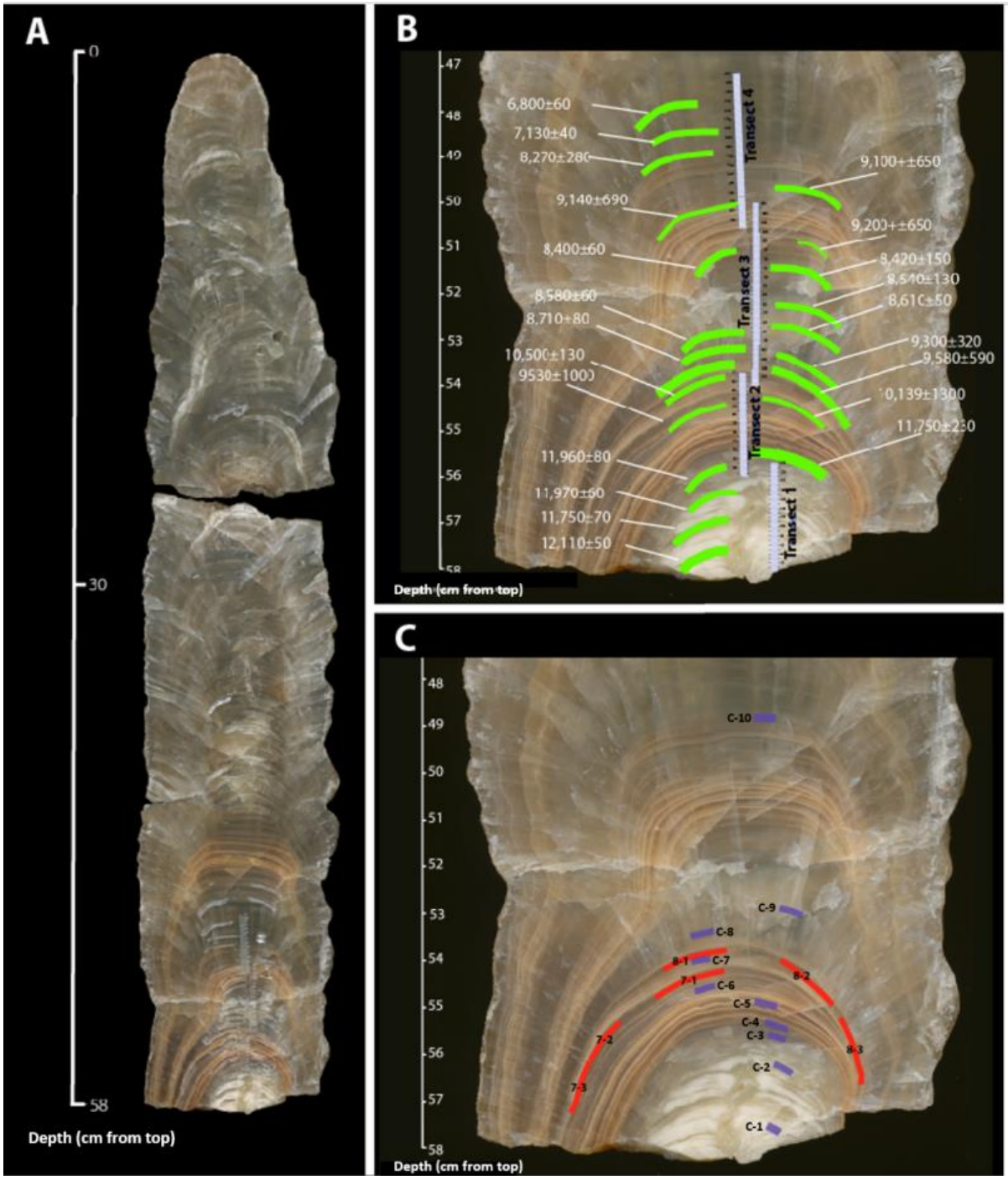

Figure 3: Sample McN-1 polished slab face. Distances (cm) are relative to the top of the stalagmite. Panel A shows drilled sample locations. Panel B shows U-series ages (green), and stable isotope transects (white). Stable isotopes were drilled at 100 um step increments along the central growth axis, with four offset, but partially overlapping, drill paths. Stratigraphically equivalent samples at three locations between the offset transects were used to understand kinetic effects. Panel C shows isochron (red) and ^{14}C (purple) sample locations.

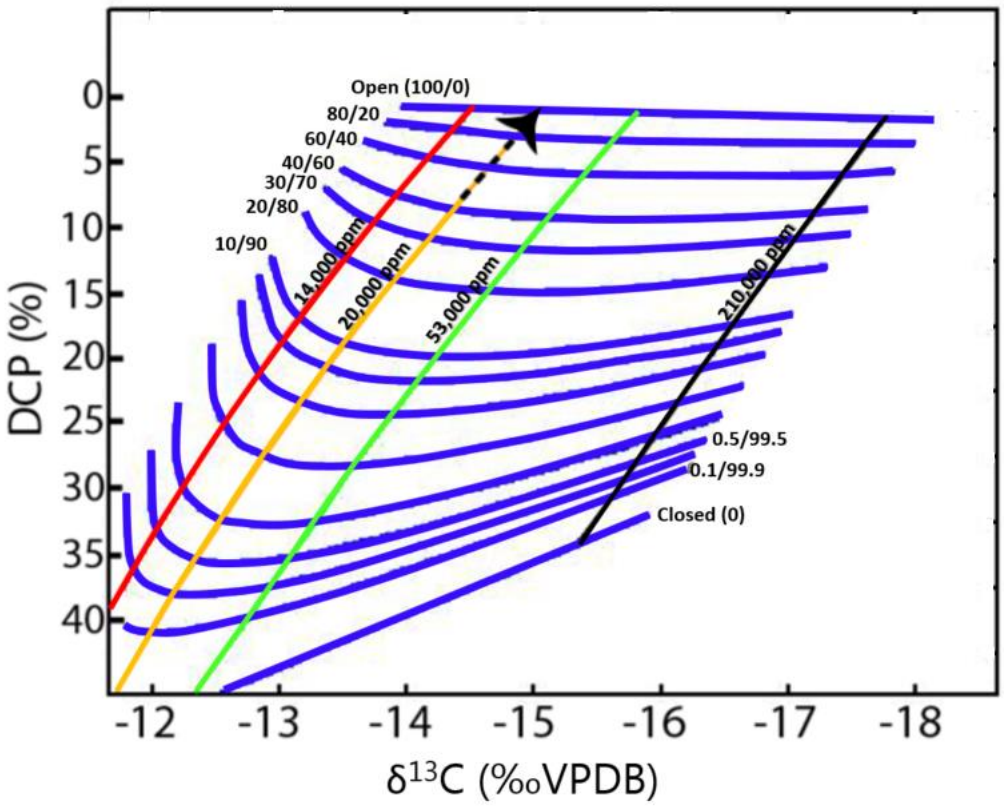

Figure 4: Simulation of the evolution of drip water DCP and $\delta^{13}C$ values along paths determined by various ratios of dissolution under open versus closed system conditions. The model, adapted from Fohlmeister et al. (2011), characterizes changes in both DCP and $\delta^{13}C$ as a function of differing open/closed system ratios (blue lines). Iso-pCO_2 lines, shown by the red, orange, green and black lines, show variations at fixed pCO_2 values, where: red = 14,000 ppm, orange = 20,000 ppm, green = 53,000 ppm, and black = 210,000 ppm. Based on soil pCO_2 data over central Texas caves, we selected 20,000 ppm, which shows a change in DCP from 7.5-0% as corresponding to a change in $\delta^{13}C$ of 0.68‰. This explains 25% of the total -2.8‰ change in $\delta^{13}C$ from YDI to HO. Therefore, the majority of the $\delta^{13}C$ shift at the YD-Holocene transition cannot be explained by this model and are a result of other processes. This drip water evolution path is designated by the black arrow. A DCP shift of this magnitude corresponds to a shift in the open/closed system ratio of 40/60 to 100/0. The $\delta^{13}C$ values shown here are different than observed values in McN-1 $\delta^{13}C$ (values span -9 to -4%) for a number of reasons. 1.) modeled values are for water DIC, not calcite, 2.) fractionation effects during calcite precipitation are not considered in this model, which would result in higher $\delta^{13}C$, and 3.) the initial $\delta^{13}C$ value of the CO_2 is not known. However, this discrepancy is not of primary importance as we are interested in how changes in the carbonate dissolution regime affect the magnitude of the $\delta^{13}C$ values, not the absolute values. Initial model parameter values are: temperature = 15°C, CO_2 $\delta^{13}C$ = -22‰, pCO_2 = 20,000 ppm, and CO_2 ^{14}C = 100 pMC.

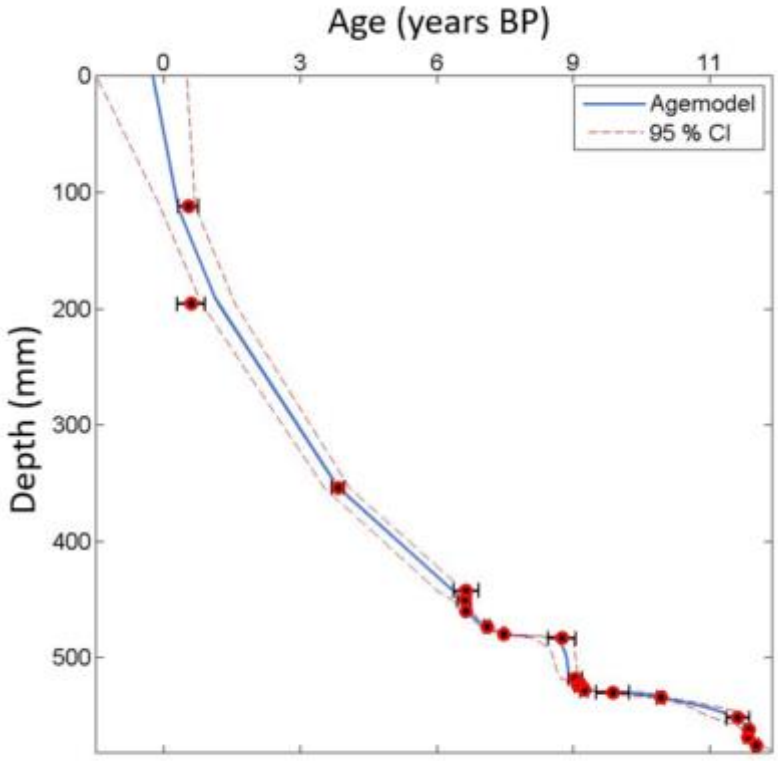

Figure 5: McN-1 age model calculated using Monte-Carlo statistical software COPRA (Breitenbach et al., 2012). U-series ages (red symbols) are shown with associated uncertainties (2σ) based on analytical uncertainty on the calculated initial $^{230}Th/^{232}Th$ value (14.7 ± 3.8 ppm). The blue line shows the best-fit solution for the U-Th chronology. Dashed red lines show 95% confidence interval for age estimates.

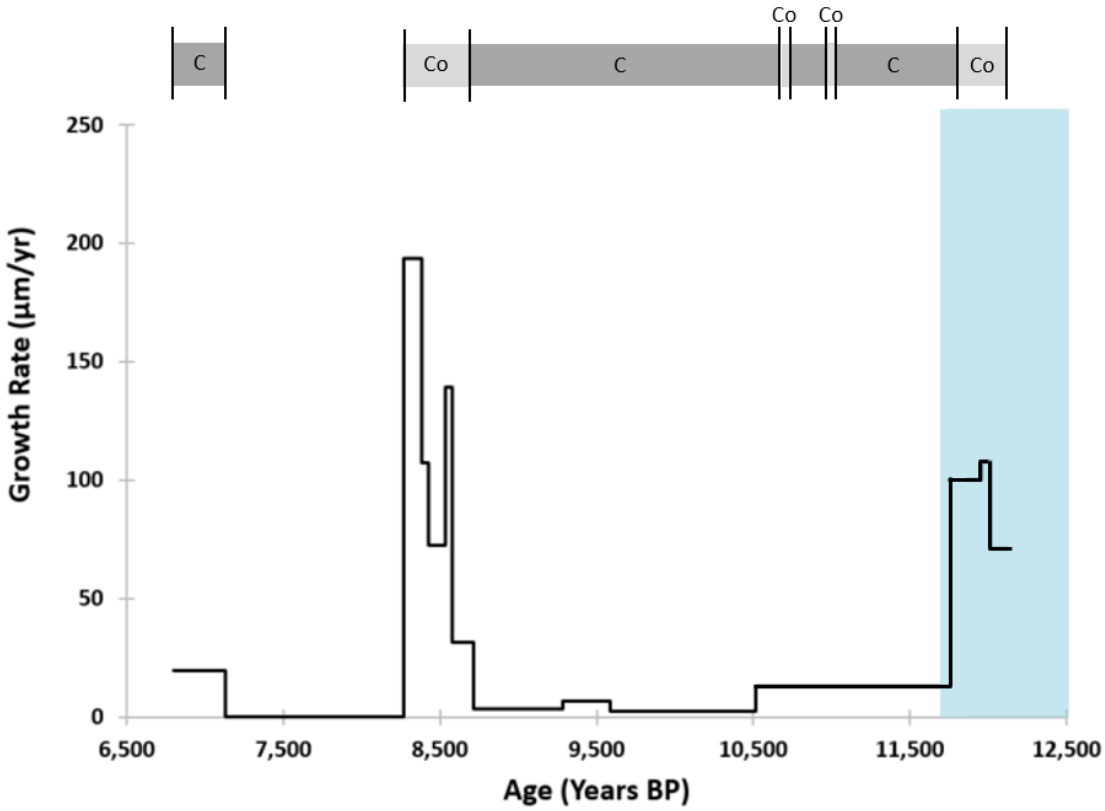

Figure 6: McN-1 growth rates calculated from the measured distances between U-series ages. The YD interval is represented by the blue shaded box. Growth rates show relative fast growth during the YD, with an abrupt decrease in growth at the YD-Holocene boundary. Temporal changes in fabric classifications (see Figs. 10-12) are shown at the top with columnar open (Co) fabric comprising most of the YD and occurs contemporaneously with faster growth rates. Columnar compact (C) fabric begins at the end of the YD and extends through the early Holocene during slower growth.

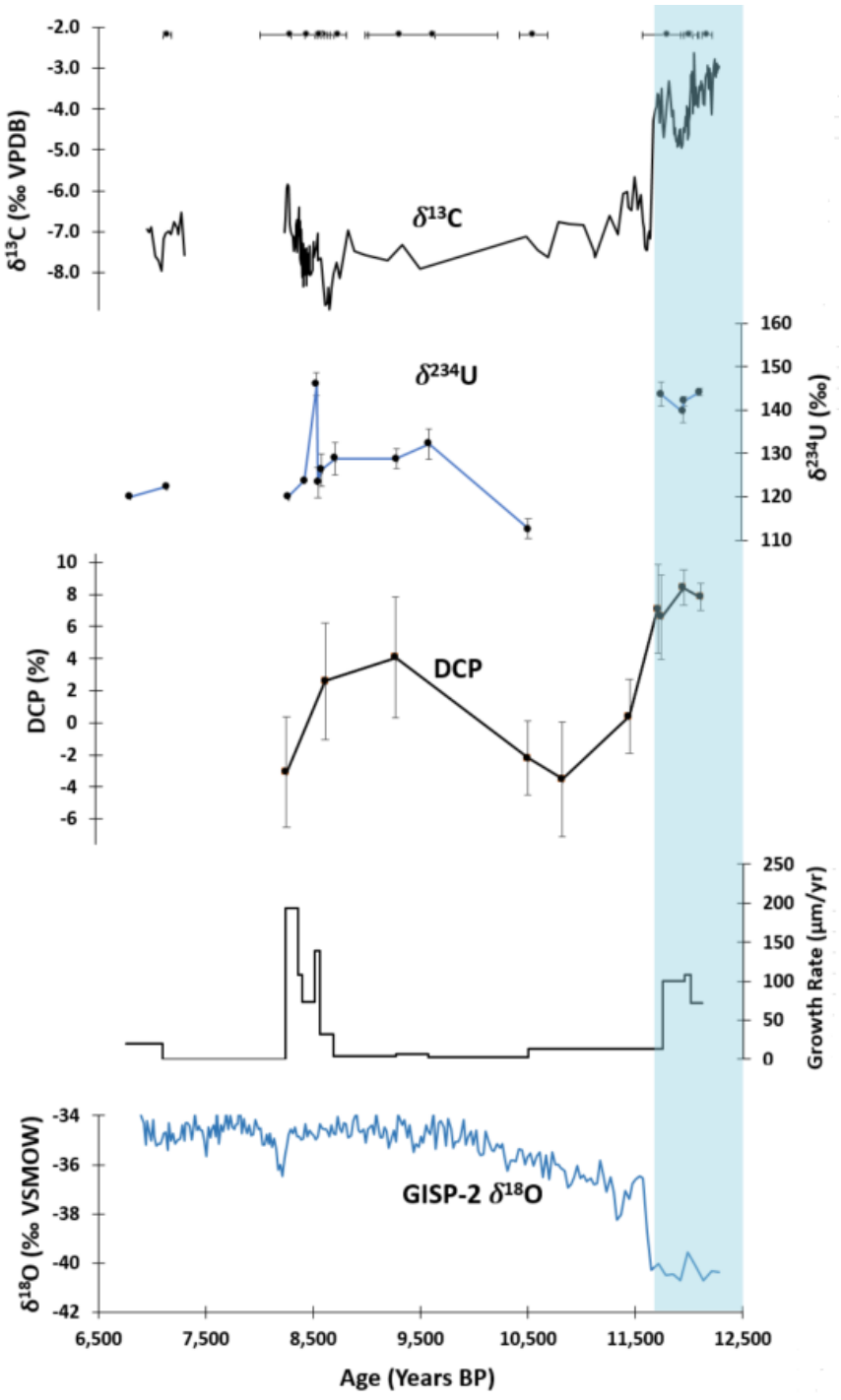

Figure 7: $\delta^{13}C$, DCP, $\delta^{234}U$, and growth rate time series for McN-1 spanning the YD (blue field) to early Holocene. Significant decreases in $\delta^{13}C$, DCP, $\delta^{234}U$ and growth rates occur at the end of the YD, with a negative $\delta^{13}C$ shift of -2.8‰ and a DCP decline of 7.5%. The YD interval is shaded in blue. $\delta^{18}O$ values from the GISP-2 ice core record show the timing of the termination of the YD (abrupt increase in $\delta^{18}O$ of ~4‰ at ~11,700 yrs BP) (Stuiver et al., 1995; Grootes et al, 1997).

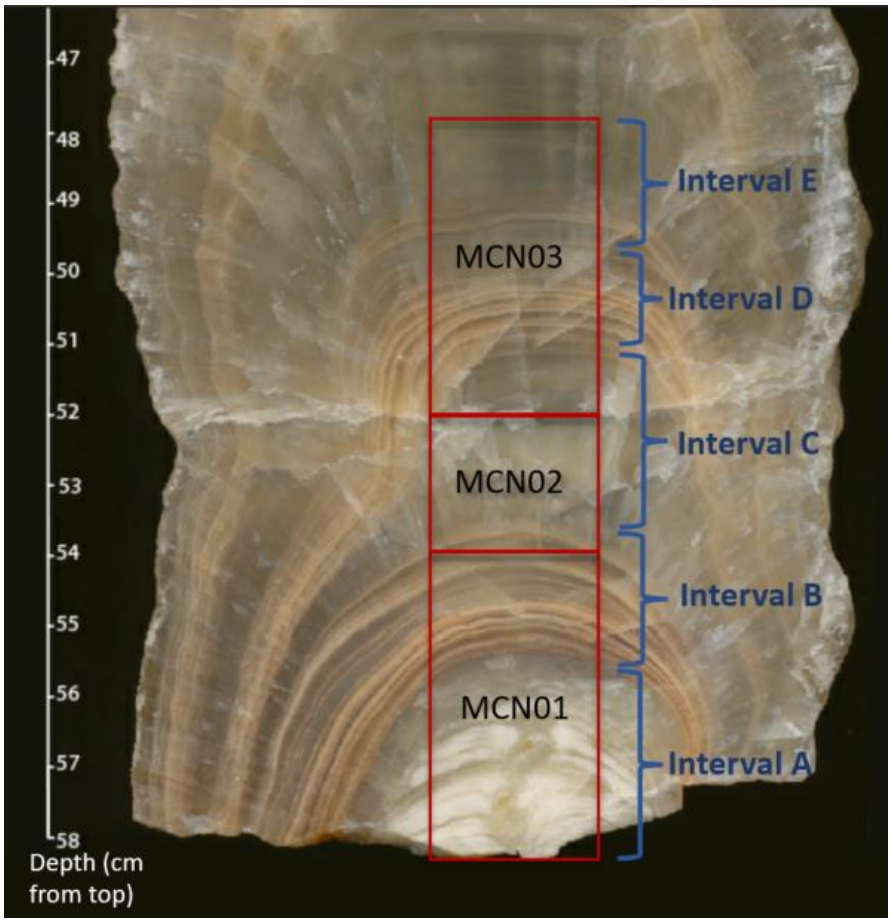

Figure 8: Shown are McN-1 thin section locations (MCN01, MCN02, MCN03) and microstratigraphy intervals. Intervals A, B, C, D, and E are defined based on changes in lamina type. Interval A extends from 58 to 55.5 cm from top and spans 12,200 to 11,600 yrs BP. Columnar open (Co) fabric dominates the majority of Interval A. This interval contains porous, opaque lamina along the basal portion and transition translucent dense lamina near the top. Interval B shows a sharp transition to brown-tan lamina occurring at 11,600 yrs BP, corresponding the onset of the Holocene. Interval C shows a transition into translucent dense lamina extending from ~54 to 51.5 cm from top, and spans 9,600 to 8,600 yrs BP. Columnar compact (C) fabric dominates the majority of Intervals B and C. Interval D contains brown-tan porous lamina that are flatter than lamina in Interval B, and extends from 51.5 to 49 cm from top. Columnar open fabric is the dominant fabric type in Interval D. Interval E extends from 49 to 47 cm from top and contains translucent dense lamina consisting of columnar open fabric.

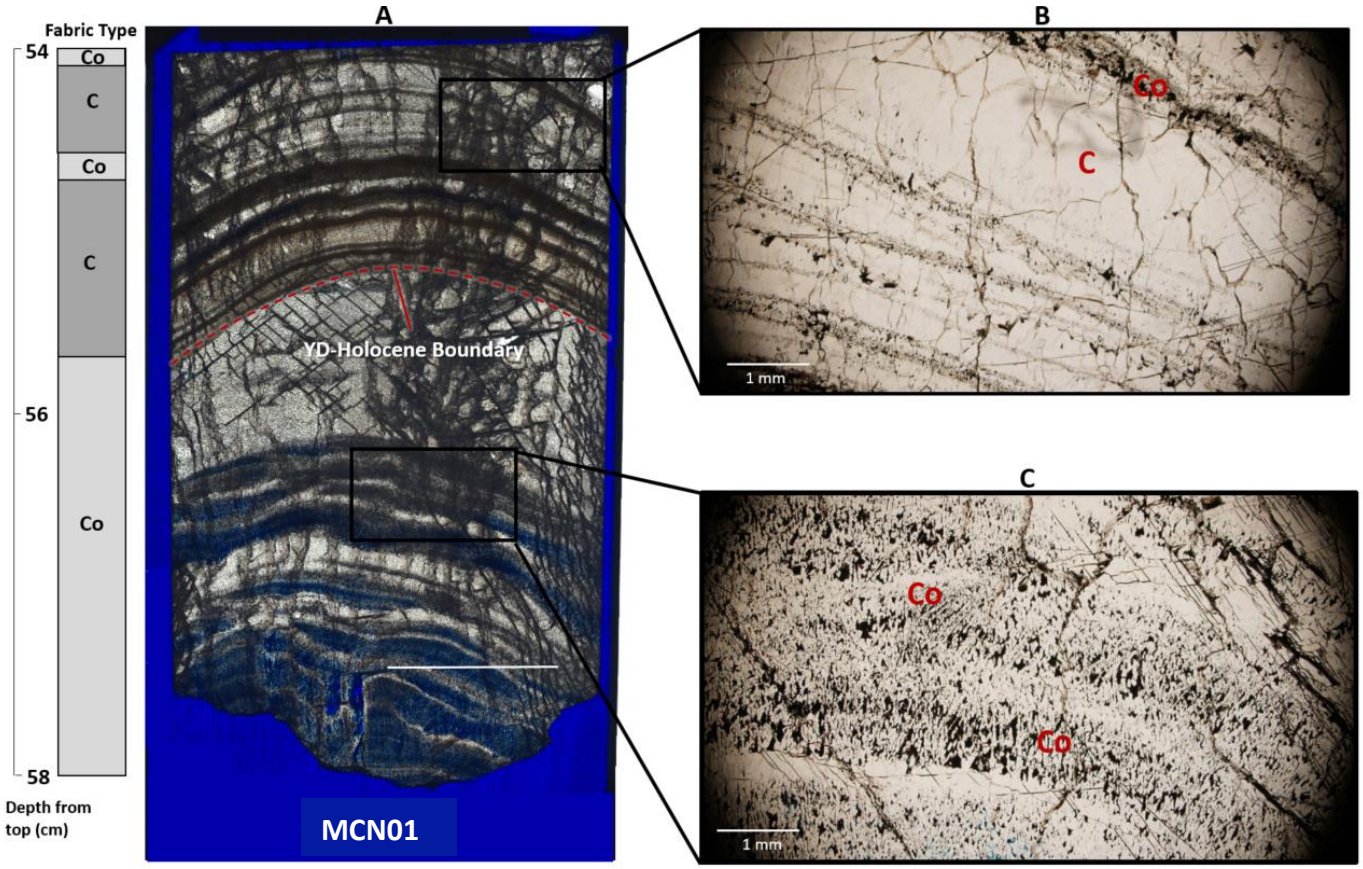

Figure 9: Thin section McN03 of the bottom-most portion of McN-1, showing the YD-Holocene boundary (Panel A). McN-1 is comprised of columnar calcite with both columnar open (Co) and columnar compact (C) fabric (shown in red letters). Fabric classifications are shown as defined by Frisia et al., (2015), where columnar open fabric contains high porosity and incomplete coalesced calcite. Columnar compact fabric show no porosity. Columnar open fabric is the dominant fabric type spanning the bottom most portion of McN-1, extending 58-55.5 cm from the top (Interval A; Fig. 8). Columnar compact fabric is the dominant fabric type from 55.5-54 cm, with thin intervals of Co fabric dominating two of the darker laminae. The columnar compact fabrics correspond with the onset of the early Holocene, lower DCP and $\delta^{13}C$ values, and slower growth rates.

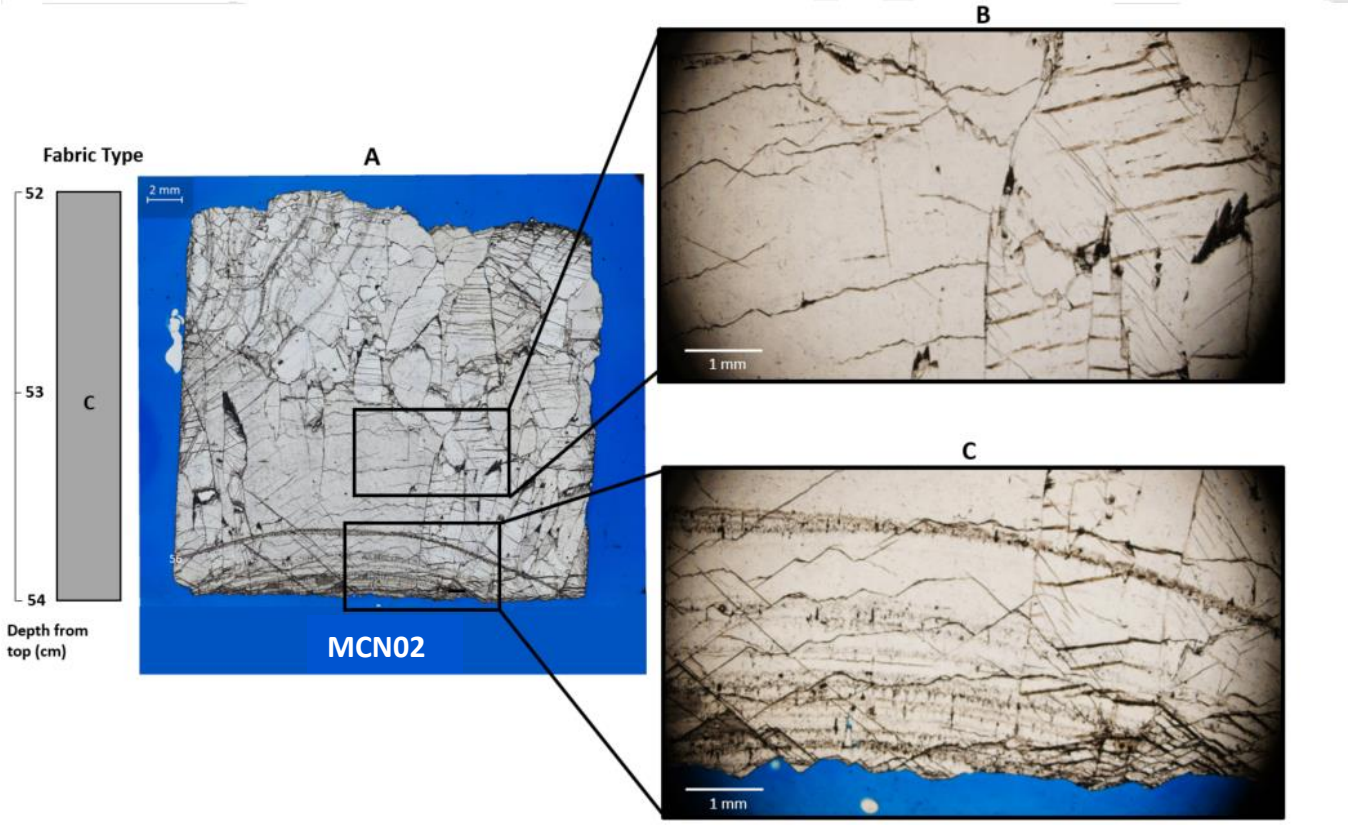

Figure 10: Thin section McN02. Fabric classifications are shown as defined by Frisia et al., (2015). Columnar compact fabric (C) dominates this portion of McN-1. Locations of thin sections are shown in Figure 9.

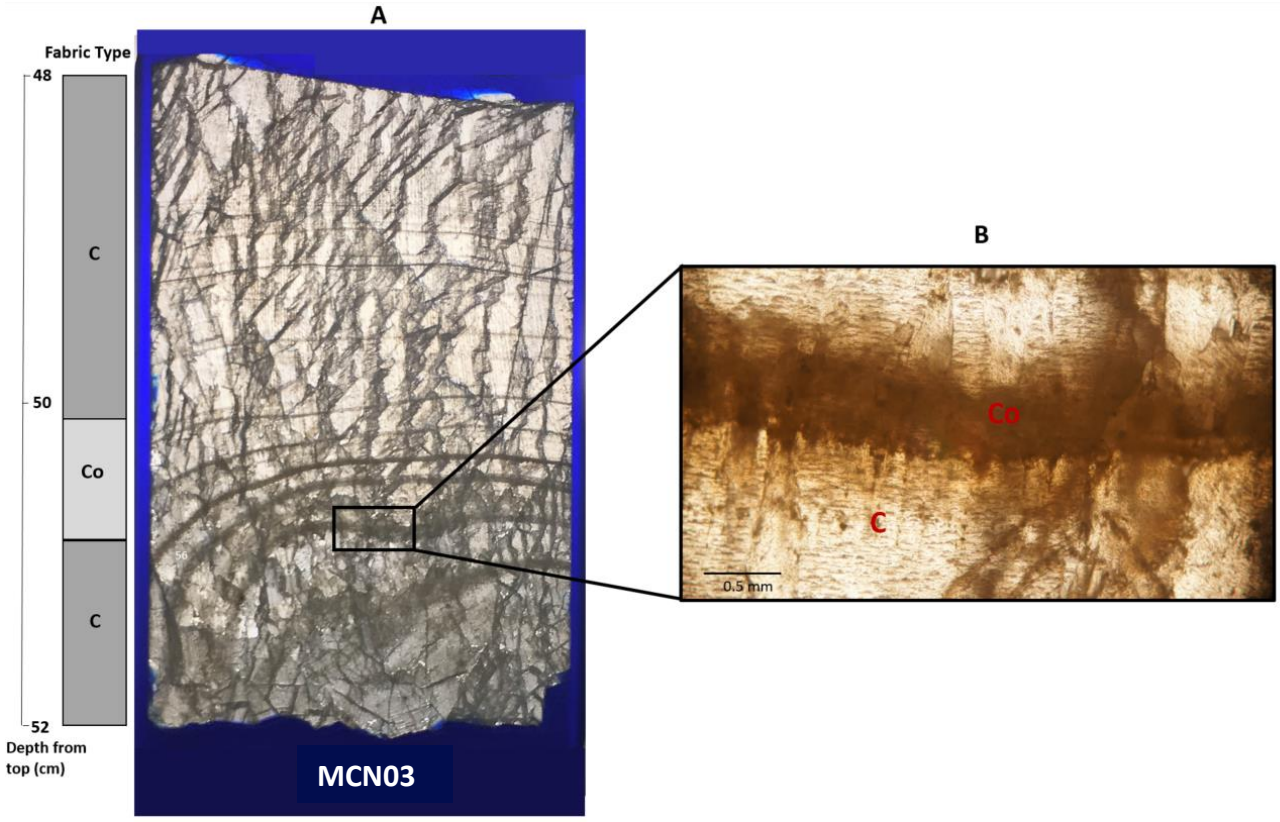

Figure 11: Thin section McN03. Fabric classifications are shown as defined by Frisia et al., (2015). Columnar compact (C) fabric comprises the majority of this portion of McN-1, with columnar open (Co) fabric observed between 51.5 to 50 cm from the top (Interval D, Fig. 8) and spans ~8,500 to 8,300 yrs BP. Co fabric is shown in Panel B, appearing cloudy and blurry due to light being refracted through porous calcite. This region of Co fabric is cotemporaneous with relatively fast growth rates (~130μm/yr) and marked by an increase in $\delta^{13}C$ values (from -8.5 to -6‰).

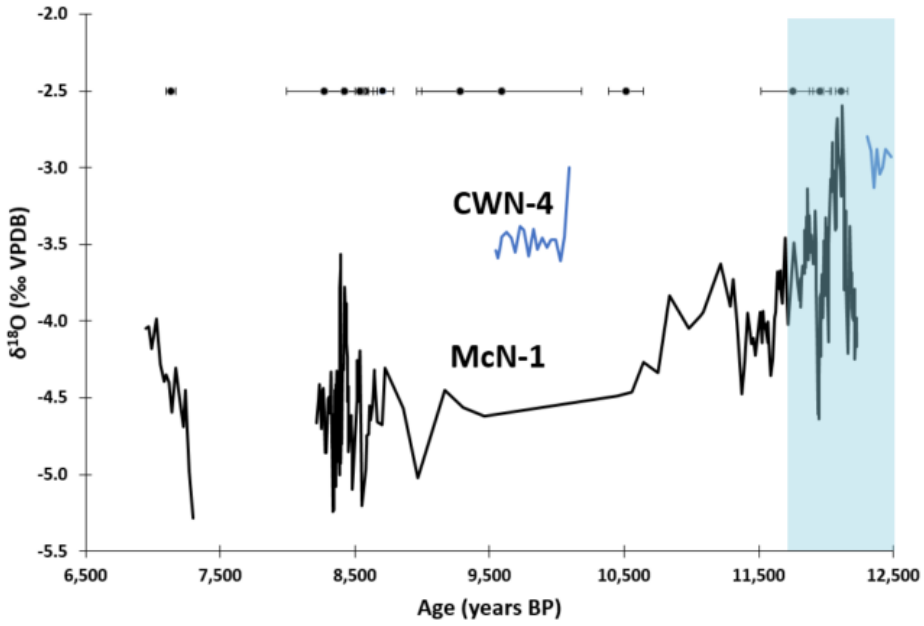

Figure 12: McN-1 and CWN-4 $\delta^{18}O$ time series. The YD interval is highlighted in blue. McN-1 $\delta^{18}O$ values are shown in black and CWN-4 $\delta^{18}O$ values are shown in blue. McN-1 $\delta^{18}O$ values are highly variable and range from -5‰ to -2.5‰, with a gradual trend to more negative values occurring through the YD and early Holocene.

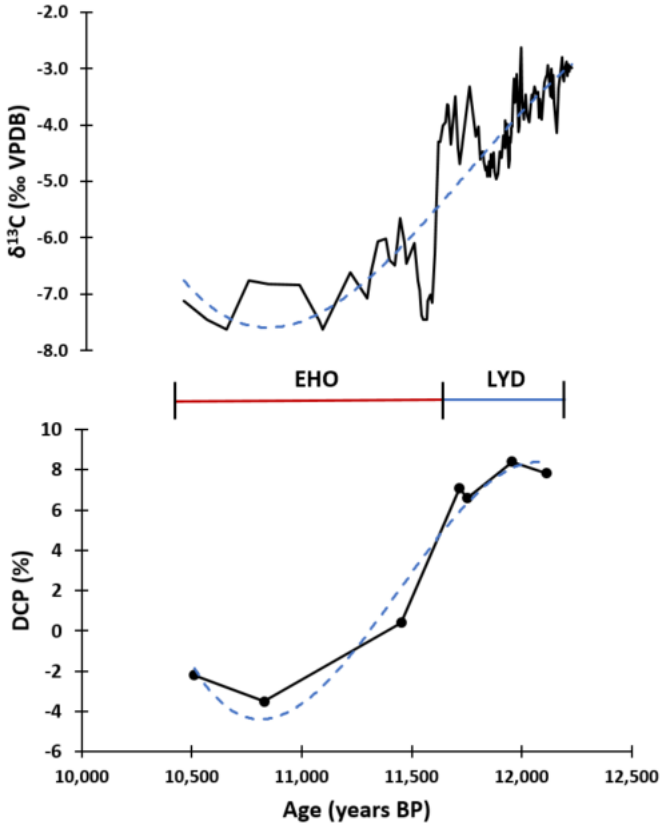

Figure 13: Prescribed intervals for comparison of mean moisture state using $\delta^{13}C$ and DCP, where LYD spans 12,200 – 11,603 yrs BP, and EHO spans 11,603 - 10,488 yrs BP. The dashed blue lines are third order polynomial fits in $\delta^{13}C$ and DCP spanning the YD-Holocene transition. Note the significant positive correlation between DCP and $\delta^{13}C$ (r^2=0.75, n=7) over this interval. LYD has mean $\delta^{13}C$ and DCP values of -3.8‰ and 7.5%, respectively. EHO has mean $\delta^{13}C$ and DCP values of are -6.6‰ and 0.0%, respectively.

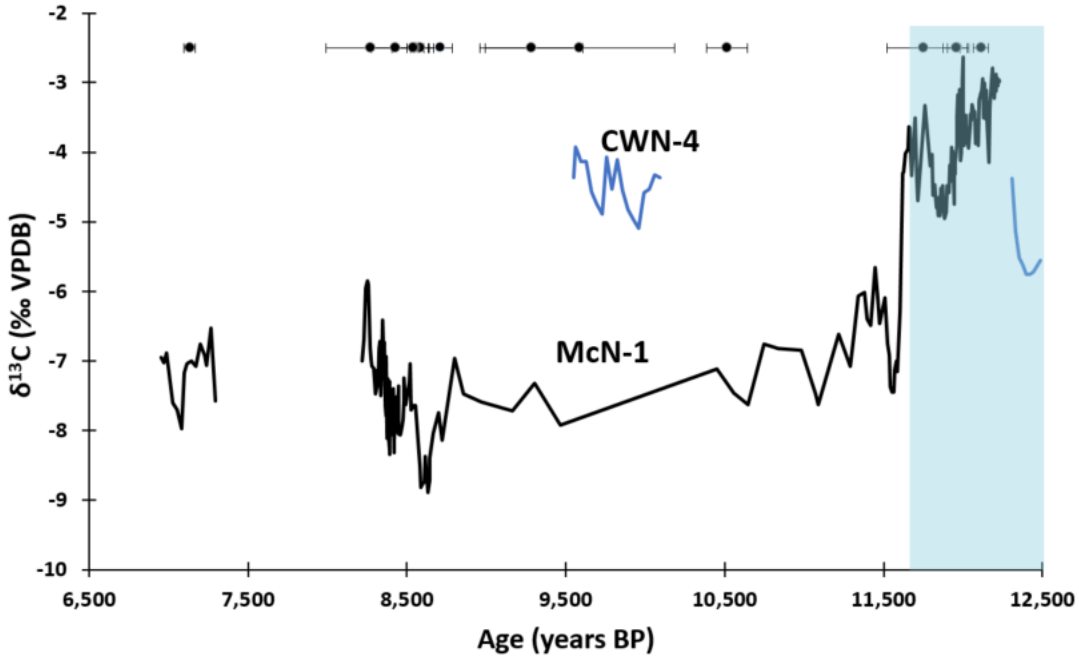

Figure 14: Comparison of CWN-4 (blue) and McN-1 (black) $\delta^{13}C$ time series.

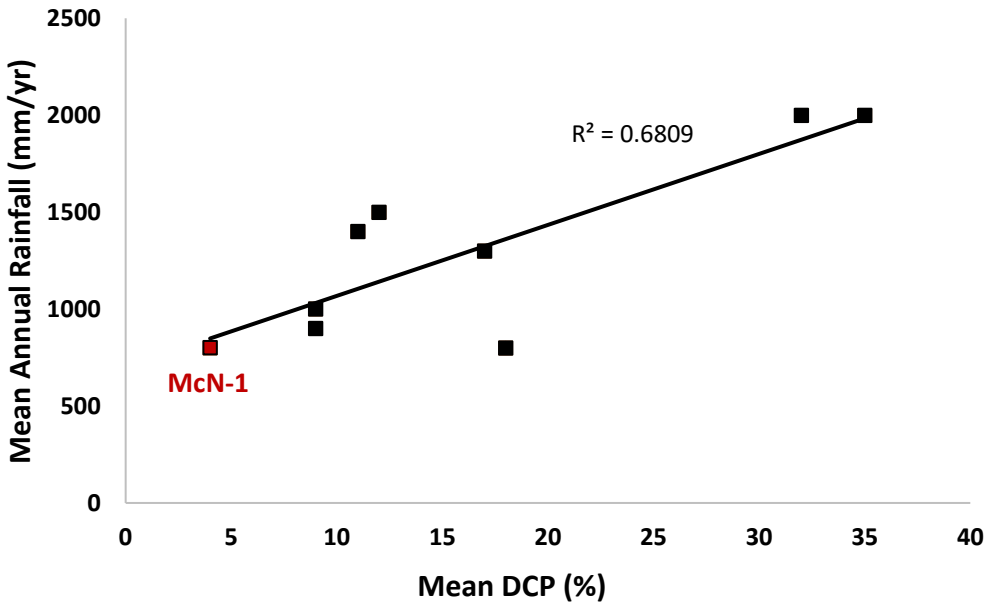

Figure 15: Correlation between DCP from modern speleothems and annual rainfall totals from a geographic range of regions (see Table 6 for speleothem locations). Higher DCP values are observed in regions with higher annual rainfall. A positive correlation between DCP and annual rainfall (r^2=0.68, n=8) is shown, suggesting rainfall can be a strong control on DCP. DCP and modern annual rainfall for McN-1 is shown in red.

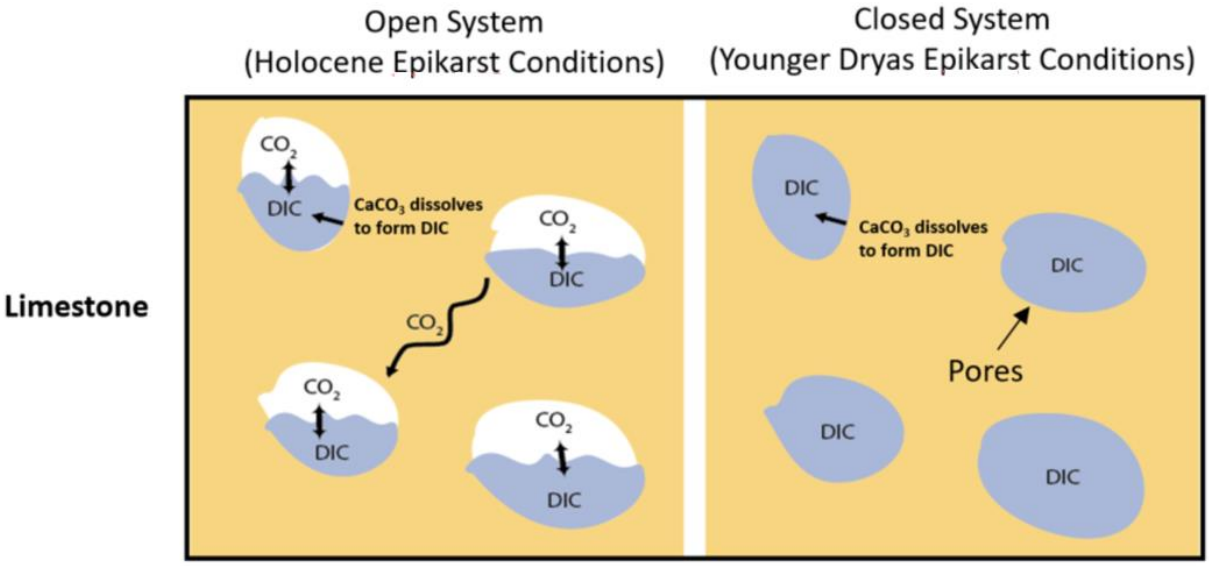

Figure 16: Schematic showing the differences between open/closed system conditions of the epikarst carbonate dissolution regime based on variable vadose zone moisture. Open system conditions have infinite gas/water ratio, which could be caused by 1.) relatively small water-filled pore space compared with gas-filled pore space, or 2.) enhanced gas phase exchange with the atmosphere by ventilation or diffusion. In this schematic, we are showing changes in the carbonate dissolution regime as a result of to changes in the amounts of pore water. Hypothetical pore spaces are shown in limestone filled with varying amounts of water (grey). The open/closed dissolution scenarios are shown in as categorizing the Younger Dryas and Holocene relative moisture conditions. Under open system conditions, DIC is in equilibrium with an unlimited supply of soil CO_2 gas. In this open system, both the ^{14}C activities and $\delta^{13}C$ of the DIC approach values similar to OM because the carbon isotopes derive from OM CO_2, corresponding to relatively lower DCP (~0%) and $\delta^{13}C$ values. In a closed system, dissolution of carbonate does not begin until the water is isolated from the OM-derived CO_2 gas and, therefore, equilibrium between and DIC and CO_2 gas is not maintained. In a perfectly closed system, soil-limestone pore spaces completely fill with water with no CO_2 gas present. Carbonate dissolution in natural systems varies between these two end-member scenarios.

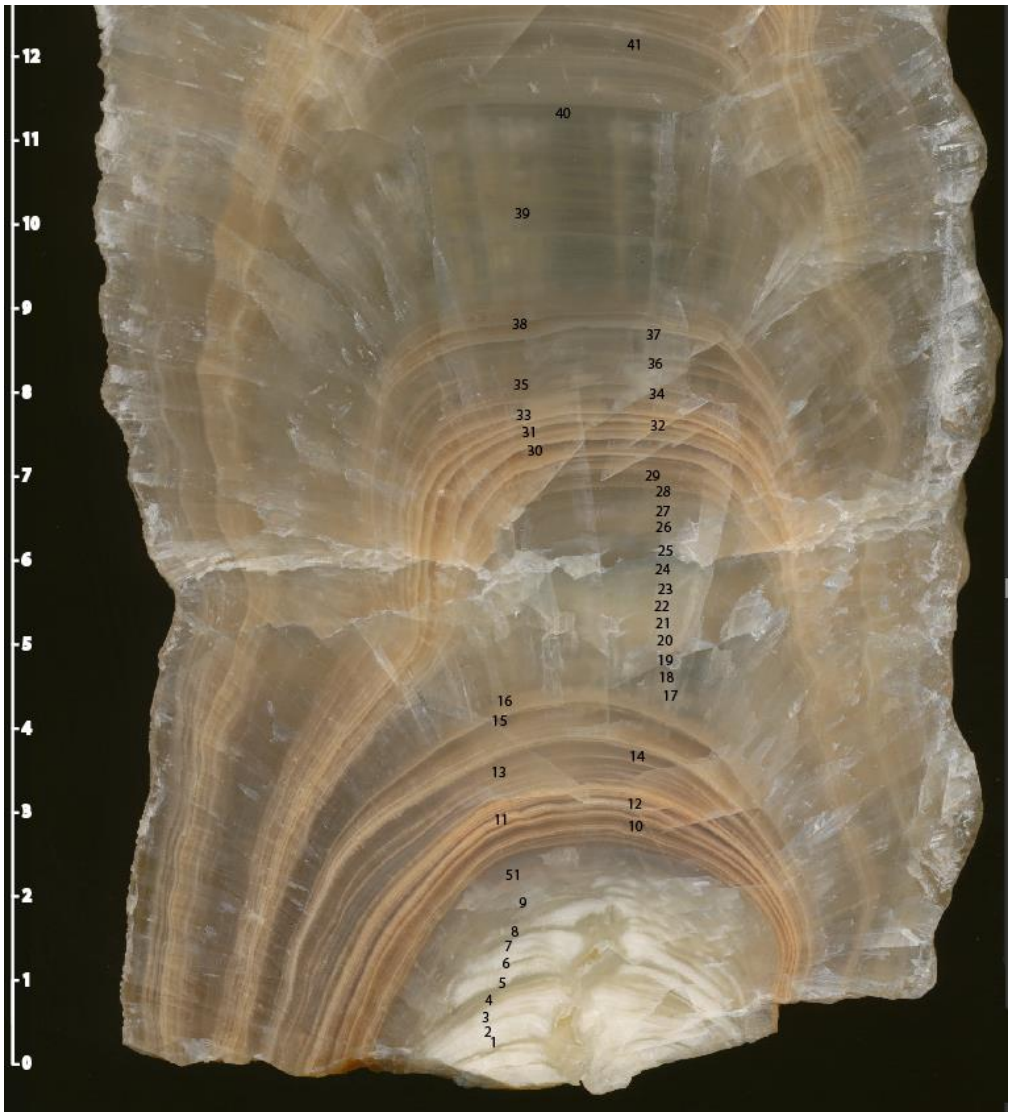

Figure 17: Locations of ^{232}Th and ^{238}U concentration sample analyses (Table 6). Approximately 5 mg of calcite powder was collected along forty-two laminae to determine layers with low ^{232}Th (< 1 ppb) concentrations.

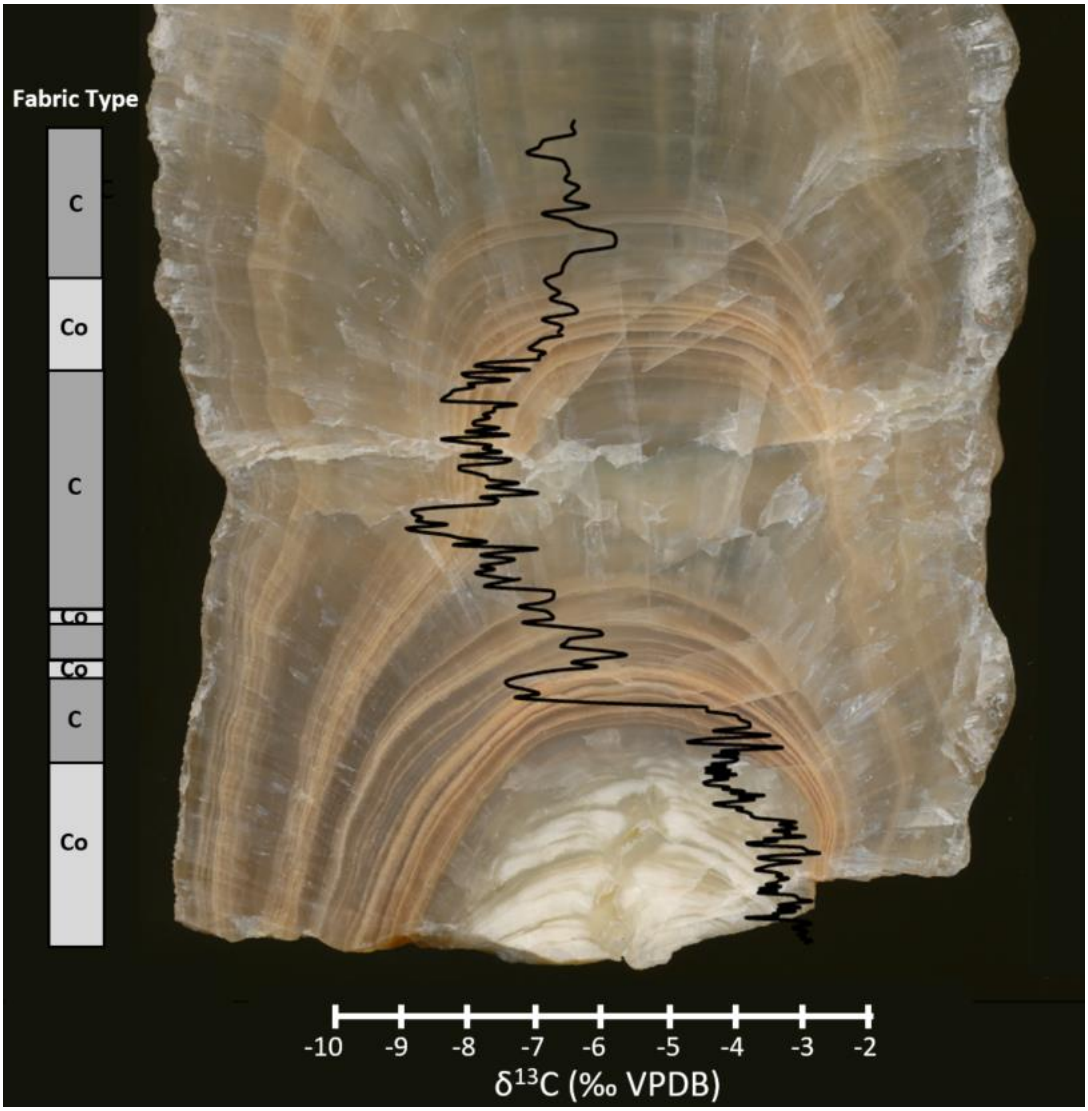

Figure 18: McN-1 $\delta^{13}C$ values and fabric types shown across sample McN-1. Decreases in $\delta^{13}C$ values are contemporaneous with columnar compact (C) fabric types. The decrease in $\delta^{13}C$ at the YD-Holocene transition occurs concurrently with the onset of brown/tan lamina (Interval B, Fig. 8). Contrastingly, an increase in $\delta^{13}C$ at ~8,500 yrs BP begins at the onset of a stratigraphically higher section of brown/tan lamina (Interval D).

Table 1. U-series dating results for Stalagmite McN-1. Quoted errors are 2σ.

Sample Number	Distance From Top (mm)	^{238}U (ppb)	^{232}Th (ppt)	^{230}Th / ^{232}Th (atomic x10^{-6})	$\delta^{234}U^{*}$ (measured)	^{230}Th / ^{238}U (activity)	^{230}Th Age (yr) (uncorrected)	^{230}Th Age (yr) (corrected)	$\delta^{234}U_{initial}^{**}$ (corrected)	^{230}Th Age (yr BP)*** (corrected)
McN-2	575.63	326 ±0	196 ±5	3312.5 ±91.3	139.3 ±1.5	0.1211 ±0.0004	12227 ±44	**12176 ±48**	144 ±2	**12114 ±48**
McN-3	568.22	172.6 ±0.2	61 ±3	5518 ±311	142.4 ±1.6	0.1179 ±0.0006	11849 ±70	**11819 ±71**	147 ±2	**11757 ±71**
McN-4	562.34	166.1 ±0.2	201 ±7	1633 ±55	137.3 ±1.5	0.1200 ±0.0004	12130 ±50	**12027 ±63**	142 ±2	**11965 ±63**
McN-5	554.99	160 ±0	279 ±9	1137.9 ±35.9	135.1 ±1.7	0.1201 ±0.0005	12166 ±62	**12018 ±82**	140 ±2	**11956 ±82**
McN-1b	551.88	173.0 ±0.5	248 ±4	1363 ±32	145.7 ±4.6	0.1182 ±0.0021	11935 ±230	**11813 ±231**	144 ±5	**11751 ±231**
McN-6	540.88	155.7 ±0.1	4864 ±100	63 ±1	119.2 ±1.8	0.1200 ±0.0005	12340 ±56	**9595 ±1007**	122 ±2	**9533 ±1007**
McN-7-1	539.12	151.2 ±0.2	6111 ±126	55 ±1	128.9 ±1.4	0.1339 ±0.0012	13731 ±131	**10201 ±1300**	133 ±1	**10139 ±1300**
McN-8-1	534.35	173.7 ±0.2	326 ±10	916 ±30	129.3 ±1.9	0.1042 ±0.0010	10739 ±115	**10574 ±129**	113 ±2	**10512 ±129**
McN-9	532.00	126.8 ±0.1	2361 ±48	98 ±2	124.9 ±1.7	0.1106 ±0.0003	11268 ±38	**9650 ±594**	128 ±2	**9588 ±594**
McN-9-rep	532.00	183.2 ±0.2	3577 ±73	97 ±2	125.7 ±1.7	0.1152 ±0.0005	11753 ±58	**10057 ±624**	129 ±2	**9995 ±624**
McN-10	530.00	179.0 ±0.2	1732 ±38	172 ±4	128.7 ±1.6	0.1008 ±0.0010	10181 ±106	**9345 ±323**	132 ±2	**9283 ±323**
McN-11	528.11	199.2 ±0.3	427 ±10	684 ±15	125.6 ±1.8	0.0889 ±0.0003	8958 ±35	**8773 ±76**	129 ±2	**8711 ±76**
McN-13	523.99	210.4 ±0.3	254 ±7	1186 ±31	125.7 ±1.4	0.0869 ±0.0004	8747 ±43	**8643 ±58**	129 ±1	**8581 ±58**
McN-14	522.11	103.0 ±0.1	104 ±3	1416 ±45	123.1 ±1.4	0.0868 ±0.0004	8762 ±41	**8675 ±52**	126 ±1	**8613 ±52**
McN-16	518.00	239.5 ±0.2	788 ±19	440 ±11	120.4 ±1.4	0.0878 ±0.0008	8885 ±80	**8600 ±132**	123 ±1	**8538 ±132**
McN-17	509.71	262.6 ±0.3	1205 ±25	321 ±7	142.5 ±2.0	0.0895 ±0.0004	8877 ±41	**8486 ±149**	146 ±2	**8424 ±149**
McN-18	505.30	255.1 ±0.3	219 ±9	1616 ±65	120.8 ±1.3	0.0843 ±0.0004	8520 ±48	**8445 ±55**	124 ±1	**8383 ±55**
McN-IS-2	503.06	276.9 ±0.3	5605 ±113	88 ±2	121.7 ±1.4	0.1081 ±0.0003	11035 ±31	**9268 ±648**	125 ±1	**9206 ±648**
McN-20	494.50	553.7 ±1.0	11806 ±241	84 ±2	120.2 ±1.7	0.1083 ±0.0005	11066 ±56	**9202 ±685**	123 ±2	**9140 ±685**
McN-21	491.33	234.1 ±0.2	4707 ±96	88 ±2	121.8 ±1.5	0.1071 ±0.0004	10918 ±44	**9163 ±644**	125 ±2	**9101 ±644**
McN-22	483.39	274.8 ±0.3	2316 ±48	175 ±4	117.1 ±1.6	0.0893 ±0.0006	9067 ±65	**8332 ±277**	120 ±2	**8270 ±277**
McN-23	479.95	377.3 ±0.6	224 ±6	2003 ±54	119.8 ±2.2	0.0721 ±0.0003	7246 ±31	**7194 ±36**	122 ±2	**7132 ±36**
McN-24	473.34	297.9 ±0.3	466 ±11	732 ±17	117.7 ±1.4	0.0695 ±0.0003	6994 ±35	**6858 ±61**	120 ±1	**6796 ±61**
McN-25	459.93	648.7 ±1.1	356 ±9	1920 ±46	107.2 ±1.5	0.0640 ±0.0002	6483 ±22	**6435 ±28**	109 ±2	**6373 ±28**
McN-25-rep	459.93	679.9 ±1.2	268 ±7	2674 ±70	107.4 ±1.9	0.0640 ±0.0002	6484 ±25	**6449 ±28**	109 ±2	**6387 ±28**
McN-26	450.67	679.6 ±1.1	2968 ±61	252 ±5	106.0 ±1.6	0.0669 ±0.0002	6794 ±22	**6409 ±142**	108 ±2	**6347 ±142**
McN-IS-1	442.38	1030.3 ±1.6	7475 ±31	159 ±4	114.9 ±2.8	0.0699 ±0.0018	7078 ±185	**6443 ±246**	115 ±3	**6381 ±246**
McN-27	353.83	243.4 ±0.3	917 ±20	186 ±4	112.9 ±1.3	0.0425 ±0.0004	4241 ±38	**3911 ±127**	114 ±1	**3849 ±127**
McN-28	195.88	194.9 ±0.2	1647 ±34	35 ±1	123.8 ±1.9	0.0178 ±0.0005	1739 ±50	**1005 ±273**	124 ±2	**943 ±273**
McN-28-rep	195.88	147.7 ±0.2	1569 ±33	36 ±1	107.6 ±1.7	0.0230 ±0.0005	2290 ±52	**1352 ±347**	108 ±2	**1290 ±347**
McN-29	111.65	99.1 ±0.1	545 ±12	43 ±3	103.5 ±1.5	0.0144 ±0.0009	1433 ±87	**947 ±198**	104 ±1	**885 ±198**

*$\delta^{234}U = ([^{234}U/^{238}U]_{activity} - 1)x1000$. ** $\delta^{234}U_{initial}$ was calculated based on ^{230}Th age (T), i.e., $\delta^{234}U_{initial} = \delta^{234}U_{measured} \times e^{\lambda 234 T}$.
***B.P. stands for "Before Present" where the "Present" is defined as the year 1950 A.D.

Table 1: U-series dating results for Stalagmite McN-1. Errors are reported as 2σ. ^{230}Th measurements that do not include the initial $^{230}Th/^{232}Th$ correction are labeled "uncorrected". Corrected ^{230}Th measurements are calculated using the isochron-derived initial $^{230}Th/^{232}Th$ value of 14.7 ± 3.8e-6. The ^{230}Th age was determined using the $^{230}Th/^{238}U$ decay equation from Broecker, (1963). Initial $\delta^{234}U$ values are based on the corrected ^{230}Th age. Replicate analyses from samples McN-9, 25 and 28 have 2σ errors < 290 yrs BP.

Table 2: McN-1 Carbon and oxygen isotope values, measured depths from the top, and sample ID's.

Sample ID	Depth (mm)	$\delta^{18}O$ (‰ VPDB)	$\delta^{13}C$ (‰ VPDB)
4	579.9	-3.98	-2.98
6	579.7	-4.17	-2.96
8	579.5	-4.09	-3.05
10	579.3	-4.25	-2.93
12	579.1	-3.79	-3.13
14	578.9	-4.00	-2.88
16	578.7	-3.98	-3.01
18	578.5	-3.91	-3.23
20	578.3	-3.68	-3.14
22	578.1	-3.72	-2.79
24	577.9	-3.38	-2.96
28	577.5	-3.79	-3.36
32	577.1	-4.21	-4.14
36	576.7	-3.77	-3.64
36-rep	576.7	-3.58	-3.61
38	576.5	-3.28	-3.11
40	576.3	-3.49	-3.52
42	576.1	-3.80	-3.01
44	575.9	-3.07	-3.50
48	575.5	-2.60	-2.94
48-rep	575.5	-2.82	-3.25
50	575.3	-2.86	-3.12
52	575.1	-3.19	-3.15
56	574.7	-3.02	-3.25
60	574.3	-2.91	-3.90
64	573.9	-2.68	-3.55
66	573.7	-2.77	-3.87
68	573.5	-3.39	-3.41
68-rep	573.5	-3.18	-3.75
72	573.1	-3.41	-3.45
72-rep	573.1	-3.49	-3.55
76	572.7	-3.02	-3.32
80	572.3	-3.12	-3.54
82	572.1	-2.84	-3.46
84	571.9	-3.16	-3.61
88	571.5	-3.07	-3.95
92	571.1	-3.29	-3.85

Table 2 Continued: McN-1 Carbon and oxygen isotope values, measured depths from the top, and sample ID's.

Sample ID	Depth (mm)	$\delta^{18}O$ (‰ VPDB)	$\delta^{13}C$ (‰ VPDB)
96	570.7	-3.49	-3.71
98	570.5	-4.14	-3.46
98-rep	570.5	-3.91	-3.19
100	570.3	-3.89	-3.69
104	569.9	-3.47	-3.90
108	569.5	-3.39	-3.54
112	569.1	-3.68	-2.63
112-rep	569.1	-3.33	-2.93
114	568.9	-3.33	-2.99
116	568.7	-3.83	-3.09
120	568.3	-3.76	-4.01
124	567.9	-3.48	-4.12
128	567.5	-3.55	-3.55
130	567.3	-3.98	-3.10
130-rep	567.3	-3.98	-3.77
132	567.1	-3.78	-3.38
136	566.7	-3.75	-3.30
140	566.3	-3.79	-3.61
140-rep	566.3	-3.73	-3.11
144	565.9	-3.92	-3.27
146	565.7	-3.69	-3.49
148	565.5	-4.03	-3.17
152	565.1	-4.23	-3.48
156	564.7	-3.82	-3.91
160	564.3	-3.85	-4.04
162	564.1	-3.89	-4.04
164	563.9	-3.97	-4.15
168	563.5	-4.36	-4.32
172	563.1	-4.64	-4.22
174	562.9	-4.48	-4.61
176	562.7	-4.32	-4.75
180	562.3	-4.61	-4.36
184	561.9	-4.13	-3.98
188	561.5	-3.78	-4.26
190	561.3	-3.70	-3.92
192	561.1	-3.50	-4.41

Table 2 Continued: McN-1 Carbon and oxygen isotope values, measured depths from the top, and sample ID's.

Sample ID	Depth (mm)	$\delta^{18}O$ (‰ VPDB)	$\delta^{13}C$ (‰ VPDB)
196	560.7	-3.28	-4.18
200	560.3	-3.63	-4.58
204	559.9	-3.63	-4.48
208	559.5	-3.44	-4.87
212	559.1	-3.55	-4.96
216	558.7	-3.31	-4.82
218	558.5	-3.60	-4.49
220	558.3	-3.14	-4.75
222	558.1	-3.37	-4.51
224	557.9	-3.32	-4.91
226	557.7	-3.65	-4.64
228	557.5	-3.41	-4.92
230	557.3	-3.69	-4.74
232	557.1	-3.69	-4.80
234	556.9	-3.64	-4.64
236	556.7	-3.72	-4.47
236-rep	556.7	-3.81	-4.47
238	556.5	-3.91	-4.49
240	556.3	-3.72	-4.62
242	559.1	-3.70	-4.61
244	558.3	-3.70	-4.43
248	557.7	-3.71	-4.61
258	557.3	-3.78	-4.71
262	556.7	-3.67	-5.01
274	556.1	-3.86	-4.03
278	555.7	-3.76	-4.20
288	554.7	-3.49	-3.33
302	553.3	-4.03	-4.70
304	553.1	-3.89	-4.42
308	552.7	-3.45	-3.50
315	552.0	-3.88	-4.34
318	551.7	-3.79	-3.65
320	551.5	-3.67	-3.64
322	551.3	-3.79	-3.95
326	550.9	-3.68	-4.02
330	550.5	-3.94	-4.29
332	550.3	-3.98	-4.29
336	549.9	-4.25	-6.28
340	549.5	-4.35	-7.16

Table 2 Continued: McN-1 Carbon and oxygen isotope values, measured depths from the top, and sample ID's.

Sample ID	Depth (mm)	$\delta^{18}O$ (‰ VPDB)	$\delta^{13}C$ (‰ VPDB)
342	549.3	-4.26	-7.00
345	549.0	-4.01	-7.13
346	548.9	-4.14	-7.45
350	548.5	-4.02	-7.45
352	548.3	-4.05	-7.37
354	548.1	-3.93	-6.93
356	547.9	-4.14	-6.76
360	547.5	-3.94	-6.10
368	546.7	-4.22	-6.46
370	546.5	-4.11	-6.10
374	546.1	-4.15	-5.66
379	545.6	-3.95	-6.49
384	545.1	-4.26	-6.40
384-rep	545.1	-4.18	-6.49
387	544.8	-4.47	-6.02
394	544.1	-4.01	-6.07
399	543.6	-3.73	-6.64
402	543.3	-3.91	-7.07
414	542.1	-3.63	-6.62
432	540.3	-3.94	-7.63
434	540.1	-3.96	-7.47
445	539.0	-4.05	-6.76
461	537.4	-3.83	-7.63
470	536.5	-4.34	-7.46
480	535.5	-4.27	-7.12
481	539.0	-4.17	-7.40
486	537.4	-4.21	-7.60
491	536.5	-4.16	-7.40
498	535.5	-4.28	-7.23
518	534.7	-4.46	-7.46
526	533.9	-4.49	-7.12
536	529.9	-4.62	-7.32
545	529.0	-4.56	-7.59
560	530.5	-4.45	-7.92
566	529.9	-5.02	-7.32
570	529.5	-4.57	-7.72
578	528.7	-4.44	-7.48

Table 2 Continued: McN-1 Carbon and oxygen isotope values, measured depths from the top, and sample ID's.

Sample ID	Depth (mm)	$\delta^{18}O$ (‰ VPDB)	$\delta^{13}C$ (‰ VPDB)
580	528.5	-4.30	-6.97
586	527.9	-4.68	-8.14
592	527.3	-4.65	-7.75
604	526.1	-4.35	-8.04
615	525.0	-4.32	-8.39
616	524.9	-4.56	-8.72
622	524.3	-4.65	-8.90
630	523.5	-4.55	-8.37
632	523.3	-4.74	-8.74
637	522.8	-4.74	-8.77
640	522.5	-4.80	-8.80
642	522.3	-4.97	-8.81
645	522.0	-5.20	-8.52
656	520.9	-4.19	-7.65
660	520.5	-4.52	-7.65
664	520.1	-4.25	-7.70
666	519.9	-4.51	-7.04
668	519.7	-4.98	-7.33
676	518.9	-5.09	-7.63
679	518.6	-4.79	-7.24
681	518.4	-4.67	-7.58
682	518.3	-4.61	-7.85
685	518.0	-4.85	-7.94
700	516.5	-4.42	-8.06
706	515.9	-4.53	-8.06
710	515.5	-4.24	-7.36
711	515.4	-4.14	-7.37
718	514.7	-4.16	-8.03
720	514.5	-3.89	-7.52
722	514.3	-3.96	-7.68
730	513.5	-3.78	-7.56
741	512.4	-4.32	-8.15
746	511.9	-4.28	-8.32
748	511.7	-4.31	-7.40
760	510.5	-4.80	-8.07
770	509.5	-4.51	-7.42
774	509.1	-4.93	-7.95
780	508.5	-4.17	-7.82

Table 2 Continued: McN-1 Carbon and oxygen isotope values, measured depths from the top, and sample ID's.

Sample ID	Depth (mm)	$\delta^{18}O$ (‰ VPDB)	$\delta^{13}C$ (‰ VPDB)
786	507.9	-4.36	-7.58
788	507.7	-3.68	-7.67
790	507.5	-3.57	-7.50
792	507.3	-3.66	-7.50
793	507.2	-3.78	-7.30
798	506.7	-4.62	-8.34
799	506.6	-4.66	-8.30
802	506.3	-4.54	-8.14
804	506.1	-4.81	-8.15
805	506.0	-5.00	-7.94
806	505.9	-4.80	-7.91
814	505.1	-4.34	-7.26
820	504.5	-4.47	-7.92
825	504.0	-4.92	-8.12
840	502.5	-4.53	-6.94
846	501.9	-4.32	-7.80
850	501.5	-4.58	-7.64
860	500.5	-4.41	-6.79
864	500.1	-5.08	-6.73
867	499.8	-5.02	-6.82
868	499.7	-5.03	-6.88
870	499.5	-4.45	-6.88
872	499.3	-4.66	-6.75
876	498.9	-4.61	-6.84
880	498.5	-5.23	-6.41
880-rep	498.5	-5.14	-6.26
890	499.8	-4.66	-6.88
900	499.7	-4.56	-7.55
910	499.5	-4.40	-6.68
920	499.3	-4.85	-6.91
924	498.9	-4.73	-6.99
927	498.5	-4.66	-7.00
938	497.9	-5.24	-7.13
948	496.9	-4.74	-7.05
954	496.3	-4.82	-7.50
966	495.1	-4.33	-6.72

Table 2 Continued: McN-1 Carbon and oxygen isotope values, measured depths from the top, and sample ID's.

Sample ID	Depth (mm)	$\delta^{18}O$ (‰ VPDB)	$\delta^{13}C$ (‰ VPDB)
972	494.5	-4.60	-6.83
978	493.9	-4.52	-7.33
984	493.3	-4.50	-7.13
990	492.7	-4.51	-7.37
996	492.1	-4.86	-7.47
1008	490.9	-4.86	-7.11
1014	490.3	-4.60	-7.07
1022	489.5	-4.44	-6.98
1026	489.1	-4.46	-6.81
1032	488.5	-4.70	-5.91
1038	487.9	-4.41	-5.85
1044	487.3	-4.51	-5.95
1050	486.7	-4.67	-6.69
1056	486.1	-5.29	-7.01
1068	484.9	-4.99	-7.58
1074	484.3	-4.45	-6.52
1082	483.5	-4.69	-7.06
1086	483.1	-4.54	-6.93
1092	482.5	-4.50	-6.76
1098	481.9	-4.30	-7.08
1102	481.5	-4.59	-7.00
1110	480.7	-4.40	-7.05
1116	480.1	-4.35	-7.17
1122	479.5	-4.39	-7.97
1128	478.9	-4.28	-7.71
1134	478.3	-3.98	-7.60
1142	477.5	-4.18	-6.89
1146	477.1	-4.03	-7.03
1150	476.7	-4.05	-6.95

^{230}Th dating results. The error is 2σ.

Sample Number	Distance From Top (mm)	^{238}U (ppb)	^{232}Th (ppt)	^{230}Th / ^{232}Th (atomic x10^{-6})	δ^{234}U (measured)	^{230}Th / 238U (activity)	^{230}Th Age (yr) (uncorrected)	^{230}Th Age (yr) (corrected)	$\delta^{234}U_{Initial}$ (corrected)	^{230}Th Age (yr BP) (corrected)	Isochron-derived initial ^{230}Th/^{232}Th
MCN-7-1	539.12	151.2 ±0.2	6111 ±126	55 ±1	128.9 ±1.4	0.1339 ±0.0012	13731 ±131	**10201 ±1300**	133 ±1	**10139 ±1300**	
MCN-7-2	539.12	170.0 ±0.2	4207 ±84	83 ±2	130.6 ±1.3	0.1244 ±0.0003	12683 ±36	**10537 ±786**	135 ±1	**10475 ±786**	27.0 ±76
MCN-7-3	539.12	178.6 ±0.2	4581 ±92	74 ±1	130.3 ±1.6	0.1155 ±0.0003	11732 ±37	**9507 ±816**	134 ±2	**9445 ±816**	
MCN-8-1	534.35	173.7 ±0.2	326 ±10	916 ±30	129.3 ±1.9	0.1042 ±0.0010	10739 ±115	**10574 ±129**	113 ±2	**10512 ±129**	
MCN-8-2	534.35	179.5 ±0.2	3976 ±80	89 ±2	127.9 ±1.4	0.1197 ±0.0003	12206 ±34	**10284 ±705**	132 ±1	**10222 ±705**	14.7 ±4
MCN-8-3	534.35	137.5 ±0.1	9354 ±187	39 ±1	124.5 ±1.4	0.1625 ±0.0004	16969 ±54	**10941 ±2212**	128 ±2	**10879 ±2212**	

Table 3: Reported are ^{238}U and ^{232}Th concentrations, corrected and uncorrected ^{230}Th ages, and δ^{234}U for the two isochron samples from McN-1. The McN-7 isochron series are not used in the calculation of the initial ^{230}Th/^{232}Th due to there being two values (McN-7-2 and McN-7-3) with similar ^{232}Th concentrations. These similarities yield a large isochron-derived ^{230}Th/^{232}Th error (+/- 76 ppm), which is not useful in constraining initial ^{230}Th/^{232}Th. All isochron-derived ages and ^{230}Th/^{232}Th are listed in Table S4.

Sample ID	Distance from top (mm)	^{230}Th age (yrs BP)	^{230}Th age error (2σ)	a^{14}Cmeas (pMC)	a^{14}Cmeas error (2σ)	DCP (%)	DCP error (2σ)
C-1	575.6	12,114	48	25.46	0.10	7.83	0.84
C-2	562.3	11,965	82	25.74	0.12	8.41	1.10
C-3	551.9	11,751	231	26.55	0.10	6.59	2.65
C-4	550.4	11,717	242	26.41	0.11	7.13	2.75
C-5	543.0	11,453	190	28.74	0.10	0.04	2.33
C-6	543.4	10,830	284	31.39	0.11	-3.51	3.58
C-7	534.4	10,512	129	32.11	0.11	-2.20	2.33
C-8	530.0	9,283	323	34.23	0.11	4.08	3.77
C-9	526.4	8,630	307	36.60	0.12	2.59	3.64
C-10	483.4	8,270	277	40.96	0.12	-3.08	3.47

Table 4: Shown are the measured speleothem ^{14}C activities (a^{14}Cmeas) in percent modern carbon (pMC), and calculated DCP values with their associated uncertainties. The ^{230}Th ages used to calculated DCP are shown in yrs BP.

Publication	Location	Mean DCP (%)	Mean Annual Rainfall (mm/yr)
Noronha et al., 2014	Heshang Cave (SW China)	11	1,400
Genty and Massault, 1999	Villars, France	9	1,000
Genty and Massault, 1999	La Faurie, France	9	900
Genty et al., 1999 and Genty et al., 1998	Han-sur-Lease, Belgium	17	1,300
Genty et al., 1999	Browns Folly Mine, England	18	800
Genty et al., 1999	Sutherland, Scotland	32	>1,900
Griffiths et al., 2012	Flores, Indonesia	35	2,000
Genty et al., 1999	Postojna, Slovenia	12	1,500

Table 5: List of DCP from modern speleothems and annual rainfall totals for the respective regions. Higher DCP values are observed in regions with higher annual rainfall. The positive correlation between DCP and annual rainfall (r^2=0.62, n=8) suggests rainfall can be a strong control on DCP. Sample McN-1 fits into the drier portion of the correlated data, with mean DCP values of 4% and annual rainfall totaling 800 mm/yr.

Parallel Track Data			
Transect 1		Transect 2	
Sample ID	$\delta^{18}O$ (‰ VPDB)	Sample ID	$\delta^{18}O$ (‰ VPDB)
212	-3.55	242	-3.70
216	-3.31	244	-3.70
218	-3.60	248	-3.71
220	-3.14	258	-3.78
222	-3.37	262	-3.67
224	-3.32	274	-3.86
226	-3.65	278	-3.76
228	-3.41	-	-
230	-3.69	-	-
232	-3.69	-	-
234	-3.64	-	-
236	-3.72	-	-
236	-3.42	-	-
238	-3.91	-	-
240	-3.72	-	-
Average			
Transect 1	-3.56	*Transect 2*	-3.74
Std dev.	**0.09**		

Parallel Track Data			
Transect 1		Transect 2	
Sample ID	$\delta^{13}C$ (‰ VPDB)	Sample ID	$\delta^{13}C$ (‰ VPDB)
212	-4.96	242	-4.61
216	-4.82	244	-4.43
218	-4.49	248	-4.61
220	-4.75	258	-4.71
222	-4.51	262	-5.01
224	-4.91	274	-4.03
226	-4.64	278	-4.20
228	-4.92	-	-
230	-4.74	-	-
232	-4.80	-	-
234	-4.64	-	-
236	-4.47	-	-
236	-4.33	-	-
238	-4.49	-	-
240	-4.62	-	-
Average			
Transect 1	-4.67	*Transect 2*	-4.51
Std dev.	**0.08**		

Transect 2		Transect 3	
Sample ID	$\delta^{18}O$ (‰ VPDB)	Sample ID	$\delta^{18}O$ (‰ VPDB)
445	-4.05	481	-4.17
461	-3.83	486	-4.21
470	-4.34	491	-4.16
480	-4.27	498	-4.28
Average			
Transect 2	-4.12	*Transect 3*	-4.20
Std dev.	**0.04**		

Transect 2		Transect 3	
Sample ID	$\delta^{13}C$ (‰ VPDB)	Sample ID	$\delta^{13}C$ (‰ VPDB)
445	-6.76	480	-7.40
461	-7.63	481	-7.60
470	-7.46	486	-7.40
480	-7.12	491	-7.23
Average			
Transect 2	-7.24	*Transect 3*	-7.41
Std dev.	**0.08**		

Transect 3		Transect 4	
Sample ID	$\delta^{18}O$ (‰ VPDB)	Sample ID	$\delta^{18}O$ (‰ VPDB)
840	-4.53	890	-4.66
846	-4.32	900	-4.56
850	-4.58	910	-4.40
860	-4.41	920	-4.85
864	-5.08	924	-4.73
867	-5.02	927	-4.66
868	-5.03	938	-5.24
870	-4.45	948	-4.74
872	-4.66	-	-
876	-4.61	-	-
880	-5.23	-	-
Average			
Transect 3	-4.72	*Transect 4*	-4.73
Std dev.	**0.01**		

Transect 3		Transect 4	
Sample ID	$\delta^{13}C$ (‰ VPDB)	Sample ID	$\delta^{13}C$ (‰ VPDB)
840	-6.94	890	-6.88
846	-7.80	900	-7.55
850	-7.64	910	-6.68
860	-6.79	920	-6.91
864	-6.73	924	-6.99
867	-6.82	927	-7.00
868	-6.88	938	-7.13
870	-6.88	940	-7.05
872	-6.75	-	-
876	-6.84	-	-
880	-6.41	-	-
Average			
Transect 3	-6.95	*Transect 4*	-7.02
Std dev.	**0.04**		

Table 6: Carbon and oxygen isotope values along parallel transects 1,2,3 and 4 (see Fig. 3b for transect locations). Both $\delta^{13}C$ and $\delta^{18}O$ along each overlapping transect show similar values [< 0.1‰ (2σ)] indicating that kinetic processes are not controlling McN-1 $\delta^{13}C$ or $\delta^{18}O$.

Sample ID	^{232}Th (ppb)	^{238}U (ppb)	Sample ID	^{232}Th (ppb)	^{238}U (ppb)	Sample ID	^{232}Th (ppb)	^{238}U (ppb)	Sample ID	^{232}Th (ppb)	^{238}U (ppb)
Dilution factor-adjusted concentrations (ppb)						Calibration standards			Blank (2% HNO3) replicates		
1	< LOD	162.260	22	< LOD	145.781	Blank	0.00000	0.00000	ccb1	-0.006	0.001
2	< LOD	148.529	23	< LOD	170.600	Std2	0.08601	0.09345	ccb2	-0.005	0.000
3	< LOD	138.694	24	< LOD	195.031	Std3	0.9219	0.96	ccb3	-0.007	-0.002
4	< LOD	122.683	25	< LOD	154.453	Std4	9.708	9.717	ccb4	-0.008	-0.003
5	< LOD	163.498	26	< LOD	173.205	Std5	100.9	101	ccb5	-0.007	-0.003
6	< LOD	129.005	27	< LOD	201.381	Std6	201.4	201.3	ccb6	-0.005	-0.002
7	< LOD	132.401	28	1.584	206.259	***Rho***	***1.0000***	***1.0000***	ccb7	-0.006	-0.001
8	< LOD	131.342	29	< LOD	< LOD	QC1 recoveries			ccb8	-0.014	-0.003
9	< LOD	121.558	30	< LOD	177.768	QC1	9.786	9.643	ccb9	-0.007	-0.001
10	5.423	91.006	31	< LOD	189.402	QC1	9.718	9.554	ccb10	-0.016	-0.004
11	17.803	87.627	32	8.674	201.212	***Recovery***	***0.920***	***0.860***	ccb11	-0.016	-0.003
12	1.681	88.164	33	< LOD	164.435	QC2 recoveries			ccb12	-0.017	-0.004
13	< LOD	124.845	34	< LOD	188.995	QC2	9.762	9.554	ccb13	-0.016	-0.004
14	< LOD	139.871	35	< LOD	185.842	QC2	9.665	9.477	ccb14	-0.012	-0.003
15	< LOD	141.717	36	< LOD	200.905	QC2	8.96	8.425	ccb15	-0.014	-0.004
16	< LOD	121.303	37	< LOD	174.719	QC2	8.519	7.814	ccb16	-0.010	-0.004
17	< LOD	129.039	38	< LOD	206.766	QC2	8.483	7.686	ccb17	-0.011	-0.003
18	< LOD	142.690	39	< LOD	270.399	QC2	8.664	7.894	***LOD***	***0.009***	***0.003***
19	< LOD	149.373	40	< LOD	271.648	QC2	9.872	8.889			
20	< LOD	158.709	41	< LOD	494.278	***Recovery***	***0.920***	***0.860***			
21	< LOD	172.853	51	< LOD	127.193						

Table 7: ^{232}Th and ^{238}U concentrations of McN-1 lamina are listed in parts per billion (ppb). Analytes were used to select ideal U-series dates by indicating which lamina contained low ^{232}Th (< 1ppb). The limit of detection (LOD) indicates the lowest concentration that can be detected with 95% confidence of the measurement being above the background signal. Concentrations that are below the LOD are flagged as "< LOD". Limits of detection (LOD) for ^{232}Th and ^{238}U are 0.009 and 0.003 ppb, respectively. Linear calibration coefficients (rho) are shown as determined from the analyte calibration curves. Quality control standards include two lab fortified matrix spikes (QC1 and QC2). Samples with ^{232}Th concentrations higher than the LOD are highlighted in grey, with these laminae avoided for U-series dating due to concentrations higher than 1 ppb.

Publication	Proxy Type	Location	Time Interval (ka)	Moisture Interpretation of Early Holocene Climate relative to Late Pleistocene Climate
Nordt et al., 1994	Alluvial deposit and soil $\delta^{13}C$	Fort Hood, TX	15 to 0	Drier
Toomey et al., 1993	Flora and faunal assemblages	Hall's Cave, TX	20 to 0	Drying trend began before the YD
Ellwood and Gose, 2006	Magnetic susceptibility	Hall's Cave, TX	19 to 0.5	Drying trend began before the YD
Polyak et al., 2004	Speleothems	Guadalupe Mountains, NM	14.5 to 10	Drier
Holliday et al., 2011	Soil $\delta^{13}C$	Central Texas	18 to 0	Drier
Cooke et al., 2003	Cave-fill Sr isotopes	Central Texas	20 to 1.5	Drier
Holliday et al., 2001	Eolian deposits/Soil $\delta^{13}C$	Texas Southern High Plains	13 to 0	Drier

Table 8: Proxy records showing relative moisture changes from the Late Pleistocene to the Early Holocene. The time interval of each proxy record is shown. All listed moisture proxies show drier Early Holocene conditions, while the proxy records of Toomey et al. (1993) and Ellwood and Gose (2006) indicate a regional drying occurring before the YD (~14 ka).

Beginning of Interval	End of Interval	Growth Rates (μm/yr)
12114	12027	71
12027	11956	108
11956	11851	100
11851	10512	13
10512	9588	3
9588	9283	7
9283	8711	3
8711	8581	32
8581	8538	139
8538	8424	73
8424	8383	108
8383	8270	193
8270	7132	0
7132	6796	20

Table 9: Shown are McN-1 growth rates in μm/yr, and represent the average growth rate spanning the shown time intervals. Growth rates are calculated using the distances between two U-series ages and the difference in the respective ages.

APPENDICES

Appendix A: Methods

Chemical Separation

Chemical separation procedures for samples developed at UT Austin were similar to those described in Musgrove et al. (2001). Three full procedural blanks (FPBs) were passed through each chemical separation step plus filament loading to account for contamination during the full sample preparation procedure (Table S7). FPBs averaged <3 pg for U and <11 pg for Th, which corresponds to < 0.003% and 0.6% of measured U and Th, respectively. For U-series calibration and quality control, the U metal Certified Reference Standard NBL 112-A was analyzed at the beginning of each analytical session. All U-series samples were refluxed and dissolved with nitric acid (HNO_3). A U-Th spike containing ^{229}Th, ^{233}U and ^{236}U was added to each sample, the FPBs and NBL 112-A. U and Th were coprecipitated from the dissolved solution using $Fe(OH)_3$. To purify both U and Th, a two-column separation technique using anion exchange resin was performed with 750ul and 160ul columns. Two rounds of HNO_3 washes were added to the samples after being placed in the columns. Th was eluted with 6N HCL, and U was eluted with 1N HBr. Chemistry yields for UT Austin samples were 82% for Th and 45% for U.

Chemical separation of samples developed at UMN followed procedures from Edwards et al. (1987) and Dorale et al. (2005). Calcite samples were dissolved in nitric acid and spiked with a tracer containing ^{229}Th, ^{233}U and ^{236}U. The samples were then dried down and re-dissolved in HCl and an FeCl solution. Fe, U, and Th were co-precipitated with HN4OH and centrifuged to isolate the solid material. U and Th were separated by running the samples through 850 μl columns containing anion resin. A series of HNO_3

washes were added to the columns to purify the samples. Th was eluted with 6N HCl, and U was eluted with water. The samples were dried down and dissolved in HNO_3 for analysis. An FPB (FPB-4) was passed through each chemical separation step at UMN, with mean U and Th amounts of <0.5 pg for U and <0.05 pg for Th (Table S7).

Mass Spectrometry

A total of 25 U-series samples were analyzed at UMN on a Thermo-Scientific Neptune Plus MC-ICP-MS with an Aridus desolvating nebulizer. Samples were dried down and redissolved into a sample introduction solution containing HNO_3 and HF. Faraday cups were used for data acquisition and SEM dark noise (~0.5 cps) and counting efficiency (~100%) were monitored regularly. Before each sample analysis, the HNO_3-HF solution was introduced through the nebulizer and used to flush previous sample residue from the machine. After the HNO_3-HF wash, values of ^{234}U, ^{233}Th, and ^{235}U were measured from the same HNO_3-HF solution (machine blanks) and were ~ <0.1% of the sample U and Th cps. Measured $\delta^{234}U$ values of standard NBL-112A for all sessions had mean values of -38.1 ± 1.3‰ (2σ) (n=2). Instrument operating parameters and NBL-112A standard measurements are shown in Table S3.

Three of the U-series samples were measured at UT Austin on a Thermo-Scientific Triton TIMS. Each sample was dried and loaded with colloidal graphite onto Re filaments. U and Th samples were run in a single-filament configuration and measured using an ion-counting system. NBL-112A was analyzed and peak centering was conducted along masses 233, 234, 235, 236, and 238, with baselines that were measured to be <5 cps. Intensity bias was calibrated from measurements on NBL-112A and the correction was

applied to all measured isotope values. Filaments were prescreened for Th content prior to analysis of NBL-112A. Background intensities were measured from masses 230.55, 233.50, 234.50, and 235.55. The measured $\delta^{234}U$ value of the standard NBL 112-A was -37.7 ± 1.1‰ (2σ) (n=1), which is within error of the reported δ^{234} U value from the reported accepted $\delta^{234}U$ value of -36.9 ± 2.1‰ (2σ) (Cheng et al., 2000). No corrections to calculated U-series ages were made in comparing data processed at UT Austin and UMN. Instrument operating conditions for TIMS analysis of samples McN-IS-1 and McN-IS-2 are listed in Table S1, and the analytical sequence for measurements of U and Th is listed in Table S2.

Age Calculation

Ages were calculated using the $^{230}Th/^{238}U$ decay equation determined by Broecker, (1963):

$$\frac{^{230}Th}{^{238}U} = (1 - e^{-\lambda_{230} \cdot t}) + \frac{\lambda_{230}}{\lambda_{230} - \lambda_{234}} \cdot \left(\frac{^{234}U}{^{238}U} - 1 \right) \cdot \left(1 - e^{-(\lambda_{230} - \lambda_{234}) \cdot t} \right)$$

Where $^{230}Th/^{238}U$ is the activity ratio, "t" is the ^{230}Th age, and values for $\lambda_{230} = 9.1577 \times 10^{-6}$ y^{-1}, $\lambda_{234} = 2.8263 \times 10^{-6}$ y^{-1}, $\lambda_{238} = 1.55125 \times 10^{-10}$ y^{-1} (Cheng et al., 2000, and Jaffrey et al., 1971). The presence of ^{232}Th often indicates detrital contamination in calcite, and represents the potential for deposition of ^{230}Th from soil rather than from ^{238}U decay within the $^{230}Th/^{238}U$ closed system of precipitating calcite. Any outside ^{230}Th would overestimate the calculated ages.

Isochron

For samples with relatively low ^{232}Th concentrations, the age uncertainty due to the uncertainty on the initial ^{230}Th/^{232}Th ratio will be minimal (Dorale and Richards, 2003). However, samples with relatively high ^{232}Th concentrations will propagate large age errors and in some cases, result in negative calculated ages if there are large uncertainties in initial ^{230}Th/^{232}Th. To account for high concentrations of ^{232}Th present in our measured U-series samples and constrain the ^{230}Th/^{232}Th ratio, we calculate two isochrons using ISOPLOT 4.15 and according to the methods of Ludwig and Titterington (1994). Traditional U-Th isochrons use a coupled pair of isochrons (^{230}Th/^{232}Th versus ^{234}U/^{232}Th, and ^{234}U/^{232}Th versus ^{238}U/^{232}Th) to calculate an age (Rosholt, 1976). However, because ^{232}Th and ^{234}U are in both of these isochrons, correlations between these two isotopes (including the amount of U brought into the system from detrital material) are not fully taken into account, and can result in mixochrons with various material formed at different times. The Osmond Type-II diagram overcomes this limitation, by plotting ^{230}Th/^{238}U vs ^{232}Th/^{238}U; ^{234}U/^{238}U vs ^{232}Th/^{238}U; and ^{230}Th/^{238}U vs ^{234}U/^{238}Th. A 3-dimensional regression line is applied, where X = ^{230}Th/^{238}U, Y = ^{234}U/^{238}U, Z = ^{232}Th/^{238}U. Samples with variable ^{232}Th plot along the line extending in the z-direction, where the ^{232}Th-free ^{230}Th/^{238}U and ^{234}U/^{238}Th endmember intersect the XY plane (Fig. S1). An age and an initial ^{230}Th/^{232}Th is then calculated for the ^{232}Th-free endmember, representing values of the closed U-Th system (Fig. S1). Therefore, these results represent true isochrons, and not mixochrons. This method uses a procedure to weigh the data points via their analytical errors using an extension of the maximum-likelihood estimation method (MLE, Titterington and Halliday,

1979). The Mean Square of Weighted Deviates (MSWD) is calculated to quantify the amount of scatter about the regression line as a result of analytical errors.

Figure 3 shows the isochron sample locations (McN-8 and McN-7) on slabbed stalagmite McN-1, with three samples drilled along the same growth layer. Table S4 shows the activities of the three ^{230}Th-U isotope ratios, their analytical uncertainties, the calculated ages, MSWDs, and initial ^{230}Th/^{232}Th (^{230}Th/^{232}Th$_{initial}$) values for both isochron samples. Figure S1 shows the Osmond-Type II diagrams (^{230}Th/^{238}U vs. ^{232}Th/^{238}U), which are X-Y projections of the calculated three-dimensional isochron, where the isotope ratios of the ^{232}Th-free endmember are calculated from the intercept of the regression line. Individual data points are represented by three-dimensional error-ellipsoids.

^{232}Th concentrations for McN-7-2 and McN-7-3 are within 7% of each other, and ^{232}Th/^{238}U activity ratios have a standard deviation of 0.000147. Variable ^{238}U/^{232}Th values stem from there being less detrital contamination near the central growth axis and more contamination along the flanks of the growth layer. The similar ^{232}Th values observed in isochron McN-7 could be due to the selected sites being sampled too close to one another such that the difference in ^{232}Th is too small. We calculated initial ^{230}Th/^{232}Th values from two of the three points (Table S4) along McN-7. McN-7-2 and McN-7-3 (two samples that had similar ^{232}Th/^{238}U values) show an age and ^{230}Th/^{232}Th value that is not consistent with other calculated values (age = 42 ka, and ^{230}Th/^{232}Th = 162 ppm). The ^{230}Th/^{232}Th values and ages calculated from the remaining McN-7 two-point isochrons bracket values calculated from the McN-8 isochron. However, these values are not useful in constraining initial ^{230}Th/^{232}Th as the isochron-derived uncertainties would not be representative of the

$^{230}Th/^{232}Th$ in the McN-1 U-Th system due there only being two points in the calculation.

Drip water Dissolved Inorganic Carbon Isotope Model

The DIC carbon isotope model is based on the model from Fohlmeister et al. (2011). In this section, we discuss in detail how the model works as well as how to navigate the corresponding Fohlmeister et al. (2011) MATLAB code. This model contains several dissolution equations from Hendy (1971). Assumed values of $\delta^{13}C$ and ^{14}C are assigned to the initial $CO_{2(g)}$.

Step 1: Equilibrium between water and $CO_{2(g)}$

In the first step, water equilibrates with $CO_{2(g)}$ in an open system, and contains no Ca^{2+}. A pH value is calculated from a prescribed initial pCO_2 value. The concentration of $CO_{2(aq)}$ is calculated using the condition of electroneutrality and mass action relation via:

$$c_{CO_{2(aq)},initial} = \frac{c_{H^+}\left((c_{H^+})^2 - \frac{K_w}{\gamma_{H^+}\gamma_{OH^-}}\right)}{\frac{K_1\gamma_{CO_{2(aq)}}}{\gamma_{H^+}} \cdot \left(\frac{c_{H^+}}{\gamma_{HCO_3^-}} + \frac{2K_2}{\gamma_{H^+}\gamma_{CO_3^{2-}}}\right)}. \quad \text{Equation S1}$$

where the concentration of H^+ (c_{H+}) is given by initial pH, K values are equilibrium constants, and λ's are activity coefficients. Concentrations of OH^-, H_2CO_3, HCO_3^-, and CO_3^{2-}, are calculated using temperature dependent mass action relations and constants from Dreybrodt (1988), and activity coefficients using the extended Debye-Huckle equation.

Step 2: Open system dissolution

The next step involves calcite dissolution, where dissolution results in higher pH and a more alkaline solution. Therefore, the model considers calcite dissolution by

increasing the pH in 0.001 increments. At each pH increment, concentrations of all of the DIC species and OH^- are calculated under an open system using mass action relations, and the concentration of Ca^{2+} is then calculated from the equation of electroneutrality ($[H^+] + 2[Ca^{2+}] - [OH^-] - [HCO_3^-] - 2[CO_3^{2-}] = 0$. Concentrations of all species are calculated under open system conditions, where $CO_{2(aq)}$ is calculated from:

$$[CO_{2(aq)}] = K_H \cdot pCO_2 \qquad \text{Equation S2}$$

Dissolution under open system conditions is modeled up to a specific pH defined by $x \cdot Kc = Q$, where Q is the ion activity product and Kc is the equilibrium constant for the reaction:

$$Ca^{2+} + CO_3^{2-} \leftrightarrow CaCO_3 \qquad \text{Equation S3}$$

Under a completely open system, $x = 1$ ($Q = K_{calcite}$), the model calculates all concentrations under open system conditions until the dissolution process stops when saturation with respect to calcite has been established ($Q = K_{calcite}$). If $0<x<1$, the model will calculate the concentrations of the species under open system conditions until the pH value associated with $Q = K_{calcite} \cdot x$ is reached.

Step 3: $\delta^{13}C$ and ^{14}C of DIC under open system dissolution

After concentrations of the DIC, OH^- and Ca^{2+}species have been calculated, the $\delta^{13}C$ and ^{14}C values of DIC formed under open system conditions are modeled at each dissolution step using the temperature dependent isotope fractionation factors and known $\delta^{13}C$ and ^{14}C values of initial pCO_2 (Mook and de Vries, 2000; Salieges and Fontes, 1984). The $\delta^{13}C$ value of the total DIC is determined by mass balance calculations:

$$\delta^{13}C_t = \Sigma\, c_j\, \delta^{13}C_j / \Sigma c_j \qquad \text{Equation S4}$$

where j = $CO_{2(aq)}$, HCO_3^-, CO_3^{2-}.

Step 4: Closed system dissolution and mass balance calculations

From this point, the model calculates the remaining concentrations under closed system conditions until saturation is reached. If x = 0, Q = 0, and all $CaCO_3$ dissolution occurs under closed system conditions until saturation and the initial species concentrations for this calculation are those in equilibrium at the prescribed pCO_2. For 0<x<1, the last concentration values of the DIC species calculated from the open system ($c_{iopen,last}$) are used as initial values for the closed system. Mass conservation requires that under a closed system:

$$c_{CO_{2(aq)},initial} + c_{HCO_{3,initial}^-} + c_{CO_{3,initial}^{2-}} + c_{Ca^{2+}} = c_{CO_{2(aq)}} + c_{HCO_3^-} + c_{CO_3^{2-}}, \quad \text{Equation S5}$$

where initial concentrations refer to DIC species at the onset of closed system dissolution. As shown in equation S5, the concentration of calcite in the final solution ($c_{Ca^{2+}}$) accounts for the amount of carbon added as a result of calcite dissolution. Equation S5 and the mass action relations can be used to calculate the concentration of $CO_{2(aq)}$ in the closed system via:

$$c_{CO_{2(aq)}} = \frac{\frac{K_w}{c_{H^+}\gamma_{H^+}\gamma_{OH^-}} - c_{H^+} + 2 \cdot \Sigma CO_{2,initial}}{2 + \frac{K_1 \gamma_{CO_{2(aq)}}}{c_{H^+}\gamma_{H^+}\gamma_{HCO_3^-}}}, \quad \text{Equation S6}$$

The total dissolved inorganic carbon concentration in the solution at the onset of closed system dissolution is given by:

$$\Sigma CO_{2,initial} = c_{CO_{2(aq),open,last}} + c_{HCO^-_{3,open,last}} + c_{CO^{2-}_{3,open,last}} - c_{Ca^{2+}_{open,last}}. \quad \text{Equation S7}$$

where ($c_{iopen,last}$) are the last concentration values of the DIC species calculated for the open system, and used as initial values for the closed system.

Step 5: $\delta^{13}C$ and ^{14}C of DIC under closed system dissolution

$\delta^{13}C$ and ^{14}C values formed under closed system conditions consider the amount (isotopic composition) of carbon coming from host rock dissolution. The carbon isotope values after the dissolution step are calculated by:

$$\delta^{13}C_t(n) = (\delta^{13}C_t(n-1) \cdot \sum c_j(n-1) + \delta^{13}C_{CaCO_3} \cdot (c_{Ca^{2+}}(n) - c_{Ca^{2+}}(n-1))) \Big/ \sum c_j(n), \quad \text{Equation S8}$$

where n = the current dissolution step, c_j is the concentration of the DIC species, and $\delta^{13}C_{CaCO3}$ is the $\delta^{13}C$ value of the host rock. ^{14}C activity is also computed using equation S7.

Dissolution model MATLAB code

The MATLAB code for this model has several subroutines that link to the primary ("main 1") code. The open/closed ratio is referred to as "dcf" in all subroutines. Temperature can be changed in "parameter.txt". Initial CO_2 $\delta^{13}C$ and ^{14}C values can be changed in the subroutine "c13_closed" and "c14_closed", respectively. Adjustments to the $\delta^{13}C$ vs ^{14}C plot can be made in subroutine "c13c14". Equations for calculating species concentrations under the closed system are provided in subroutine "conc_closed". pH step increments can be modified in subroutine "pCO2". Open/closed system ratio selected for modeled $\delta^{13}C$ and ^{14}C (both for plotting and calculating) can be changed in subroutine "pCO2", and are

shown at the top next to “dcf1”. Iso-pCO_2 lines can also be modified in subroutine “pCO2” near the bottom labeled “Iso-PCO_2 Lines”. Modifications to the iso-pCO_2 lines in the $\delta^{13}C$ vs ^{14}C plot can be made at the bottom of this subroutine. All modeled carbon isotope values along these iso-pCO_2 lines are given in the workspace under “isopH_i”. All equilibrium constants and fractionation factors are shown in subroutine “temperature”. All species concentrations at each pH step are given in the “c” document from the workspace, where the matrix rows going from top to bottom are pH, $CO_{2(aq)}$, HCO_3^-, CO_3^{2-}, and Ca^{2+}.

Appendix B: Supplemental Tables and Figures

Thermo Scientific Triton TIMS Operating Conditions	
Filament Type	Re
Flight Tube Pressure	2.53e-9 mbar
Midivac Pressure	8.00E-7 mbar
High Voltage	10,030 V
Ion Counter	0.358 counts/min
Axial Mass	238
Source Pressure before added liquid nitrogen	1.7E-7 mbar
Source Temperature (°C)	U: 1,700-1,900
	Th: 1,850-2,000

Table S1: Instrument operating parameters for U-series analysis of samples McN-IS-1 and McN-IS-2 on the Thermo Scientific Triton TIMS at the UT Austin.

Mass Scan Cycle		
Sequence	**U**	**Th**
1	233	229
2	233.5	230
3	234	230
4	234	230.55
5	234	232
6	234	-
7	234.45	-
8	235	-
9	235.55	-
10	236	-

Table S2: The analytical sequence of U and Th analysis on the TIMS at the UT Austin. After each sequence a series of lens focusing and peak centering techniques were used to amplify signal intensity. Masses 233.5, 230.55, 234.5 and 235.5 were used to measure background signals.

Session Date	Argon Flow (L/min)	Nitrogen Flow (L/min)	Counting Efficiency ($^{235}U/^{235}U$)	Abundance Sensitivity ($237/^{238}U$)	Dark Noise (cpm)	112A Standard Value + Error (‰)			Uptake rate (mg/s)	Ion Efficiency (%)
						$\delta^{234}U$	$^{235}U/^{233}U$	$^{236}U/^{233}U$		
11/9/2016	5.9	3	100%	3.4E-07	37.2	-38.0 ± 1.11	14.6 ± 0.02	1.026 ± 0.001	0.7	1
11/10/2016	5.9	3	100%	3.5E-07	29.68	-38.1 ± 1.43	14.7 ± 0.02	1.024 ± 0.001	0.7	1

Table S3: Instrument operating parameters for U-series analysis on the Neptune Plus MC-ICP-MS at the University of Minnesota.

Sample ID	Isochron	$[232/238]_A$	1σ error (abs)	$[230/238]_A$	1σ error (abs)	$[234/238]_A$	1σ error (abs)	Age (kyr)	Age error (kyr)	MSWD	230/238 atomic ratio (ppm)	2σ error
McN-8-1	1	6.14E-04	1.93E-05	0.10	1.04E-03	1.11	0.11	10.223	0.072	3.10	14.7	3.4
McN-8-2	1	7.25E-03	1.45E-04	0.12	2.77E-04	1.13	0.08					
McN-8-3	1	2.23E-02	4.46E-04	0.16	4.37E-04	1.12	0.08					
McN-7-1	2	1.32E-02	2.73E-04	0.13	1.19E-03	1.13	0.07	7.852	1.6	51	27	75
McN-7-2	2	8.10E-03	1.62E-04	0.12	2.99E-04	1.13	0.07					
McN-7-3	2	8.39E-03	1.68E-04	0.12	3.09E-04	1.13	0.09					
Values calculated using 2 points												
McN-7-1 and 7-2								11.100	25		10	2.8
McN-7-2 and 7-3								42.000	35		161.9	253
McN-7-1 and 7-3								8.330	14		20.5	3.7

Table S4: Shown are activity ratios ($[232/238]_A$, $[230/238]_A$, and $[234/238]_A$), ISOPLOT calculated ages, MSWDs, and associated errors for isochrons McN-7 and McN-8. Values calculated for 2-point isochrons from McN-7 are shown at the bottom. Ages are reported in kyr, and activity ratio uncertainties are reported as absolute error. McN-7-2 and McN-7-3 (two samples that had similar $^{232}Th/^{238}U$ values) show an age and $^{230}Th/^{232}Th$ value that is not consistent with other calculated values (age = 42 ka, and $^{230}Th/^{232}Th$ = 162 ppm). The $^{230}Th/^{232}Th$ values and ages calculated from the remaining McN-7 two-point isochrons bracket values calculated from the McN-8 isochron. However, these values are not useful in constraining initial $^{230}Th/^{232}Th$ as the isochron-derived uncertainties would not be representative of the $^{230}Th/^{232}Th$ in the McN-1 U-Th system due there only being two points in the calculation.

Full Procedural Blank Values

Sample ID	230Th (pg)	230Th 2σ error	232Th (pg)	232Th 2σ error	234U (pg)	234U 2σ error	235U (pg)	235U 2σ error	238U (pg)	238U 2σ error
FPB -1	1.1E-04	3.1E-05	10.653	0.223	2.2E-04	7.8E-05	1.6E-02	2.0E-03	2.054	0.102
FPB-2	4.3E-04	1.2E-04	7.617	0.07	1.3E-04	1.5E-04	1.1E-02	5.0E-03	1.716	0.083
FPB-3	1.1E-04	5.7E-05	9.525	0.214	2.5E-05	2.2E-05	2.0E-03	1.0E-03	0.341	0.015
FPB-4	4.5E-05	1.6E-05	0.069	0.001	3.5E-05	3.3E-05	4.0E-03	1.0E-03	0.267	0.029

Table S5: Shown are full procedural blank (FPB) Th and U values from FPBs processed in clean labs at UT Austin and UMN. FPBs 1-3 were processed at UT Austin, and FPB 4 was processed at UMN. Values are reported in picograms (pg).

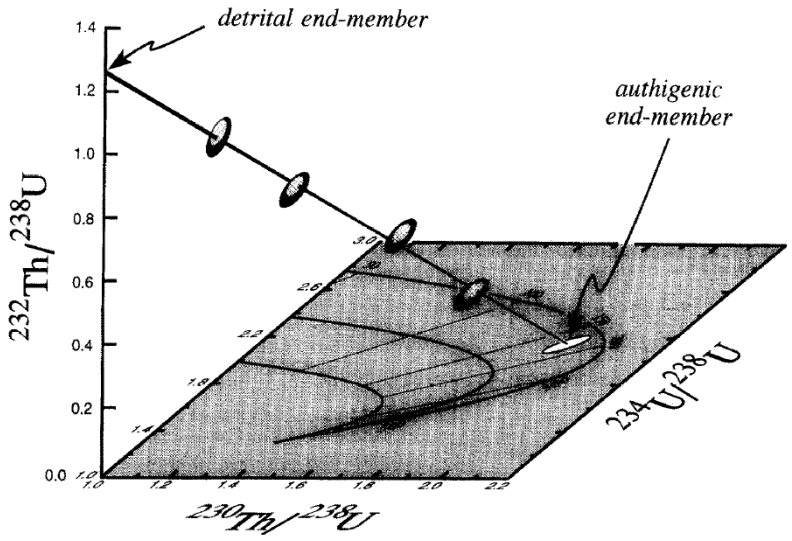

Figure S1: Representation of ^{230}Th-^{234}U-^{238}U data for mixtures of ^{232}Th endmembers, where the open ellipsoid is at the intercept of the regression line with the ^{232}Th-free plane. From Ludwig and Titterington (1994).

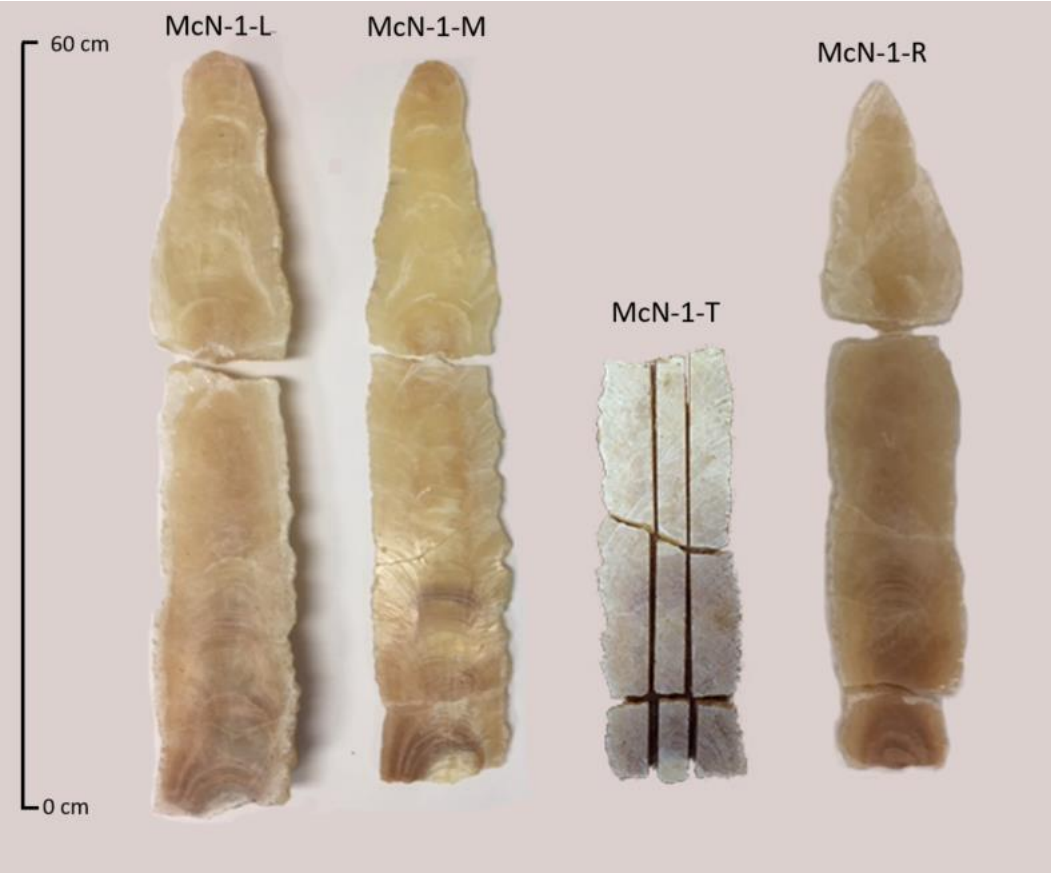

Figure S2: Cut sections of stalagmite McN-1. The two exterior sections (McN-1-L and McN-1-R) and two middle-slabbed sections (McN-1-M and McN-1-T) are shown. The flat side (shown) of the left exterior section (McN-1-L) adjoins the underside of the middle-slabbed section (McN-1-M). U-series, stable isotopes, and ^{14}C samples were collected on the shown side of McN-1-M. Thin sections were made on the growth axis of McN-1-T (see Fig. S5). The shown sides of McN-1-M and McN-1-T were previously adjoined. The underside of McN-1-T previously adjoined the flat side of the right exterior section, McN-1-R.

Figure S3: Photograph of McN-1 cave after it was discovered on August 2, 2014 while excavating a 12-ft wide trench to install a water main beneath McNeil Road in Austin, TX. The cave was approximately 7m long, 1.5m high and 2 m below ground surface. The cave was filled in with concrete after excavation, preventing access to the cave. The cave is located in Kainer member limestone of the Edwards group. McN-1 is shown intact before sample removal.

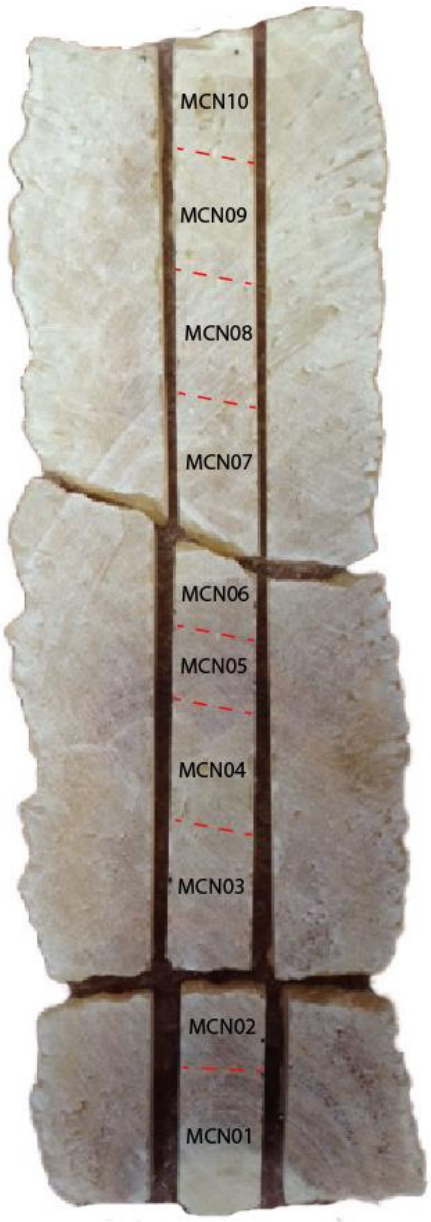

Figure S4: Thin section locations made along the growth axis of middle-slabbed section McN-1-T (see Fig. S2). In total, 10 thin sections were made on the shown side, which previously adjoined the side of McN-1-M where stable isotope, U-series and ^{14}C samples were collected.

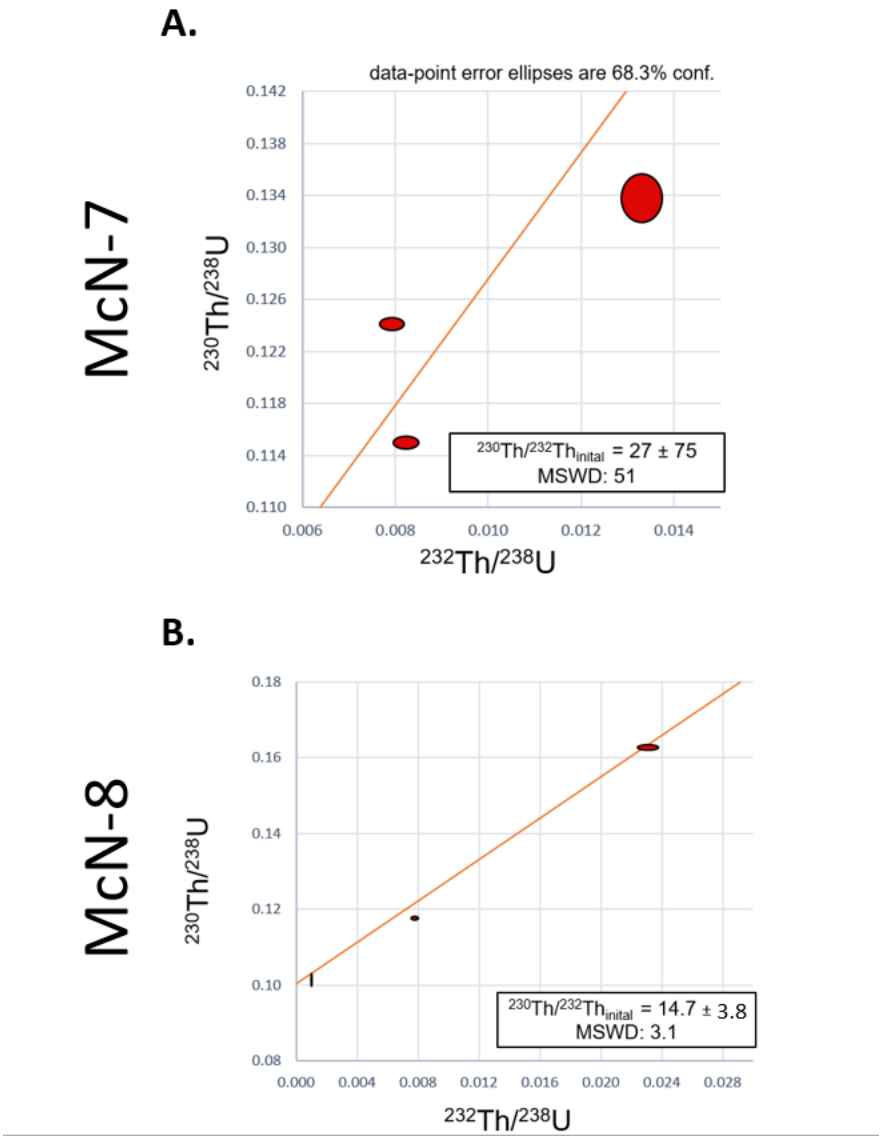

Figure S5: Shown are $^{230}Th/^{238}U$ vs. $^{232}Th/^{238}U$ Osmond Type-II isochron diagrams computed using ISOPLOT 4.15. The regression line is shown in orange, and the red ellipses are error ellipsoids showing the 1σ confidence interval. The calculated $^{230}Th/^{232}Th_{initial}$ and MSWD values are given for each isochron.

REFERENCES

Alley, R. 2000. The Younger Dryas cold interval as viewed from central Greenland Quat. Sci. Rev., 19, 2000, pp. 213–226

Alley, R.B. and P.U. Clark, The deglaciation of the northern hemisphere: a global perspective, Ann. Rev. Earth Planet. Sci., 27, 149-182, 1999.

Atkinson, T.C. (1977) Carbon dioxide in the atmopshere of the unsaturated zone: an important control of groundwater hardness in limestones. J. Hydrol. 35, 111-123.

Ayalon, A., Bar-Matthews, M., and Kaufman, A., 1999, Petrography, strontium, barium and uranium concentrations, and strontium and uranium isotope ratios in speleothems as palaeoclimatic proxies: Soreq Cave, Israel: The Holocene, v. 9, p. 715–722, doi:10.1191/095968399673664163.

Baker, A, Smart PL, Edwards RL, Richards DA, 1993. Annual growth banding in a cave stalagmite. Nature 364: 518-520

Baker, A., Barnes, W.L., and Smart, P.L., 1997, Variations in the discharge and organic matter content of stalagmite drip waters in Lower Cave: Hydrological Processes, v. 11, p. 1541–1555.

Banner, J.L., Gilfoyle, A., James, E.W., Stern, L.A., and Musgrove, M., 2007, Seasonal variations in modern speleothem calcite growth in Central Texas, U.S.A.: Journal of Sedimentary Research, v. 77, p. 615–622. doi:10.2110/jsr.2007.065.

Banner, J. L., Jackson, C. S., Zong-Liang, Y., Hayhoe, K., Woodhouse, C., Gulden, L., Jacobs, K., North, G., Leung, R., Washington, W., Jiang, X., Casteel, R., 2010, Climate change impacts on Texas water: A white paper assessment of the past, present and future and recommendations for action. Texas Water Journal 1, 1.

Bar-Matthews, M., Ayalon, A., Kaufman, A., 1997. Late quaternary paleoclimate in the eastern Mediterranean region from stable isotope analysis of speleothems at Soreq cave. Isr. Quat. Res. 47, 155e168. http://dx.doi.org/10.1006/ qres.1997.1883.

Bar-Matthews, M., Ayalon, A., Kaufman, A., Wasserburg, G.J., 1999. The eastern Mediterranean palaeoclimate as a reflection of regional events: Soreq Cave, Israel. Earth Planet. Sci. Lett. 166, 85e95.

Bergel, S.J., Carlson, P.E., Larson, T.E., Wood, C.T., Johnson, K.R., Banner, J.L., Breecker, D.O., Constraining the subsoil carbon source to cave-air CO2and speleothem calcite in central Texas, Geochimica et Cosmochimica Acta (2017), doi: http://dx.doi.org/10.1016/j.gca.2017.08.017

Berkelhammer, M., Stott, L., Yoshimura, K., Johnson, K., Sinha, A., 2011. Synoptic and mesoscale controls on the isotopic composition of precipitation in the western United States. Clim. Dyn. 38, 433e454. http://dx.doi.org/10.1007/s00382-011-1262-3.

Boch, R. Spotl, C., Frisia, S., 2011. Origin and paleoenvironmental significance of lamination in stalagmites from Katerloch Cave, Austria. Sedimentology 58, 508-531

Boutton, T.W., 1998. δ13C values of soil organic carbon and their use in documenting vegetation changes in a subtropical savanna ecosystem. In: Geoderma, pp. 5–41.

Breecker, D.O., Payne, A.E., Quade, J., Banner, J.L., Ball, C.E., Meyer, K.W., and Cowan, B.D., 2012, The sources and sinks of CO2 in caves under mixed woodland and grassland vegetation: Geochimica et Cosmochimica Acta, v. 96, p. 230–246, doi: 10.1016/j.gca.2012.08.023.

Breitenbach, S. F. M., K. Rehfeld, B. Goswami, J. U. L. Baldini, H. E. Ridley, D. Kennett, K. Prufer, V. V. Aquino, Y. Asmerom, V. J. Polyak, H. Cheng, J. Kurths, and N. Marwan. "COnstructing Proxy-Record Age Models (COPRA)." Climate of the Past Discussions 8.3 (2012): 2369-408.

Clark, P.U., Shakun, J.D., et al., 2012. Global climate evolution during the last deglaciation. Procedings of the National Academy of Sciences of the United States of America, 109, E1134-E1142.

Cole, KL, and Arundel, ST, 2005, Carbon isotopes from fossil packrat pellets and elevational movements of Utah agave plants reveal the Younger Dryas cold period in Grand Canyon, Arizona. Geology 33: 713–716

Cooke, M.J., Stern, L.A., Banner, J.L., Mack, L.E., Stafford, T.W., Toomey, R.S., 2003. Precise timing and rate of massive late Quaternary soil denudation. Geology 31, 853e856. http://dx.doi.org/10.1130/G19749.1.

Cooke, M.J., 2005, Soil formation and erosion in central Texas: insights from relict soils and cave deposits, PhD.dissertation. The University of Texas, Austin.

Cooke, M.J., Libby A.S, Banner, J.L., and Edwards, E.., 2007. Evidence for the Silicate Source of Relict Soils on the Edwards Plateau, Central Texas. Quaternary Research 67.02. 275-85.

Coplen, T. B., P. De Bièvre, H. R. Krouse, R. D. Vocke Jr., M. Gröning, and K. Rozanski (1996), Ratios for light-element isotopes standardized for better interlaboratory comparison, Eos Trans. AGU, 77(27), 255–255, doi:10.1029/96EO00182.

Cowan, B., Osborne, M. and Banner, J. L., 2013, Temporal variability of cave-air CO2 in central Texas. Journal of Cave and Karst Studies 75, p. 38–50. doi:10.4311/2011ES0246 (Article).

Cruz, F. W. , Vuille, M. , Burns, S. J. , Wang, X. , Cheng, H. , Werner, M. , Edwards, R. L. , Karmann, I. , Auler, A. S. and Nguyen, H., 2009, Orbitally driven eastwest antiphasing of South American precipitation , Nature Geoscience, 2 , 210-214, . doi: 10.1038/ngeo444Cuffey, K.M., G.D. Clow, R.B. Alley, M. Stuiver, E.D. Waddington, and R.W. Saltus, Large Arctic temperature change at the Wisconsin-Holocene glacial transition, Science, 270, 455-458, 1995.

Breecker, D., Payne, A.E., Quade, J., Banner, J.L., Carolyn B., Meyer, k., Cowan, B., The sources and sinks of CO in caves under mixed woodland and grassland vegetation, 2017, Geochimica et Cosmochimica Acta, Volume 96, 2012, Pages 230-246, ISSN 0016-7037, http://dx.doi.org/10.1016/j.gca.2012.08.023

Bowling D. R., Pataki D. E. and Randerson J. T., 2008, Carbon isotopes in terrestrial ecosystem pools and CO2 fluxes. New Phytol. 178, 24–40.

Dansgaard, S.J. Johnsen, H.B. Clausen, D. Dahl-Jensen, N.S. Gundestrup, C.U. Hammer, C.S. Hvidberg, J.P. Steffensen, A.E. Sveinbjornsdottir, J. Jouzel, G., 1993. Bond Evidence for general instability of past climate from a 250-kyr ice-core record Nature, 364 (1993), pp. 218–220.

Dansgaard, W., J.W. White, and S.J. Johnsen, The abrupt termination of the Younger Dryas climate event, Nature, 339, 532-534, 1989.

Davidson EA, Janssens IA, 2006 Temperature sensitivity of soil carbon decomposition and feedbacks to climate change. Nature 440:165-173

Deininger M., Fohlmeister J., Scholz D. and Mangini A., 2012, Isotope disequilibrium effects: The influence of evaporation and ventilation effects on the carbon and oxygen isotope composition of speleothems – a model approach. Geochim. Cosmochim. Acta 96, 57–79.

Deplazes, G. et al. Links between tropical rainfall and North Atlantic climate during the last glacial period. Nature Geosci. 6, 213–217 (2013).

Dickson, J.A.D., 1993, Crystal growth diagrams as an aid to interpreting the fabrics of calcite aggregates: Journal of Sedimentary Petrology, v. 63, p. 1–18.

Diefendorf, A.F., Mueller, K.E., Wing, S.L., Koch, P.L., Freeman, K.H., 2010. Global pat-terns in leaf 13C discrimination and implications for studies of past and future climate. Proc. Natl. Acad. Sci. USA107, 5738–5743.

Dreybrodt, W., Processes in karst systems--Physics, chemistry and geology, in Springer Series in Physical Environments 5, SpringerVerlag, New York, 1988

Dorale, J. a, Gonzalez, L. a, Reagan, M.K., Pickett, D. a, Murrell, M.T., Baker, R.G., 1992. A high-resolution record of holocene climate change in speleothem calcite from cold water cave, northeast iowa. Science 258, 1626e1630. http://dx.doi.org/ 10.1126/science.258.5088.1626.

Dulinski, M., and Rozanski, K., 1990. “Formation of 13C/13C Ratios in Speleothems: A Semi-Dynamic Model.” Radiocarbon 32:7-16.

Ellwood, B.B., Gose, W.A., 2006. Heinrich H1 and 8200 yr B.P. climate events recorded in Hall's Cave, Texas. Geology 34, 753e756. http://dx.doi.org/10.1130/ G22549.1.

Eberts, S.M., Kauffman, L.J., Bexfield, L.M., and Lindgren, R.J., 2011, Overview of chapter B: Additional regional investigations of the transport of anthropogenic and natural contaminants to public-supply wells, section 1 of Eberts, S.M., ed.,

Hydrogeologic settings and groundwater-flow simulations for regional investigations of the transport of anthropogenic and natural contaminants to public-supply wells—Investigations begun in 2004: Reston, Va., U.S. Geological Survey Professional Paper 1737–B, pp. 1-1–1-6.

Fairchild I.J., Baker A., Borsato A., , Frisia S., Hinton R.W., Mcdermott F., Tooth A.F., 2001 - Annual to sub-annual resolution of multiple trace-element trends in speleothems. Journal of the Geological Society London, 158: 831841.

Fairchild, I.J., Smith, C.L., Baker, A., Fuller, L., Spotl, C., Mattey, D., McDermott, F., EIMF, 2006. Modification and preservation of environmental signals in speleothems. Earth-Sci Rev. 75, 105e153.

Fairchild, I.J., Treble. P.C., 2009. Trace elements in speleothems as recorders of environmental change. Quat. Sci. Rev., 28 (2009), pp. 449-468

Feng, W., Banner, J. L., Guilfoyle, A., Musgrove, M., and James, E. W., 2012, Oxygen isotopic fractionation between drip water and speleothem calcite: A 10-year monitoring study, central Texas, USA. Chemical Geology304-305, 53-67. (Article)

Feng, W., Hardt, B.F., Banner, J.L., Meyer, K.J., James, E.W., Musgrove, M., Edwards, R.L., Cheng, H., and Min, A., 2014b, Changing amounts and sources of moisture in the U.S. southwest since the Last Glacial Maximum in response to global climate change: Earth and Planetary Science Letters, v. 401, p. 47–56, doi: 10.1016/j.epsl.2014.05.046. (Article)

Feng, W., Casteel, R.C., Banner, J.L., Heinze-Fry, A., 2014a. Oxygen isotope variations in rainfall, drip-water and speleothem calcite from a well-ventilated cave in Texas, USA: assessing a new speleothem temperature proxy. Geochim. Cosmochim. Acta 127, 233e250. http://dx.doi.org/10.1016/j.gca.2013.11.039.

Fleitmann, D., Burns, SJ., Mangini, A., Mudelsee, M., Kramers, J., Nilla, I., et al., 2006, Holocene ITCZ and Indian monsoon dynamics recorded in stalagmites from Oman and Yemen (Socotra). Quaternary Science Reviews. 26:170-88

Fisher, W. L., and Rodda, P. U., 1969, Edwards Formation (Lower Cretaceous), Texas: dolomitization in a carbonate platform system: The University of Texas at Austin, Bureau of Economic Geology Geological Circular 69-1. Reprinted from

American Association of Petroleum Geologists Bulletin, v. 53, no. 1, p. 55-74, 14 figs.

Fohlmeister J., Kromer B. , A. Mangini, 2011. The influence of soil organic matter age spectrum on the reconstruction of atmospheric 14C levels via stalagmites Radiocarbon, 53 (1) (2011), pp. 99–115

Fohlmeister, J., D. Scholz, B. Kromer, and A. Mangini. "Modelling Carbon Isotopes of Carbonates in Cave Drip Water." Geochimica Et Cosmochimica Acta 75.18 (2011): 5219-228.

Frappier, A., Sahagian, D., Gonzalez, L.A., and Carpenter, S.J., 2002, El Niño events recorded by stalagmite carbon isotopes: Science, v. 298, p. 565, doi: 10.1126/science.1076446.

Friedman, I., O'Neil, J., Cebula, G. (1982): Two New Carbonate Stable Isotope Standards. Geostandards Newsletter, 6 (1), 11-12.

Frisia, S., Borsato, A., Fairchild, I.J., and McDermott, F., 2000, Calcite fabrics, growth mechanisms, and environments of formation in speleothems from the Italian Alps and southwestern Ireland: Journal of of Sedimentary Research, v. 70, no. 5, p. 1183–1196. doi:10.1306/ 022900701183.

Gary, M. O., B. B. Hunt, and R. H. Gary, 2011, Interconnection of the Trinity (Glen Rose) and Edwards Aquifers along the Balcones fault zone and related topics, Proceedings of the Karst Conservation Initiative; Austin, Texas.

Genty, D., Baker, A., Massault, M., Proctor, C., Gilmour, M., Pons-Branchu, E., Hamelin, B., 2001b. Dead carbon in stalagmites: carbonate bedrock paleodissolution vs. ageing of soil organic matter. Implications for 13C variations in speleothems. Geochim. Cosmochim. Acta 65, 3443e3457. http://dx.doi.org/ 10.1016/S0016-7037(01)00697-4.

Genty, D., Blamart, D., Ghaleb, B., Plagnes, V., Causse, C., Bakalowicz, M., Zouari, K., Chkir, N., Hellstrom, J., Wainer, K., 2006. Timing and dynamics of the last deglaciation from European and North African d13C stalagmite profi- lesdcomparison with Chinese and South Hemisphere stalagmites. Quat. Sci. Rev. 25, 2118e2142. http://dx.doi.org/10.1016/j.quascirev.2006.01.030.

Gill, I., J. J. Olson, and D. K. Hubbard, 1995, Corals, paleotemperature records, and the aragonite-calcite transformation, Geology, 23(4), 333 – 336.

Gonzalez-Lemos, S., Jimenez-Sanchez, M., Stoll, H. 2014. Sediment transport during recent cave flooding events and characterization of speleothem archives of past flooding, Geomorphology, doi: 10.1016/j.geomorph.2014.08.029

Griffi ths, M.L., Drysdale, R.N., Gagan, M.K., Frisia, S., Zhao, J., Ayliffe, L.K., Hantoro, W.S., Hellstrom, J.C., Fischer, M.J., Feng, Y., and Suwargadi, B.W., 2010, Evidence for Holocene changes in Australian-Indonesian monsoon rainfall from stalagmite trace element and stable isotope ratios: Earth and Planetary Science Letters, v. 292, p. 27–38, doi:10.1016/j .epsl.2010.01.002.

Griffiths M., Fohlmeister J., Drysdale R., Hua Q., Johnson K.R., Hellstrom J., M. Gagan, J.-X. Zhao, 2012. Hydrological control of the dead carbon fraction in a Holocene tropical speleothem, Quat. Geochronol., 14, pp. 81–93

Griffiths, M.L., Drysdale, R.N., Gagan, M.K., Hellstrom, J.C., Couchoud, I., Ayliffe, L.K., Vonhof, H.B., Hantoro, W.S., 2013. Australasian monsoon response to DansgaardeOeschger event 21 and teleconnections to higher latitudes. Earth Planet. Sci. Lett. 369e370, 294e304. http://dx.doi.org/10.1016/j.epsl.2013.03.030.

Grootes, P.M., and M. Stuiver. 1997. Oxygen 18/16 variability in Greenland snow and ice with 10^3 to 10^5-year time resolution. Journal of Geophysical Research 102:26455-26470.

Haug, G. H., Hughen, K. A., Sigman, D. M., Peterson, L. C. & Ro¨hl, U. Southward migration of the Intertropical Convergence Zone through the Holocene. Science 293, 1304–1308 (2001).

Hendy, C., 1971. The isotopic geochemistry of speleothemsdI. The calculation of the effects of different modes of formation on the isotopic composition of speleothems and their applicability as palaeoclimatic indicators. Geochim. Cosmochim. Acta 35, 801e824. http://dx.doi.org/10.1016/0016-7037(71)90127-X.

Higgins, R.W., 1997. Influence of the North American Monsoon System on the U.S. summer precipitation regime. J. Clim. 10, 2600e2622.

Holliday, V.T., 2001. Stratigraphy and geochronology of upper Quaternary eolian sand on the Southern High Plains of Texas and New Mexico, United States. Geol. Soc. Am. Bull. 113, 88e108

Holliday, V.T., Meltzer, D.J., Mandel, R., 2011. Stratigraphy of the Younger Dryas Chronozone and paleoenvironmental implications: Central and Southern Great Plains. Quaternary International 242, 520–533.

Hughen, K. A., J. T. Overpeck, L. C. Peterson, and S. Trumbore, Rapid climate changes in the tropical Atlantic region during the last deglaciation, Nature, 380, 51 – 54, 1996.

J.A. Dorale and Z. Liu, 2009, Limitations of hendy test criteria in judging the paleoclimatic suitability of speleothems and the need for replication. Journal of Cave and Karst Studies, v. 71, no. 1, p. 73–80.

Kendall, A.C., & Broughton, P.L., 1978, Origin of fabrics in speleothems composed of columnar calcite crystals: Journal of Sedimentary Petrology, v. 48, n. 2, p. 519-538.

Kohn, M.J., 2010. Carbon isotope compositions of terrestrial C3plants as indi-cators of (paleo)ecology and (paleo)climate. Proc. Natl. Acad. Sci. USA107, 19691–19695.

Kuzyakov, Y., and Larionova, A.A., 2005, Root and rhizomicrobial respitration: A review of approaches to estimate respiration by autotrophic and heterotrophic organisms in soil. J. Plant Nutr. Soil Sci. 168, 503-520.

Kutzbach, J.E., and Guetter, P.J., 1986, The influence of changing orbital parameters and surface boundary conditions on climate simulations for the past 18,000 years: Journal of the Atmospheric Sciences, v. 43, p. 1726–1759.

Ludwig K. R. and Titteringon D. M. 1994: Calculation of 230Th/U isochrons, ages, and errors. Geochimica et Cosmochimica Acta 58: 5031 – 5042.

Masson-Delmotte, V., M. Schulz, A. Abe-Ouchi, J. Beer, A. Ganopolski, J.F. González Rouco, E. Jansen, K. Lambeck, J. Luterbacher, T. Naish, T. Osborn, B. Otto-Bliesner, T. Quinn, R. Ramesh, M. Rojas, X. Shao and A. Timmermann, 2013: Information from Paleoclimate Archives. In: Climate Change 2013: The Physical Science Basis. Contribution of Working Group I to the Fifth Assessment Report

of the Intergovernmental Panel on Climate Change [Stocker, T.F., D. Qin, G.-K. Plattner, M. Tignor, S.K. Allen, J. Boschung, A. Nauels, Y. Xia, V. Bex and P.M. Midgley (eds.)]. Cambridge University Press, Cambridge, United Kingdom and New York, NY, USA.

Mattey, D., Atkinson, T., Barker, J., Fisher, R., Latin, J.-P., Durrell, R. and Ainsworth, M. (2016) Carbon dioxide, ground air and carbon cycling in Gibraltar karst. Geochim. Cosmochim. Acta 184, 88-113.

McDermott, F., 2004. Palaeo-climate reconstruction from stable isotope variations in speleothems: a review. Quat. Sci. Rev. 23, 901e918. http://dx.doi.org/10.1016/ j.quascirev.2003.06.021.

McDonough, L., Iverach, C., Beckmann, S., Manefield, M., Rau, G., Baker, A. and Kelly, B. (2016) Spatial variability of cave-air carbon dioxide and methane concentrations and isotopic compositions in a semi-arid karst environment. Environ. Earth Sci. 75, 1-20.

Menking, K.M., R.Y. Anderson, N.G. Shafike, K.H. Syed, and B.D. Allen (2004), Wetter or colder during the Last Glacial Maximum? Revisiting the pluvial lake question in southwestern North America, Quaternary Research, 62, 280-288.

Mook, W.G., and J.J. De Vries. 2000. Environmental isotopes in the hydrological cycle: Principles and applications/ Vol. 1 Introductions-Theory, methods, review. Vienna: IAEA, Isotope Hydrology Section.

Mook, W. (2002) Introduction to isotope hydrology: stable and radioactive isotopes of hydrogen, oxygen and carbon, International Association of Hydrogeologists. Taylor and Francis.

NOAA, 2017, National Oceanic and Atmospheric Administration. Climate Data Center (CDC), n.d.

Nordt, L. C., Boutton, T. W., Hallmark, C. T., and Waters, M. R., 1994, Late Quaternary vegetation and climate change in Central Texas based on the isotopic composition of organic carbon. Quaternary Research 41, 109–120.

Noronha, A. L., Johnson, K. R., Southon, J. R., Hu, C., Ruan, J., and McCabe-Glynn, S., 2015,: Radiocarbon evidence for decomposition of aged organic matter in the

vadose zone as the main source of speleothem carbon, Quaternary Sci. Rev., 127, 37–47, doi:10.1016/j.quascirev.2015.05.021, 2015.

Noronha, A.L., Johnson, K.R., Hu, C., Ruan, J., Southon, J.R., Ferguson, J.E., 2014. Assessing influences on speleothem dead carbon variability over the Holocene: implications for speleothem-based radiocarbon calibration. Earth Planet. Sci. Lett. 394, 20e29. http://dx.doi.org/10.1016/j.epsl.2014.03.015.

Oster, J., Montan¸ez, I., Guilderson, T., Sharp, W.D., Banner, J.L., 2010. Modeling speleothem d13C variability in a Central Sierra Nevada cave using 14C and 87Sr/ 86Sr. Geochim. Cosmochim. Acta 74, 5228e5242.

Partin, J. W., Cobb, K. M., Adkins, J. F., Clark, B. & Fernandez, D. P. Millennial-scale trends in west Pacific warm pool hydrology since the Last Glacial Maximum. Nature 449, 452–455 (2007).

Peterson, L. C., and G. H. Haug (2006), Variability in the mean latitude of the Atlantic Intertropical Convergence Zone as recorded by riverine input of sediments to the Cariaco Basin (Venezuela), Palaeogeogr. Palaeoclimatol. Palaeoecol., 234, 97–113, doi:10.1016/j.palaeo.2005.10.021.

Polyak, V.J., Rasmussen, J., Asmerom, ., 2004. Prolonged wet period in the southwestern United States through the Younger Dryas: Geology, v. 32, p. 5-8.

Polyak, V.J., Rasmussen, J.B.T., and Asmerom, Y., 2004, Prolonged wet period in the southwestern United States through the Younger Dryas: Geology, v. 32, p. 5–8, doi:10.1130/G19957.1.

Polyak, V.J., and Asmerom, Y., 2001, Late Holocene climate and cultural changes in the southwestern United States: Science, v. 294, p. 148–151.

Rasmussen, S. O., et. al., 2006. A new Greenland ice core chronology for the last glacial termination, J. Geophys. Res., 111, D06102, doi:10.1029/2005JD006079.

Reimer P.J., Bard E., A. Bayliss, J.W. Beck, P.G. Blackwell, C.B. Ramsey, C.E. Buck, H. Cheng, R.L. Edwards, M. Friedrich, P.M. Grootes, T.P. Guilderson, H. Haflidason, I. Hajdas, C. Hatte, T.J. Heaton, D.L. Hoffmann, A.G. Hogg, K.A. Hughen, K.F. Kaiser, B. Kromer, S.W. Manning, M. Niu, R.W. Reimer, D.A. Richards, E.M. Scott, J.R. Southon, R. Staff, C.S.M. Turney, J. van der Plicht.

IntCal13 and Marine13 radiocarbon age calibration curves 0–50,000 years cal BP. Radiocarbon, 55 (4) (2013), pp. 1869–1887

Richards, D.A., and Dorale, J.A., 2003, Uranium-series chronology and environmental applications of speleothems: Reviews in Mineralogy and Geochemistry, v. 52, p. 407–460.

Ridley, H.E., Asmerom, Y., Baldini, J.U.L., Breitenbach, S.F.M., Aquino, V.V., Prufer, K.M., Culleton, B.J., Polyak, V., Lechleitner, F. a., Kennett, D.J., Zhang, M., Marwan, N., Macpherson, C.G., Baldini, L.M., Xiao, T., Peterkin, J.L., Awe, J., Haug, G.H., 2015. Aerosol forcing of the position of the intertropical convergence zone since ad 1550. Nat. Geosci. 8

Saribudak, M., 2016. Geophysical mapping of Mount Bonnell fault of Balcones fault zone and its implications on Trinity-Edwards Aquifer interconnection, central Texas, USA. The Leading Edge, 35(9), 752–758. https://doi-org.ezproxy.lib.utexas.edu/10.1190/tle35090752.1

Schmidt, G.A., J.H. Jungclaus, C.M. Ammann, E. Bard, P. Braconnot, T.J. Crowley, G. Delaygue, F. Joos, N.A. Krivova, R. Muscheler, B.L. Otto-Bliesner, J. Pongratz, D.T. Shindell, S.K. Solanki, F. Steinhilber, and L.E.A. Vieira, 2012: Climate forcing reconstructions for use in PMIP simulations of the Last Millennium (v1.1). Geosci. Model Dev., 5, 185-191, doi:10.5194/gmd-5-185-2012.

Seager, R., M. Ting, C. Li, N. Naik, B. Cook, J. Nakamura, and H. Liu, 2013: Projections of declining surface-water availability for the southwestern United States. Nature Clim. Change, 3, 582-486, doi:10.1038/nclimate1787.

Seager, R., Ting, M., Held, I., Kushnir, Y., Lu, J., Vecchi, G., Huang, H.-P., Harnik, N., Leetmaa, A., Lau, N.-C., Li, C., Velez, J., Naik, N., 2007. Model projections of an imminent transition to a more arid climate in southwestern North America. Science 316, 1181e1184. http://dx.doi.org/10.1126/science.1139601.

Severinghaus, J.P., Sowers, T., Brook, E.J., Alley, R.B., Bender, M.L., 1998. Timing of abrupt climate change at the end of the Younger Dryas interval from thermally fractionated gases in polar ice. Nature 391, 141–146.

Sharp, J. M., Jr. and Banner, J. L., 2000, The Edwards Aquifer: Water for Thirsty Texans, in: Schneiderman, J., ed., The Earth Around Us: Maintaining a Livable Planet, W. H. Freeman and Co., New York, pp 154-165.

Stahle, D.W., Cleaveland, M.K. 1988. Texas drought history reconstructed and analyzed from 1698 to 1980 J. Climate, 1 , pp. 59-74

Stocker, T.F., Wright, D.G., Broecker, W.S., 1992. The influence of high-latitude surface forcing on the global thermohaline circulation, Paleoceanography, 7, pp. 529–541

Stuiver M, Polach HA. 1977. Discussion: reporting of 14C data. Radiocarbon 19(3): 355-63

Stuiver, M., P.M. Grootes, and T.F. Braziunas. 1995. The GISP2 18O climate record of the past 16,500 years and the role of the sun, ocean and volcanoes. Quaternary Research 44:341-354

Svensson, K. K. Andersen, M. Bigler, H. B. Clausen, D. Dahl-Jensen. 2008, A 60,000 year Greenland stratigraphic ice core chronology. Climate of the Past, European Geosciences Union (EGU), 2008, 4 (1), pp.47-57.

Talbot, M. R., Filippi, M. L., Jensen, N. B. & Tiercelin, J.-J.. An abrupt change in the African monsoon at the end of the Younger Dryas. Geochem. Geophys. Geosyst 8, 16PP (2007).

Taylor, K.C, W. Lamorey, G.A. Doyle, R.B. Alley, P.M. Grootes, P.A. Mayewski, J.W.C. White, and L.K. Barlow. 1993, The 'flickering switch' of late Pleistocene climate change, Nature, 361, 432-436, 1993.

Texas Water Development Board (TWBD), 2017. 2016 Regional and 2017 State Water Plan Projections Data. Austin: TWDB, 2017. Print.

Titterington, D.M., Hallidat,A.N., 1979. On fitting of parallel isochrons and the method of maximum likelihood. Chemical Geology 26, 183-195.

Toomey III, R.S., Blum, M.D., Valastro Jr., S., 1993. Late Quaternary climates and environments of the Edwards Plateau, Texas. Global and Planetary Change 7, 299–320.

Trumbore SE, Chadwick OA, Amundson R. 1996. Rapid exchange between soil carbon and atmospheric carbon dioxide driven by temperature change. Science 272(5260):393–6.

Texas Water Development Board (TWDB), 2005. The Texas Manual on Rainwater Harvesting. Third Edition. p. 30.

Wortham B., James E.W. and Banner J.L. (2013) Variability in initial 230Th/232Th ratios in central Texas speleothems is used for more accurate age determination. Geol. Soc. Am. SouthCentral Section – 47th Annual Meeting, Abstract, 17.

Wood, B.D., Keller, C.K. and Johnstone, D.L. (1993) In situ measurement of microbial activity and controls on microbial CO2 production in the unsaturated zone. Water Resour. Res. 29, 647-659.

Wood, W.W. and Petraitis, M.J. (1984) Origin and distribution of carbon dioxide in the unsaturated zone of the southern high plains of Texas. Water Resour. Res. 20, 1193-1208.

Zhou, J., Lundstrom, C.C., Fouke, B., Panno, S., Hackley, K., and Curry, B., 2005, Geochemistry of speleothem records from southern Illinois: Development of (234U)/(238U) as a proxy for paleoprecipitation: Chemical Geology, v. 221, p. 1–20, doi:10.1016/j.chemgeo.2005.02.005.